Van der Waals heterostructures with photo-oxidised high-κ dielectrics

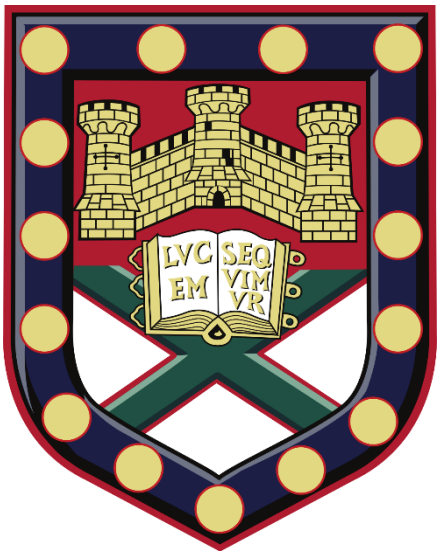

Submitted by Janire Escolar Ulibarri to the University of Exeter as a thesis

for the degree of Doctor of Philosophy in Physics

December 2019

This thesis is available for Library use on the understanding that it is copyright material and that no quotation from the thesis may be published without proper acknowledgement.

I certify that all material in this thesis which is not my own work has been identified and that no material has previously been submitted and approved for the award of a degree by this or any other University.

Janire Escolar Ulibarri

Abstract

The emergence of atomically thin systems has underpinned significant discoveries in fundamental science and game changing innovation in novel technologies such as energy storage and data communication. In this thesis, different types of optoelectronic devices based on van der Waals (vdW) heterostructures are investigated. A high-dielectric (κ) material hafnium disulphide (HfS_2) is embedded into these heterostructures and photo-oxidised into hafnium oxide (HfO_x) by laser writing selectively and underneath the contacts. Moreover, HfO_x as a gate dielectric for field-effect transistors (FET) instead of hexagonal boron nitride (h-BN) is also shown. A dielectric constant for hafnium oxide of ~15 is reported, which shows a novel way to introduce dielectrics in such complicated structures being compatible with two-dimensional 2D materials. Finally, the impact of the dielectric environment on monolayer tungsten diselenide (1L-WSe_2) while been surrounded by different dielectric materials such as quartz, hexagonal boron nitride, indium selenide (In_2Se_3) and hafnium oxide, is demonstrated. The effect of the dielectric environment on the exciton binding energies and quasiparticle bandgap has been investigated by measuring the energy separation between the 1s and 2s states using transmission measurements. The exciton binding energy, as well as the electronic band gap, were found to decrease as the average dielectric constant increases. The largest reduction of band gap by ~300 meV is observed when WSe_2 is encapsulated between HfO_x compared with that of exposed WSe_2 on quartz.

Acknowledgments

I acknowledge the financial support from the Engineering and Physical Sciences Research Council (EPSCR) of the United Kingdom (Grant No. 1651726).

This work would have not been done without these people.

I would like to thank to my supervisors; Saverio and Monica for having me these two years and giving me feedbacks under their supervision.

I especially need to thank to my research group: the workmates that already left Peng, Matt, Gareth, Elias, Gabriela, Iddo. Especially Nikola for her feedbacks and support since I became part of the group and made me feel like a second family and Jake for encouraging me to try yoga and training me in G16 as well. Namphung for training, teaching me so much and becoming my friend. The workmates that still remain Adolfo for training me and his useful feedbacks as well as his support. Lauren, Agnes, Jonas, Kieran, Ioannis and Konstantinos for their support.

I would like to thank to my old workmate, Gregor, for being there in the first two years in the University.

I need to thank Mark Heath for inducting and training me in the cleanroom and for being patient when I first came with a poor level of English and for his jokes and support. Also, thanks to Chris Forrest for fixing the computer and for his support.

Aside from Physics colleagues, I would like to thank to my first group of friends in Exeter: Sarah, Ana, Manu, Ploy and my first housemate Polly that took me to her house and made a home of it and my second group of friends: Santiago, Henry, Constanza, Alba, Sergio, David, and Carlota for their support and funny adventures and parties.

I would like to thank to my Yoga instructors as Yoga has changed my life completely, and to Katie my weight-lifting trainer as I did not see myself having such strength before meeting her.

I would like to thank to Noris for her support and making the building a better place and to Yessenia and Tamara.

From Spain, I thank to my master friends; Nerea and Sandra, some of my high school and Physics bachelor friends and to Javier for supporting me during Physics. I would like to thank to my best friend Virginia as she has been there for me.

I would like to thank to Jon for all his love and support during this last year as you caught me falling and to my cute hamster Floppy that brings me joy every day.

From my heart, I especially thank to my family to their support, love and care during my life and for raising me as they know what I have been through. They are my rock.

Contents

Publications

- *Engineering dielectric screening for potential well arrays of excitons in 2D material*. N. Peimyoo, H.-Y. Wu, J. Escolar, A. De Sanctis, G. Prando, F. Vollmer, F. Withers, K. S. Thygesen, A.C. Riis-Jensen, M. F. Craciun and S. Russo. *In preparation*.
- *Electrical tuning of optically active interlayer excitons in bilayer MoS_2. In preparation*.
- *Graphene Quantum Transcapacitors for non-linear electronics.*A.De Sanctis*,* J. D. Mehew, N. Peimyoo,J.Escolar,Takashi Taniguchi,Kenji Watanabe, M. F. Craciun and S. Russo. *In preparation*.
- *Laser-writable high-κ dielectric for van der Waals nanoelectronics.* N. Peimyoo, M. D. Barnes, J. D. Mehew, A. De Sanctis, I. Amit, J. Escolar, K. Anastasiou, A. P. Rooney, S. J. Haigh, S. Russo, M. F. Craciun and F. Withers. Science Advances **5**, 1 (2019).
- *Anisotropic magnetoconductance and Coulomb blockade in defect engineered $Cr_2Ge_2Te_6$ van der Waals heterostructures*. J. Escolar, N. Peimyoo, M. F. Craciun, H. A. Fernandez, S. Russo, M. D. Barnes, and F. Withers. Physical Review letters B **100**, 054420 (2019).

Author declaration

The work of this thesis has been carried out as a part of a team researchers. In this section, I will explain my contribution in each of the experimental chapters.

Chapter 5

In this chapter, I fabricated some of the memory devices samples.

Chapter 6

In this chapter, I fabricated some of the samples and I was involved in the measurements, data analysis and in the manuscript writing.

List of figures

List of acronyms

A Acoustic branch

ALD atomic layer-deposition

Al_2O_3 alumina

Au gold

B Boron

BE bottom electrode

BP bandpass

BS beam splitters

BZ The first Brillouin zone

C Carbon

C capacitance

C optical contrast

CB Conduction band

CBM Conduction band minimum

CCD charge-coupled device

CD conductive filament

CMOS metal-oxide-semiconductor

CNP Charge Neutrality Point

Cond condenser

Cr Chromium

CVD chemical vapour deposition

d thickness

D (E) density of states

DFT Density Functional Theory

DI deionized water

DiF drop-in-filters

DR double resonant

DRAM Dynamic random-access memory

E Electric field

E_b exciton binding energy

EDX energy-dispersive X ray

E_F Fermi level

E_g Energy bandgap

EL Electroluminescence

E_o optical bandgap

FET Field-effect transistor

FETT field-effect tunnelling transistor complementary

FM flip mirror

FWHM full width at a half maximum

Ge Germanium

h-BN and hBN hexagonal boron nitride

HfO_x Hafnium oxide

HfS_2 Hafnium disulphide

$HfSe_2$ Hafnimum diselenide

HRS high resistance state

I_{sd} source-drain current

In_2Se_3 Indium selenide

IPA isopropanol

k_F Fermi momentum

LA Longitudinal acoustic branch

LED light-emitting-diode

LEQW light-emitting quantum well

LRS low resistance state

M Metal

M fixed mirrors

MeO_x metal oxide

M_{xy} kinematic

MIM metal-insulator-metal

Mo Molybdenum

MoS_2 Molybdenum disulphide

MQW multiple quantum well

N Number of layers

N Nitrogen

n carrier density

ND neutral density filters

NIS Nikon elements Microscope Imaging software

O Optical branch

P_c Degree of polarisation

PD Photodetectors

PDMS polydimethylsiloxane

PL Photoluminescence

PMMA polymethyl methacrylate

PPC polypropylene carbonate

PVA Poly vinyl alcohol

Q and **q** charge

R Reflectance

R(λ) Reflected light

RRAM Resistive switching random access memory

S Sulphur

Se Selenium

Si Silicon

SiO_2 Silicon dioxide

SOC Spin-Orbit Coupling

SPCM Scanning Photocurrent Microscopy

SQW single quantum well

SR single resonant

T Transmittance

TA Transversal Acoustic branch

TE top electrode

Te Tellurium

Ti Titanium

TL Atomic trilayer structure

TMDC Transition metal dichalcogenides

TO Transversal optical branch

TR tripe resonant

UV ultraviolet

VB Valence band

VBM Valence band maximum

vdW van der Waals

v_F Fermi velocity

V_g gate voltage

V_{sd} source-drain voltage

V_{th} threshold voltage

W Tungsten

X Chalcogen

ZA Out-of-plane acoustic branch

ZO Out-of-plane optical branch

$ZrSe_2$ Zirconium diselenide

κ,ε Dielectric constant

ε_r relative dielectric permittivity

ε_0 Vacuum dielectric permittivity

Δ_{so} Spin-splitting for the conduction band

σ electrical conductivity

ρ resistivity

μ mobility

1L-graphene monolayer graphene

1L-WS_2 monolayer tungsten disulphide

1L-WSe_2 monolayer tungsten diselenide

1T Octahedral

2D Two-dimensional materials

2H Trigonal prismatic

Chapter 1: Introduction

1.1 Semiconductors

The first semiconductor (Germanium, Ge) transistor was made by John Bardeen and Walter Brattain under Shockley's direction in 1947 (1) and since then, the size of the transistors have been decreasing according to Moore's law (1965) first presented in the journal *Electronics*. This states that *the number of transistors per silicon chip would double each year* (2). Later, around 1960, Silicon (Si) took over as a raw material for electronics as it is an abundant element on planet Earth and its manufacturing processes are low cost. Contrary to most of the semiconductors Silicon has another desired property that is silicon dioxide (SiO_2); it is an excellent dielectric material which can easily be grown on the surface of a Si wafer through the exposure to oxygen. It is therefore not surprising that Si underpins the vast majority of the global market semiconductor technology. However, the push for novel applications in flexible and wearable electronics has now created a demand for novel materials with high mechanical flexibility, stretchability, optical transparency, thermal conductivity and semiconducting properties. Emerging atomically thin materials combine the aforementioned list of diverse and unique physical properties which are attracting an exponentially growing interest by a wide scientific community, inspiring the discovery of significant novel fundamental science such as the discovery of the high temperature condensation of charge excitations known as a condensate of excitons.

Graphene is the first and most studied atomically thin material, first isolated in its monolayer form (1L-graphene) in 2004 by Andrea Geim and Kostia Novoselov, (3). Interestingly, the electronic structure of graphene was theoretically described in 1947, though the material was thought to be thermodynamically unstable (4). The discovery of graphene lead to the Nobel Prize in Physics in 2010 (5) marking a significant growth in the science of two-dimensional materials. Graphene has high mechanical strength (6), it is highly transparent (7) as monolayer graphene absorbs 2.3% of the incident visible light (7, 8) and it is an incredible thermal and electric conductor (9). Interestingly, it is compatible with the silicon-based electronics and photonics as a transparent electrodes in displays (10), photovoltaics (11), ultrafast lasers (8) and photodetectors (PD) (8, 12-14). Moreover, graphene is gapless which means that the light absorption covers a wide range of the energy spectrum (8). However, the lack of bandgap makes graphene not suitable for transistor applications since current cannot be switched off in this material through a simple electrostatic gating action (15, 16).

Semiconducting layered materials such as transition metal dichalcogenides (TMDCs) are appealing especially in their monolayer limit as they show different properties from their bulk counterparts (17). Monolayer TDMCs are direct-bandgap semiconductors with the optical bandgap in the visible and near-infrared spectral range (18), transparent and mechanical flexible (8, 18).Their bandgap can be tuned depending on the number of layers (N) (17) allowing the detection of a wide range of wavelength, complementing the range of applications targeted

by graphene (8). These materials have been used in a wide variety of fields; electronics (17) , photonics (17), optoelectronics (17), spintronics (17) and valleytronics (17, 19). The combination of graphene and TMDCs alongside with the layered dielectric hexagonal boron nitride (h-BN) leads to van der Waals (vdW) heterostructures (20) hybrid devices where graphene could be used as tuneable electrodes, h-BN for tunnel barriers (21) and TMDCs as photoactive material due to the strong light-matter interaction and photon absorption (8).

These devices have relied on Si/SiO_2 as a substrate and back gate such as: Dynamic random-access memory (DRAM) (22) and field-effect transistor (FET) to list a few (22). Nevertheless, the downscaling of transistors imposes requirements on the use of ultra-thin gate-oxide dielectrics (SiO_2 ~ 2nm as a minimum thickness value) which, on the other hand, suffer of significant leakage current (23) affecting the performance of devices (22). During the last years, h-BN has been used for different purposes like tunnel barriers (24) , gate (25) and substrate (21). Nonetheless, its dielectric constant (κ ~ 4) (26) is similar to that SiO_2 (κ ~ 3.9) (27) which prevents further downscaling of the devices. As an option, high-κ dielectric materials are proposed as they can have the same gate or higher capacitance as SiO_2 having more thickness range (28). Previously, some studies have been done on high-κ materials (hafnium diselenide ($HfSe_2$), zirconium diselenide ($ZrSe_2$)), on their native oxides (29) and hafnium oxide (HfO_x) as gate dielectric for molybdenum disulphide (MoS_2) FET (30) opening a new research field.

1.2 This thesis

In this work, novel devices based on high-κ *materials* (HfO_x) are introduced as well as their influence on the dielectric environment of the TMDCs when been embedded in van der Waals heterostructures moving forward in the field.

This thesis is divided in 6 chapters starting from the physical background necessary to understand the fundamental science of the light-matter interaction and electrical transport in the materials studied in this research. Hence, the fabrication and experimental characterisation techniques are presented, finishing with the results and the conclusions. In Chapter 2 the properties of the materials and description are reviewed such as the as the lattice structure, the phonon dispersion and energy bands. Chapter 3 contains the fabrication techniques used for making the challenging vdW heterostructures covering the whole procedure in detail and Chapter 4 describes the characterisation techniques applied to the samples including Raman and photoluminescence (PL). Following to the previous theoretical chapters, Chapter 5 and 6 summarise the result of the two projects of this thesis; Chapter 5 shows two interesting points; the photo-oxidation of hafnium disulphide (HfS_2) into hafnium oxide while being embedded in the vdW heterostructures and the devices fabricated containing it.

Knowing the multitude of opto-electronics applications that the monolayer and few-layer TMDCs have, the dielectric interaction of the exciton study is vital

therefore in Chapter 6, the dielectric environment impact on monolayer WSe_2 binding energy and quasiparticle bandgap is studied with different dielectric surrounding material. This is done analysing theoretically and experimentally the transmission spectra and its derivatives of different surrounding materials being greater and smaller than the monolayer WSe_2 stacked in different van der Waals heterostructures. Hafnium oxide (κ ~ 15) and the ferroelectric indium diselenide (α- In_2Se_3, κ ~ 17) are used as a high-κ dielectrics.

The results of this thesis show the possibility of including high-κ materials within opto-electronics devices stack as van der Waals heterostructures. These materials could be used as gate dielectric, tunnel barriers and so on leading into a new direction of the field.

Bibliography

1. Bardeen J, Brattain WH. The Transistor, A Semi-Conductor Triode. Physical Review. 1948;74:230-1.
2. Moore GE. Cramming more components onto integrated circuits, Reprinted from Electronics, volume 38, number 8, April 19, 1965, pp.114 ff. IEEE Solid-State Circuits Society Newsletter. 2006;11:33-5.
3. Novoselov KS, Geim AK, Morozov SV, Jiang D, Zhang Y, Dubonos SV, et al. Electric Field Effect in Atomically Thin Carbon Films. Science. 2004;306:666-9.
4. Wallace PR. The Band Theory of Graphite. Physical Review. 1947;71:622-34.
5. Geim AK, Novoselov KS. The rise of graphene. Nat Mater. 2007;6:183-91.
6. Lee C, Wei X, Kysar JW, Hone J. Measurement of the Elastic Properties and Intrinsic Strength of Monolayer Graphene. Science. 2008;321:385-8.
7. Nair RR, Blake P, Grigorenko AN, Novoselov KS, Booth TJ, Stauber T, et al. Fine Structure Constant Defines Visual Transparency of Graphene. Science. 2008;320:1308.
8. Koppens FHL, Mueller T, Avouris P, Ferrari AC, Vitiello MS, Polini M. Photodetectors based on graphene, other two-dimensional materials and hybrid systems. Nat Nanotechnol. 2014;9:780.
9. Butler SZ, Hollen SM, Cao L, Cui Y, Gupta JA, Gutiérrez HR, et al. Progress, Challenges, and Opportunities in Two-Dimensional Materials Beyond Graphene. Acs Nano. 2013;7:2898-926.
10. Bae S, Kim H, Lee Y, Xu X, Park J-S, Zheng Y, et al. Roll-to-roll production of 30-inch graphene films for transparent electrodes. Nat Nanotechnol. 2010;5:574-8.
11. Jiao T, Wei D, Liu J, Sun W, Jia S, Zhang W, et al. Flexible solar cells based on graphene-ultrathin silicon Schottky junction. Rsc Adv. 2015;5:73202-6.
12. Mueller T, Xia F, Avouris P. Graphene photodetectors for high-speed optical communications. Nature Photonics. 2010;4:297-301.
13. Kim CO, Kim S, Shin DH, Kang SS, Kim JM, Jang CW, et al. High photoresponsivity in an all-graphene p–n vertical junction photodetector. Nat Commun. 2014;5:3249.
14. Liu C-H, Chang Y-C, Norris TB, Zhong Z. Graphene photodetectors with ultra-broadband and high responsivity at room temperature. Nat Nanotechnol. 2014;9:273.
15. Liu Y, Duan X, Huang Y, Duan X. Two-dimensional transistors beyond graphene and TMDCs. Chem Soc Rev. 2018;47:6388-409.
16. Huang W, Luo X, Gan CK, Quek SY, Liang GC. Theoretical study of thermoelectric properties of few-layer MoS2 and WSe2. Phys Chem Chem Phys. 2014;16:10866-74.
17. Wang QH, Kalantar-Zadeh K, Kis A, Coleman JN, Strano MS. Electronics and optoelectronics of two-dimensional transition metal dichalcogenides. Nat Nanotechnol. 2012;7:699-712.
18. Raja A, Chaves A, Yu J, Arefe G, Hill HM, Rigosi AF, et al. Coulomb engineering of the bandgap and excitons in two-dimensional materials. Nat Commun. 2017;8:15251.
19. Mak KF, McGill KL, Park J, McEuen PL. The valley Hall effect in MoS2 transistors. Science. 2014;344:1489-92.
20. I.V. Grigorieva and A.K.Geim. Van der Waals heterostructures.Nat. 2013;499:419-425
21. Dean CR, Young AF, Meric I, Lee C, Wang L, Sorgenfrei S, et al. Boron nitride substrates for high-quality graphene electronics. Nat Nanotechnol. 2010;5:722-6.
22. Kingon AI, Maria JP, Streiffer SK. Alternative dielectrics to silicon dioxide for memory and logic devices. Nature. 2000;406:1032-8.
23. Taur Y. CMOS design near the limit of scaling. IBM Journal of Research and Development. 2002;46:213-22.

24. Withers F, Del Pozo-Zamudio O, Mishchenko A, Rooney AP, Gholinia A, Watanabe K, et al. Light-emitting diodes by band-structure engineering in van der Waals heterostructures. Nat Mater. 2015;14:301.
25. Hattori Y, Taniguchi T, Watanabe K, Nagashio K. Layer-by-Layer Dielectric Breakdown of Hexagonal Boron Nitride. Acs Nano. 2015;9:916-21.
26. Li LH, Santos EJG, Xing T, Cappelluti E, Roldan R, Chen Y, et al. Dielectric Screening in Atomically Thin Boron Nitride Nanosheets. Nano Letters. 2015;15:218-23.
27. Wilk GD, Wallace RM, Anthony JM. High-κ gate dielectrics: Current status and materials properties considerations. J Appl Phys. 2001;89:5243-75.
28. Osada M, Sasaki T. Two-Dimensional Dielectric Nanosheets: Novel Nanoelectronics From Nanocrystal Building Blocks. Adv Mater. 2012;24:210-28.
29. Mleczko MJ, Zhang C, Lee HR, Kuo H-H, Magyari-Köpe B, Moore RG, et al. $HfSe_2$ and $ZrSe_2$: Two-dimensional semiconductors with native high-κ oxides. Science Advances. 2017;3:1-9
30. Radisavljevic B, Radenovic A, Brivio J, Giacometti V, Kis A. Single-layer MoS_2 transistors. Nat Nanotechnol. 2011;6:147.

Chapter 2: Theoretical background and literature review

2.1 Introduction

In this chapter the theoretical concepts are reviewed to provide the underpinning theoretical background needed to interpret the experimental results presented in the following chapters. The chapter starts by presenting the lattice structure of graphene, its energy band and phonon dispersion. Subsequently, transition metal dichalcogenides are introduced with the same description sequence of graphene and a brief description of hexagonal boron nitride. The chapter is concluded with a discussion of the most relevant physical concepts to the devices presented in this thesis.

2.1 Graphene

In the late 1960s, around 40 materials with layered structure were known (1) one of them been graphene. Its electronic structure was predicted theoretically in 1947 (2) but it was not until 2004 that was first isolated from its counterpart graphite (3). Graphite is a well-known layered structure consisting of stacked layers of carbon (C) atoms arranged on a honeycomb structure (figure 2.2), known as graphene ("2D graphite" or "zero-gap semimetal") (4).

2.1.1 Lattice structure

Graphene is made by carbon atoms and its electronic configuration is $1s^2\ 2s^2\ 2p^2$ consisting in a total of 6 electrons, $1s^2$ being the core orbital that does not take part in the hybridization as it is tightly bound to the nucleus. Each carbon atom's 2s, $2p_x$ and $2p_y$ orbitals hybridize into three sp^2 coplanar (XY plane, see figure 2.1 (a)) orbitals separated by 120° so that the carbon atom resulting electronic configuration is $1s^2\ (2sp^2)^1\ (2sp^2)^1\ ((2sp^2)^1\ (2p_z)^1$ where the p_z orbital is in the perpendicular Z direction to the XY plane of the sp^2 orbitals. The p_z orbital has one electron per atom being the only electron which contributes to the electrical transport properties as the localized sp^2 electrons do not contribute to the low-energy electrical and thermal conductivity (2, 5) (see figure 2.1 (a)). When carbon atoms arrange to form the graphene lattice, the sp^2 orbital between neighbouring carbon atoms hybridise covalently giving σ bond with a distance of 1.42 Å between atoms (6) and p_z orbitals from neighbouring atoms hybridize covalently between them and form the π bonds as shown in figure 2.1 (b).

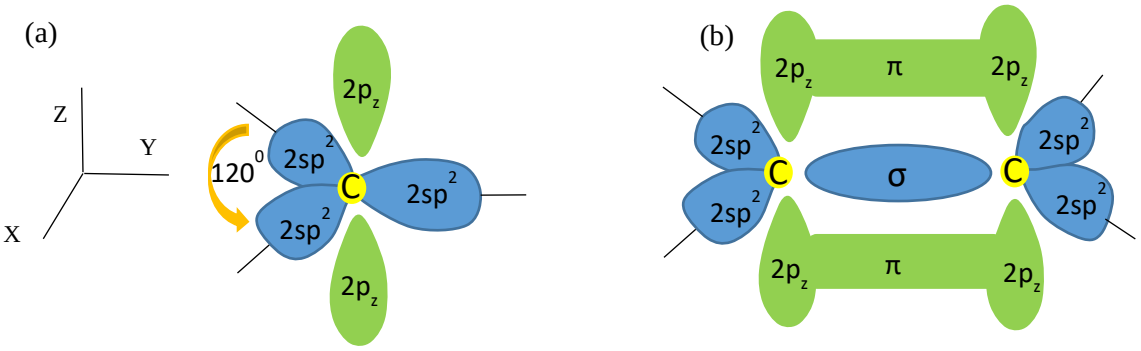

Figure 2.1: The $2sp^2$ and $2p_z$ orbitals hybridizations of carbon. (a) Hybridization of $2sp^2$ orbitals separated by an angle of 120° in blue, the remaining $2p_z$ in green and the carbon atom in yellow. (b) Hybridization of two neighbouring carbons in yellow with $2p_z$ orbitals in green forming π bond between them and $2sp^2$ orbitals in blue forming σ bond between them.

The honeycomb atomic structure of graphene consists of two interpenetrating and inequivalent triangular atomic sub-lattices (denoted in blue (A) and in yellow (B) colours in figure 2.2 (a) and in orange and green in figure 2.2 (b)). The atoms of this planar sheet are held together by covalent bonds whereas different sheets are bound by van der Waals interactions (7) with a layer thickness of 3.5 Å nm (8). The unit cell of the single layer has a basis of two atoms (A in blue and B in yellow) and is formed by the primitive vectors (6) as shown in figure 2.2 (a) by $\mathbf{a_1}$ and $\mathbf{a_2}$ with the following expression:

$$\mathbf{a_1} = \frac{a}{2}(3,\sqrt{3}),\ \mathbf{a_2} = \frac{a}{2}(3,-\sqrt{3}) \qquad (2.1)$$

where a ≈ 1.42 Å is the nearest-neighbour atoms distance. The three nearest-neighbours' atoms of each atom belong to a different sub-lattice as shown in figure 2.2 (a) from the atom taken as the origin with the following expression for their vectors in the real space:

$$\boldsymbol{\delta_1} = \frac{a}{2}(1,\sqrt{3}),\ \boldsymbol{\delta_2} = \frac{a}{2}(1,-\sqrt{3}) \text{ and } \boldsymbol{\delta_3} = -a\,(1,0) \qquad (2.2)$$

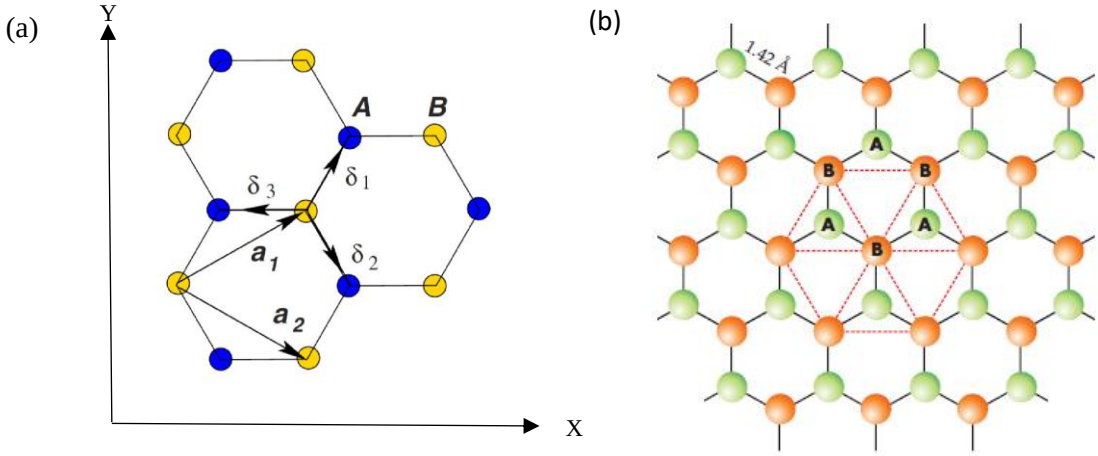

Figure 2.2: **Honeycomb atomic lattice structure of graphene in real space.** (a) Lattice structure with two triangular sub-lattices – blue (A) and yellow (B) – with the $\mathbf{a_1}$ and $\mathbf{a_2}$ primitive vectors and the nearest-neighbour vectors $\boldsymbol{\delta_i}$ =1, 2, 3. Reproduced with permission (6). (b) Expanded lattice structure with two triangular sub-lattices-green (A) and orange (B) denoted by triangles (9). Reproduced from [Physics Today 60, 8, 35 (2007)], with the permission of the American Institute of Physic.

The first Brillouin zone (BZ) of the reciprocal lattice of monolayer graphene has a hexagonal shape as shown in figure 2.3 with the reciprocal lattice vectors of (6):

$$\mathbf{b_1} = \frac{2\pi}{3a}(1, \sqrt{3}) \quad , \mathbf{b_2} = \frac{2\pi}{3a}(1, -\sqrt{3}) \tag{2.3}$$

The first Brillouin zone has several high symmetry points denoted by K and K' for the corners, Γ for the center and M for the midway between K and K' which are labelled in figure 2.3. These K/K' points are named Dirac points which will be clarified in section 2.1.2 and their positions are K = $(\frac{2\pi}{3a}, \frac{2\pi}{3\sqrt{3}a})$ and K' = $(\frac{2\pi}{3a}, -\frac{2\pi}{3\sqrt{3}a})$. There is one set of three K and another set of three K' in the first BZ (each set belonging to different sub-lattices), however, only two of them are not equivalent as the others are connected by the reciprocal lattice vectors (6).

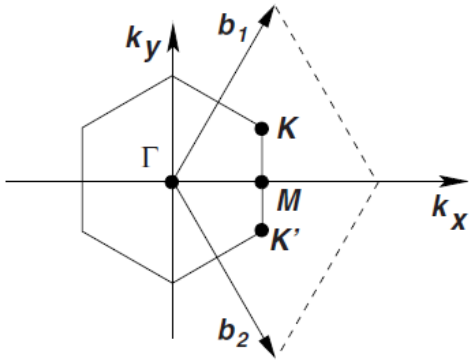

Figure 2.3: The first hexagonal Brillouin zone of monolayer graphene in the reciprocal space. The high symmetry points are denoted (K, K', M and with Γ) and the reciprocal lattice vectors are denoted by $\mathbf{b_1}$ and $\mathbf{b_2}$. Reproduced with permission (6).

2.1.2 Energy bands

The electronic dispersion of monolayer graphene for the honeycomb lattice structure of figure 2.2 can be calculated using the tight-binding method that was proposed by Bloch in 1928 for solid-state physics (10). This method consist of the calculation of the electronic band structure based on a set of wavefunctions expressed as a linear combination of the wavefunctions for the orbitals of atoms in the base. Following the work of Wallace in 1947 (6) and taking into account the primitive and reciprocal vectors and the three nearest-neighbour vectors (see section 2.1.1), the energy bands for the nearest-neighbour atoms are described by:

$$E_{\pm}(\boldsymbol{k}) = \pm t\sqrt{3 + 2\cos\left(\sqrt{3}k_Y a\right) + 4\cos\left(\frac{\sqrt{3}}{2}k_Y a\right)\cos\left(\frac{3}{2}k_X a\right)} \tag{2.4}$$

where t ≈ 2.8 eV is the nearest-neighbour hopping energy between the two sub-lattices and the plus (minus) sign is for the upper-conduction (lower-valence) bands (6).
A plot of the electronic band structure of monolayer graphene is shown in figure 2.4 where the energy in the reciprocal space is shown for the valence (VB, π) and conduction (CB, π^*) bands emerging from the overlap between the p_z orbitals of neighbouring atoms. The corners of the Brillouin zone are denoted by K and K' and at low energies (6) and the energy dispersion is linear with the momentum

$E_{\pm} = \pm \hbar v_F k$ (4, 8, 11) where ħ is the reduced Planck constant, k is the momentum and $v_F \sim 10^6$ m/s the Fermi velocity (4, 6). Therefore, the electrons mimic the massless Dirac fermions and are governed by the Dirac equation due to the interaction between the electrons and the honeycomb lattice (12)- naming K and K' Dirac cones. For undoped graphene the Fermi level lies at the charge neutrality point (CNP) which is the crossing point from the valence to the conduction band with no energy bandgap. The absence of an energy gap is due to the energetic equivalent carbon atoms in the A and B sub-lattices. By breaking the symmetry of the on-site energy between the A and B atoms, it is possible to engineer the opening of an energy gap, otherwise graphene is energy gapless.

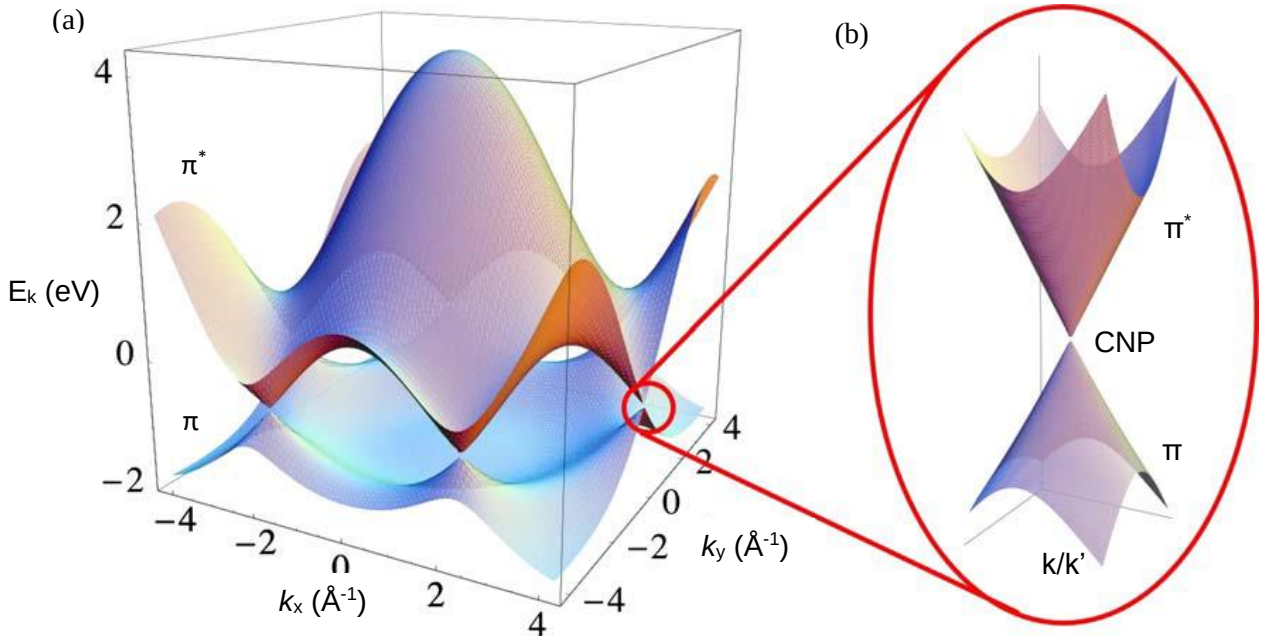

Figure 2.4: Energy bandstructure of monolayer graphene. (a) The electronic dispersion for the nearest-neighbour and next-nearest neighbour atoms in the first Brillouin zone showing the conduction band (π*) and valence band (π). (b) Zoomed Dirac cones (K/K') showing the charge neutrality point (CNP) with the conduction and valence bands. Reproduced with permission (6).

2.1.3 Phonon dispersion

Monolayer graphene has two atoms per unit cell (7) that belong to two different sub-lattices (figure 2.5 (a) in red and blue colours) and each of them has three degrees of freedom leading to six phonon modes as is shown in Figure 2.5 (b). These modes are classified in two sets. The first group consists of three acoustic (A) branches (ZA, TA and LA), whilst the second consist of three optical (O) branches (ZO, TO and LO), where L (T) stands for longitudinal (transversal) polarisation and they are in-plane whereas Z mode has out-of-plane polarisation and can be named flexural modes (13). LO and TO are degenerate in energy at the Γ point which will be important for the Raman G peak in Chapter 4. As shown in figure 2.5 (b), acoustic phonons have lower frequency than optical phonons and for the case of large wavelength compared to the atoms spacing, the frequency shows a linear dispersion in the wave vector (14). Acoustic modes cannot interact with electromagnetic radiation unlike optical phonons that can interact for long wavelengths (14).

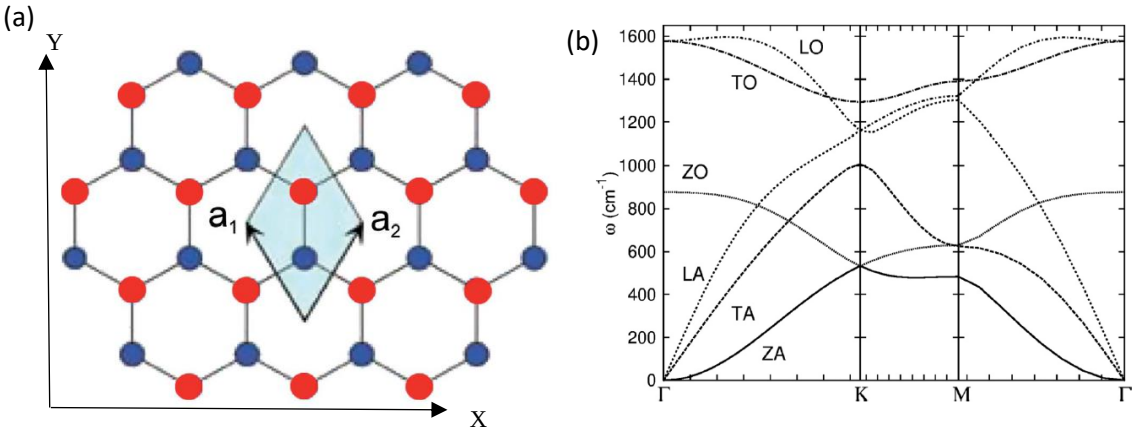

Figure 2.5: Monolayer graphene lattice and phonon dispersion. (a) Honeycomb lattice in real space with the unit cell in blue defined by the vectors $\mathbf{a_1}$ and $\mathbf{a_2}$ and one sub-lattice in red and the other one in blue. Reproduced with permission (15). (b) Phonon dispersion along the line ΓK-MΓ with the modes branches: acoustical (ZA, TA and LA) and optical (ZO, TO and LO). Reproduced with permission (13).

2.2 Transition metal dichalcogenides

Shortly after the discovery of graphene, other two-dimensional materials raised to the attention of a wide scientific community. Of these, the semiconducting transition metal dichalcogenides are presently generating a growing interest owing to their unique range of properties such as: layer-dependent indirect-to-direct energy bandgap transition (16, 17), coupled spin and valley physics (18), valley polarization (19, 20). Due to these properties, they have been implement in a wide variety of devices such as light-emitting diodes (21, 22), flexible and transparent sensors (23).

2.2.1 Lattice structure

Layered transition metal dichalcogenides are compounds with the chemical formula MX_2 where M is a transition metal from the group IV,V and VI and X is a chalcogen (16). For semiconducting TMDCs, Molybdenum (Mo) and Tungsten (W) stand for the metal and Sulphur (S), Selenium (Se) and Tellurium (Te) for the chalcogen (24). These materials can be presented in two phases: hexagonal symmetry with trigonal prismatic coordination (2H) and tetragonal symmetry with octahedral coordination (1T), for this work TMDCs are presented in 2H phase, however, HfS_2 is presented in 1T phase where the hafnium atoms plane are in the midway between the planes of the sulphur atoms leading to an hexagonal lattice as seen from the top as shown in figure 2.6 (c).

A monolayer TMDC is made by three atomic planes (X-M-X) where intralayer M-X bonds are bounded by strong covalent forces named atomic trilayer structure (TL) (25) with each layer ~ 6 Å thick (26) that can be exfoliated by micromechanical cleavage. Monolayer TMDCs lattice structure has a hexagonal shape made by two triangular sub-lattices as shown in figure 2.6 (a) and are weakly held together by van der Waal's forces for few-layers up to bulk, being the case of trilayer in figure 2.6 (b) (16).

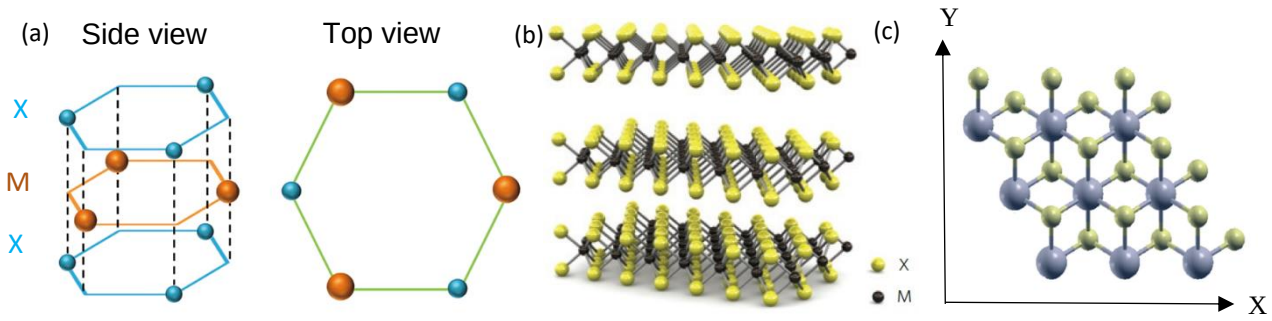

Figure 2.6: TMDCs atomic lattice structure for the 2H and 1T phases. (a) Monolayer (X-M-X) side and top view with metal layer in orange (M) and chalcogen layers (X) in blue. Reproduced with permission (27). (b) Trilayer structure stacked by three monolayers (X-M-X) with metal layer (M) in black and chalcogen layer (X) in yellow for the 2H phase. Reproduced with permission (16). (c) Atomic lattice structure in 1T crystal phase for monolayer HfS_2. Sulphur atoms in yellow and hafnium atoms in blue [*Catal. Sci. Technol.*, 2016; 6, 6605-6614] – Reproduced by permission of The Royal Society of Chemistry (54).

The lattice structure of monolayer TMDCs has a hexagonal shape as shown in figure 2.6 (a) for the top view containing three different planes: two chalcogen planes where the atoms from the two planes sit on top of each other and the metal plane being in the middle plane. The unit cell is defined by the lattice vectors $\mathbf{a_1}$ and $\mathbf{a_2}$ containing three atoms as a base as shown in figure 2.7 (a) (28).

The first Brillouin zone is hexagonal as shown in figure 2.7 (b) with four high-symmetry points (K, K', M and Γ) with Q being approximate a local minimum of the conduction band (29, 30) and K and K' points named valleys (31) being inequivalent in the Brillouin zone.

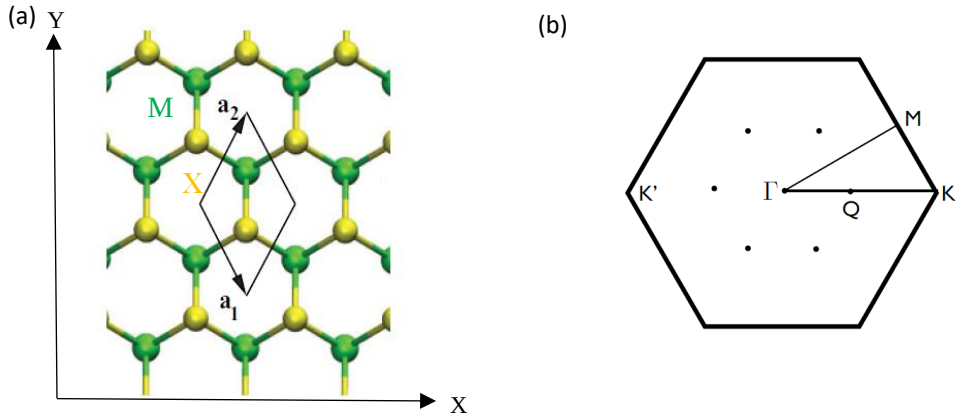

Figure 2.7: Monolayer TMDCs atomic lattice structure for the 2H-phase and Brillouin zone. (a) Top view of the atomic lattice structure showing two sub-lattices in green for the metal (M) and yellow for the chalcogen (X) containing the unit cell with the primitive vectors $\mathbf{a_1}$ and $\mathbf{a_2}$ .Reproduced with permission (29). (b) The hexagonal first Brillouin zone with the high symmetry points K, K', M and Γ and the six Q points for a local minimum of the conduction band. Reproduced with permission (30).

Considering the electronic configuration of the transition metal Mo and W; Mo: [Kr] $4d^5\ 5s^1$ and W: [Xe] $4f^{14}\ 5d^4\ 6s^1$ they have d orbitals which is the origin of spin-orbit coupling (SOC) (32, 33). Spin-orbit coupling describes the interaction between the magnetic field created by the relative motion between the electron and nucleus and the spin of the electron leading to a change in the energy levels

of the electron in the atoms. Due to the spin-orbit coupling, monolayer TMDCs have a spin-splitting in the valence and conduction bands along the line Γ-K of the Brillouin zone breaking the spin degeneracy (24) where the spin splitting is more pronounced for tungsten than molybdenum as the atoms are heavier (24, 30). The strong spin-splitting of the valence band would make possible to use TMDCs in spintronics for storing and manipulating the spin degree of freedom of electrons (26).

Monolayers TMDCs show broken inversion symmetry and the electron motion is confined in the plane of the material. Inversion (i) symmetry is defined as an operator that reproduces the crystal under the transformation r → -r from every single point of the crystal which means that for the point (x,y,z) transforms into (-x,-y,-z) taking the center of the crystal as the origin-inversion center- in the midway between two atoms. Graphene has an inversion symmetry as setting the center of the lattice as the inversion center and pointing one carbon atom with a vector and inverting it there is another carbon atom in the same plane as shown in figure 2.8 (a). However, for monolayer TMDCs a vector pointing the metal atom, points to a vacant point after being inverted as the metal and chalcogen atoms are in different planes as shown in figure 2.8 (a). Therefore, monolayer TMDCs do not possess inversion symmetry –i.e. show broken inversion symmetry- unlike for bilayers where the inversion symmetry is between both monolayers as shown in figure 2.8 (b). The inversion symmetry dictates the energy dispersion as discussed in section 2.1.2 for graphene and in the following section 2.2.2 for TMDCs. The link between the inversion symmetry and the energy dispersion can be explained in this way: in graphene, electrons with same momenta modulus but opposite sign have the same energy value as the inversion symmetry is preserved, for monolayer TMDCs, however, electrons have different value in energy.

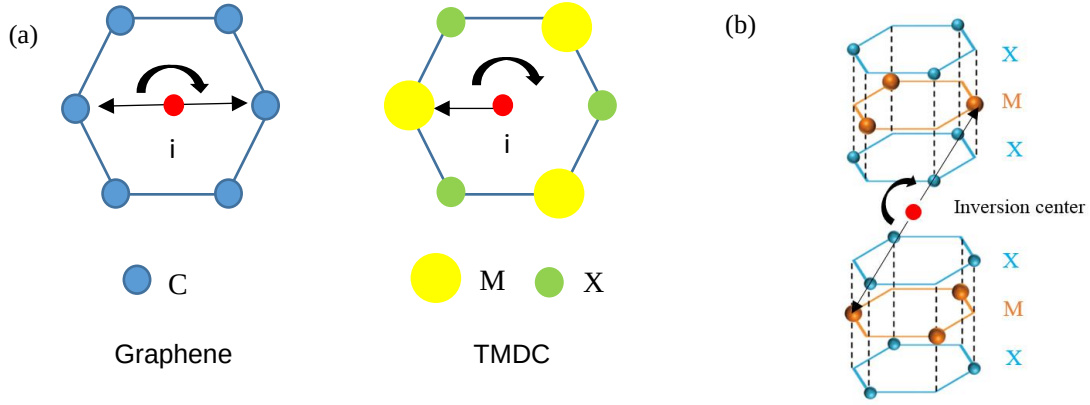

Figure 2.8: Inversion symmetry for graphene and TMDCs. (a) Monolayer graphene structure with carbon atoms in blue circles, monolayer TMDCs with metal (chalcogen) atoms in yellow (green) circles and inversion center in red for top views of the hexagonal lattice structure. Graphene shows inversion symmetry as both vectors from the inversion center are in the same plane pointing carbon atoms once that are inverted whereas for monolayer TMDC the vector pointing the metal does not point another metal when is inverted as there is a vacant in that plane being lack in inversion symmetry. (b) Bilayer TMDCs with the metal (chalcogen) atoms in (orange) blue circles and the inversion center in red where the vector points one metal atom from the top monolayer. After being inverted, the vector points another metal atom from the bottom monolayer meaning that the inversion symmetry is preserved for bilayer TMDCs.

Monolayers TMDCs show valley-contrasting optical selections rules in K and K' of Brillouin zone as a consequence of broken inversion symmetry (19) and combined with the strong spin-orbit coupling leads to the coupled spin and valleys physics (19). Therefore, by choosing the polarisation of the incoming light, it is possible to populate only one valley as the light couples to the K and K' valleys differently. Indeed, the right-handed circularly polarised excited light (σ+) couples to K valley whereas the left-handed circularly polarised excited light (σ-) couples to K' valley. Hence the absorption of polarised light can lead to an imbalance of the population of charges between valleys also known as valley polarisation (19, 34). The polarisation of the emitted luminescence follows the polarisation of the incoming excited light; right (left)-handed circularly polarised excited light generates right (left)-handed luminescence as shown in figure 2.9 (19). The degree of polarisation (Pc) of the emitted circular polarised luminescence is characterised by Pc= $(I_{\sigma+} - I_{\sigma-})/ (I_{\sigma+} + I_{\sigma-})$ where $I_{\sigma+}$ ($I_{\sigma-}$) is the emitted intensity of the right (left)-handed circular component luminesce (19). The possibility of controlling the degree of freedom of the charge carries in K and K' valleys for monolayers TMDCs makes them suitable for valleytronics where the valley degree of freedom is used for information storage (26).

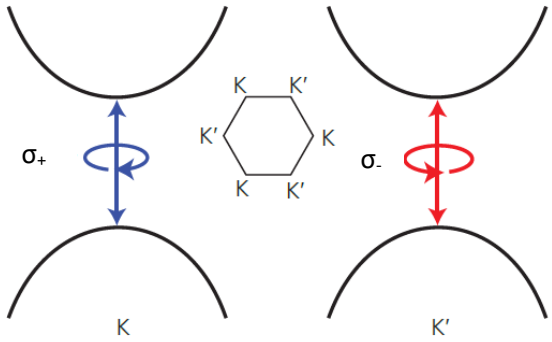

Figure 2.9: Optical selection rules for monolayer TMDCs. K valley couples to right-handed circularly polarised excited light (σ+) whereas K' valley couples to left-handed circularly polarised (σ-) excited light due to the broken inversion symmetry. In the middle the hexagonal first Brillouin zone with the valleys K and K' in the corners. Reproduced with permission (19).

2.2.2 Energy bands

As explained in section 2.2.1, the conduction and valence bands in the K and K' points of the Brillouin zone for monolayer TMDCs show spin-splitting due to the strong spin-orbit coupling as shown in figure 2.10 (a). For figure 2.10 (a) the conduction band spin-splitting was neglected as is smaller than the spin-splitting of the valence band. The splitting of the valleys is related by time reversal symmetry which means that they show opposite spin-splitting of the conduction and valence bands to one another valley (25, 33, 35). Figure 2.10 (b) shows the spin-splitting in K and K' valleys for the conduction and valence bands in WX_2 compounds where the fundamental energy bandgap (E_g) and the spin-splitting for the conduction band (Δ_{SO}) are denoted. For MoX_2 compounds, the spin-splitting of the conduction band is opposite to WX_2 compounds shown in figure

2.10 (b) (22). These band are theoretically calculated using the Density Functional Theory (DFT) (35, 36).

The split has been calculated for monolayers MoS_2 and WSe_2 in a valence band with the values of 0.15 eV and 0.46 eV respectively as the magnitude of the intrinsic spit-orbit coupling of tungsten is bigger than molybdenum (37), due to the fact that tungsten is a heavier element than molybdenum, whereas the values of the split for the conduction band is ~ 40 meV for both (20).

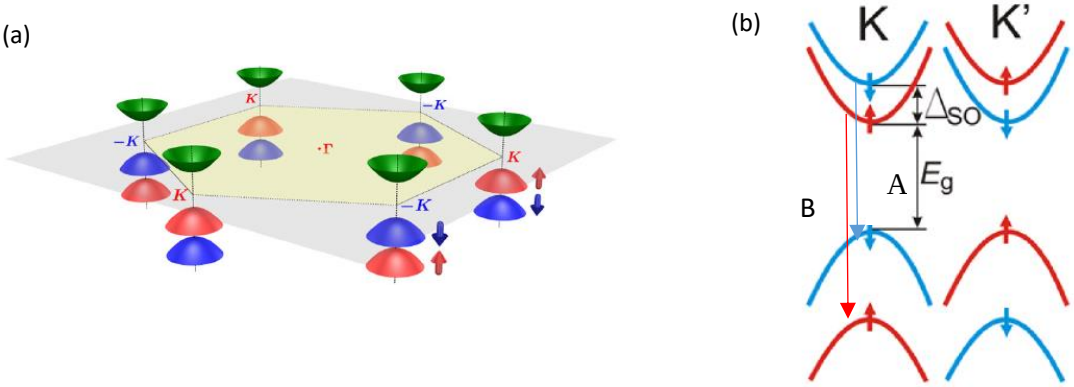

Figure 2.10: Monolayer TMDCs energy bands for the valleys: (a) Schematic drawing of the band edges within the Brillouin zone where the conduction bands are in green, valence bands are in blue and red for the spin orientation. Reproduced with permission (18). (b) Band diagrams with the spin-splitting for the K and K' valleys for compounds WX_2. E_g denotes the fundamental energy bandgap and Δ_{SO} denotes the spin-split for the conduction band. The spin orientation follows the same colour code and optical transition. Reproduced with permission (22).

The bandgap of the TMDCs undergoes an indirect-to-direct crossover from a few-layers to monolayer limit (16). Most bulk TMDCs have an indirect bandgap from the valence band maximum (VBM) at Γ point to a conduction band minimum (CBM) at midway between Γ and K as shown in figure 2.11 (a). However, monolayer TMDCs have a direct bandgap in K as is shown in figure 2.11 (b) as the quantum confinement increases in the out-of-plane direction.

Taking MoS_2 as an example in figure 2.11, the transition can be explain as the change in the hybridization between the pz orbitals on S atoms and d orbitals on Mo atoms (16). The conduction bands in the K point are made of localised d orbitals of the Mo atoms and they are in the middle of the S-Mo-S layers so they are not very affected by the interlayer coupling (16). The states that are at the Γ point, however, are made of pz orbitals of the S atoms and d orbitals of the Mo atoms which leads to strong interlayer coupling (16). Upon reducing the number of layers from the bulk crystal down to the monolayer limit the bands at the K point remain unchanged while the bands in the Γ point change so that the bandgap becomes direct (16).

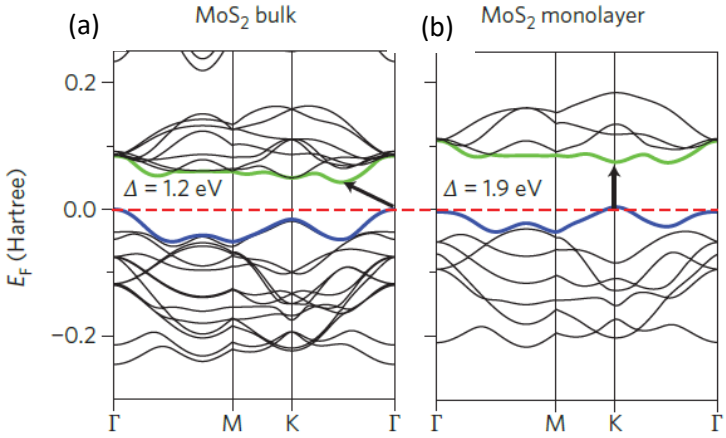

Figure 2.11: Energy bandstructure of MoS_2 for the line ΓK-MΓ calculated from first-principles Density Functional Theory. (a) MoS_2 bulk band diagram with indirect bandgap. (b) Monolayer MoS_2 with direct bandgap. The top valence band in blue and the bottom conduction band in green where the arrow pointing out the fundamental energy bandgap between this bands. The Fermi level is indicated by red dashed lines and the fundamental bandgap is indicated by Δ. Reproduced with permission (16).

2.2.3 Phonon dispersion

Monolayer TMDCs like MoS_2 have three atoms per unit cell (see section 2.2.1) each of them having three degrees of freedom leading to nine phonon modes as is shown in Figure 2.12. These modes are classified like this: three acoustical branches (ZA,TA and LA) and six optical branches (ZO1, ZO2,TO1, TO2, LO1 and LO2) (38) where T (L) denotes the transversal (longitudinal) modes and Z denotes the out-of-plane mode. They have another notation-irreducible representation-which will be used for Raman in Chapter 4: E'' (LO1 and TO1), E' (LO2 and TO2), A_2'' (ZO2) and A_1' (ZO1).

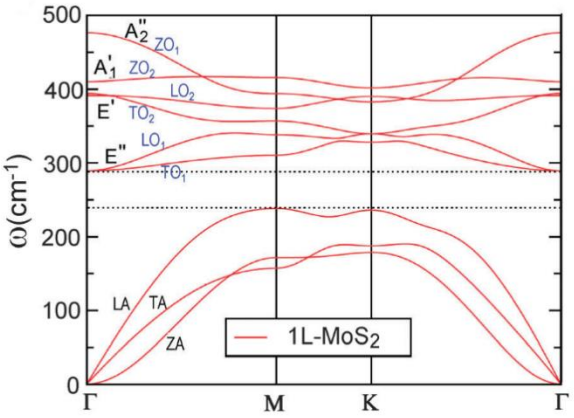

Figure 2.12: Phonon dispersion of monolayer MoS2 (1L-MoS2) along the line ΓK-MΓ. Low acoustic branches (ZA, TA and LA) and upper optical branches (ZO1, ZO2, TO1, TO2, LO1 and LO2) with the irreducible representation E'' (LO1 and TO1), E' (LO2 and TO2), A_2'' (ZO2) and A_1' (ZO1) [Chem Soc Rev. 2015; 44(9):2757-85] – Reproduced by permission of The Royal Society of Chemistry (38).

2.3 Hexagonal boron nitride

Hexagonal boron nitride is another 2D material that has a honeycomb lattice structure as shown in figure 2.13–similar to graphene. Three sp^2 orbitals of each boron (B) atom combine with the sp^2 orbitals of nitrogen (N) forming a σ bond by covalent forces with B-N bound of 1.45 Å (8). These layers are held together by weak van der Waals forces (8) and h-BN has a direct bandgap around 5.9 eV which means that it is an insulator (8).

This material does not absorb visible light, however, it has absorption in the ultraviolet region (8). Moreover, the crystal structure of h-BN is almost commensurate to that graphene, as the lattice mismatch is only 1.7 %. This makes interfaces of graphene to h-BN highly interesting van der Waals heterostructures (39).

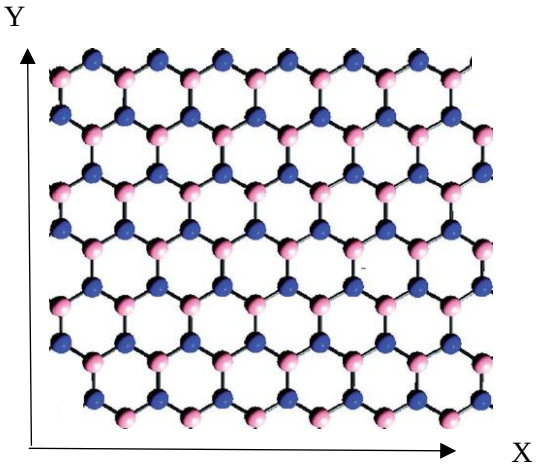

Figure 2.13: h-BN hexagonal lattice atomic structure in real space. Nitrogen atoms are depicted by blue spheres and boron atoms in pink in white spheres. [Rsc Adv. 2017; 7(27):16801-22] – Reproduced by permission of The Royal Society of Chemistry (8).

2.4 Transistor and memory devices based on 2D materials

2.4.1 Field effect transistor

Field-effect transistor uses the electric field (E) originated in the capacitor for controlling the conductivity of the channel. This device consists on the source, drain, channel and the gate. The most common FET is the MOSFET where the M stands for the source and drain metal contacts, O for the oxide (dielectric gate insulator) and S for semiconductor channel. If the substrate is Si/SiO_2, the schedule is the one shown in figure 2.14 where the SiO_2 is the dielectric between the silicon (the back gate) and the semiconductor channel (2D material for this project) which means that there is a capacitor between the channel and the silicon with a dielectric in between. Normally in most devices, the global back gate consists of a highly p-doped Si substrate coated by a ~280-300 nm thick thermally-grown SiO_2 (40).

A source-drain voltage bias is applied between the source and drain (V_{sd}) and a non-zero source-drain current (I_{sd}) flows in the device upon increasing V_{sd} to larger values than threshold voltage (V_{th}), which is the minimum gate-to-source voltage needed to enable conduction in the semiconducting channel, see figure 2.14. The back-gate voltage (V_g) is applied to the heavily doped silicon substrate ensuring the electrostatic control of the free charge carrier density and therefore of the electrical conductivity of the semiconductor. Selecting the polarity of the back-gate voltage, the type of carries can be selected: holes or electrons. Therefore, if a positive (negative) gate voltage is applied to the Si substrate, electrons (holes) are accumulated in the semiconducting channel.

In the case of undoped graphene, a negative back gate voltage results in the accumulation of holes which corresponds to a shift of the Fermi level (i.e. the energy of the highest occupied state, E_F) to the valence band. In this condition, the majority of the carriers of the channel are holes (p-doped channel) whereas for positive voltages the fermi level is shifted to the conduction band the majority of the carriers are electrons (n-doped channel).Therefore graphene shows an ambipolar behaviours (4).

In the following, I provide a more quantitative analysis of the relation between the applied voltage to the gate and the density of free surface charge carrier density (n) accumulated in the semiconductor channel. The system consisting of heavily doped Si/SiO_2/semiconductor FET can be modelled as a parallel plate capacitor in which one armour plate is the Si substrate whereas the second armour plate is the semiconductor and the SiO_2 of thickness d is the dielectric medium with relative dielectric permittivity ε_r. The expression relating the voltage V, charge accumulated on the armour plates Q and the capacitance C is:

$$C = Q/V = Q/E \cdot d \tag{2.5}$$

where E the electric field. The capacitance per unit area can be written as (41):

$$C = \varepsilon_0 \varepsilon_r / d \tag{2.6}$$

Hence, the charge density accumulated in the semiconductor is given by:

$$n = \varepsilon_0 \varepsilon_r V_g / d \cdot q \tag{2.7}$$

where q the electron charge, V_g the back gate voltage, d is the thickness of the dielectric and ε_0 is the vacuum permeability. For graphene the equation can be written like n = α Vg where the α coefficient ≈ 7.2x1010 $cm^{-2}\,V^{-1}$ for a FET with 300 nm SiO_2 dielectric (4).

The electrical conductivity (σ) has the following expression:

$$\sigma = 1/\rho \tag{2.8}$$

where ρ is the resistivity. Moreover, the conductivity can be derived from the Drude model (3, 14, 42) as follows:

$$\sigma = nq\mu \tag{2.9}$$

where n is the carrier concentration, q is the electron charge and μ is the mobility.

Rearranging these formulas and using equations 2.9 and 2.7 the conductivity can be written as follows:

$$\sigma = (\varepsilon_0 \varepsilon_r V_g/d)\mu \quad (2.10)$$

The fermi energy of graphene can be expressed as follows for the Dirac cones at low energies:

$$E_F = \pm \hbar v_F K_F \quad (2.11)$$

Where the fermi momentum has the following expression $k_F^2/\pi = n$, and re-writing the fermi energy:

$$E_F = \pm \hbar v_F \sqrt{n\pi} \quad (2.12)$$

The density of states for monolayer graphene is related to the charge density as follows:

$$D(E) = \frac{2\sqrt{n}}{\sqrt{\pi}\,\hbar\, \nu F} \quad (2.13)$$

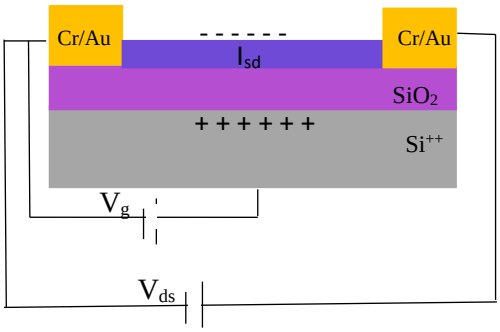

Figure 2.14: MOSFET with the circuit. The voltage (bias V_{sd}) is applied between source and drain metal contacts and the back gate voltage (V_g) is applied to silicon back gate for modulating the conductivity and current (I_{sd}) of the channel. The source and drain contacts (Cr/Au) are in orange, p-doped Si++ in grey, SiO_2 in pale purple, the channel in dark purple, positive charges are indicated for the polarity of the back gate voltage, negative charges for the induced charges in the channel.

2.4.2 Resistive switching random access memory

Resistive switching random access memory (RRAM) are non-volatile memory devices in which information is stored in specific resistive states (43). The structure of these devices consists on one layer of insulator material or named metal oxide (MeO_x) sandwiched (metal-insulator-metal, MIM) between two metal electrodes (TE-top electrode, BE-bottom electrode) as shown in figure 2.15.

These devices are described by the Set and Reset process as shown in figure 2.16. In the Set process the system undergoes a transition from a high resistance state (HRS) to a low resistance state (LRS). On the other hand, in the Reset, the system experiences a transition from the LRS to HRS being HRS the OFF state for the device and LRS the ON state. The bias is applied between the electrodes so that the resistance of the oxide is electrically stimulated and a current-compliance (Ic) is set for avoiding permanent dielectric breakdown of the oxide (44, 45).

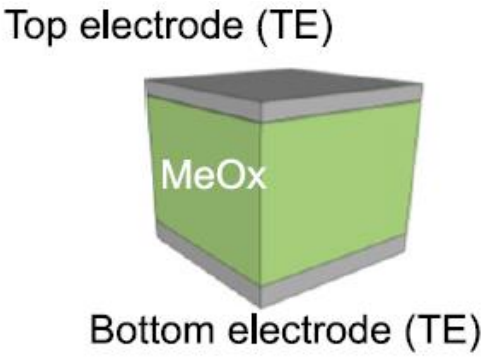

Figure 2.15: **RRAM device structure.** The oxide (MeOx) is in green colour, top (TE) and bottom (BE) electrodes in grey colour. Reprinted with permission from (46), Copyright (2014) John Wiley & Sons, Inc.

There are two types of RRAM (figure 2.16) : bipolar switching-antisymmetric (see figure 2.16 (b))- the Set and Reset process are achieved with opposite voltage polarities (47) and normally they have some asymmetry on the structure-different electrode material- (45). The second type is unipolar switching (see figure 2.16 (a)), which use the same polarity for achieved Set and Reset process, therefore the switching direction depends on the amplitude of the voltage (48).

In this thesis, I focus on bipolar switching memories shown in figure 2.16 (b). At the beginning the device is in the HRS (OFF) state and the positive voltage is applied where the current reaches Ic. At that point, the device reaches the LRS (ON) state in the Set process (blue curve in figure 2.16 (b)). Afterwards, the voltage is decreased dropping the current while the LRS state is kept until the voltage is reversed reaching a HRS state known as Reset process in which the device if OFF for low currents (red curve in figure 2.16 (b)). Therefore, the Set process starts from HRS state to LRS under positive voltage whereas Reset starts from LRS to HRS under negative bias.

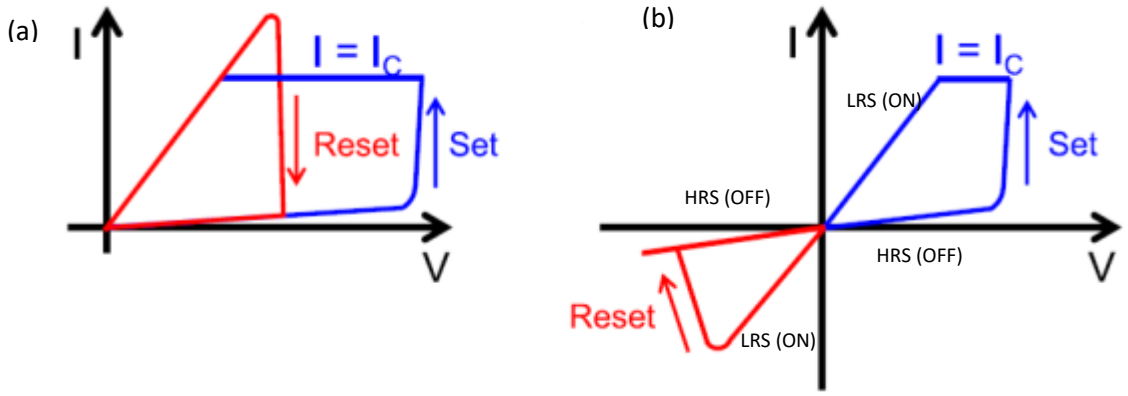

Figure 2.16: Two types of RRAM. (a) Unipolar switching: Set and Reset process are achieved under the same voltage polarity. (b) Bipolar switching; Set and Reset are reached under opposite voltage polarities. Reset process is in red, set in blue and I_C for the current compliance. Reprinted with permission from (46), Copyright (2014) John Wiley & Sons, Inc.

When the memories are based on oxides, the mechanism is based on the formation/ reversible rupture of the conductive filaments (CD) where the oxygen vacancies take part (43). Normally these devices' resistance is very high at the beginning so there is the need of an initial large voltage higher than the Set voltage of the following cycles (48) to switch on –electroforming process (49). In the electroforming process the oxide undergoes a soft dielectric breakdown creating the conductive filament (48). After the CD forming, the first Reset process is achieved with partially broken "disconnected" conductive filaments reaching the HRS state (50, 51). The first Set process, TE and BE are connected by the conductive filament with low resistance reaching the LRS state. These CDs can be connected and disconnected during multiple cycles going from Set to Reset.

In more detail, the mechanism can be understood as follows: a positive voltage is applied to the TE for the electroforming step before the repeatable resistive switching where the oxygen anions accumulate underneath the TE oxidising it, leaving behind positively charge oxygen vacancies (44) as shown in figure 2.17. Normally a "capping layer" such at Titanium (Ti) is used between the top metal electrode and oxide for attracting the oxygen anions to it (44). Afterwards, applying a reversed voltage to TE so that previously accumulated oxygen anions underneath TE migrate towards BE recombining with the vacancies from the oxide. In this process the conductive filament is partially ruptured and the device reaches the HRS state and dropping the current (44, 50, 52). Applying a positive voltage to TE, the oxygen anions migrate from the oxide towards TE like in the electroforming process.

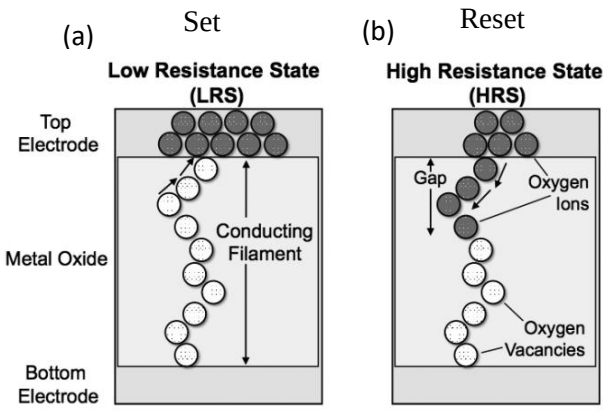

Figure 2.17: Conductive filament-based RRAM. (a) LRS state with the formed conductive filament for the Set process where the motion of the oxygen anions towards the top electrode is indicated. (b) HRS state with the partially broken conductive filament for the Reset process where the directions of the oxygen anions towards the oxide is indicated recombining with the oxygen vacancies (53).The oxygen anions are in black, oxygen vacancies in white and the conductive filament is the combination of all the oxygen vacancies.

A figure of merit that is used for characterising the performance of the RRAM is the memory window that is defined as the ratio between the resistance for the HRS and LRS: R_{HRS}/R_{LRS}.

This chapter focus on the physical background for understanding the concepts that are used thorough the thesis. In the following chapter, the fabrication methods used for making the samples are detailed from the very simple exfoliation method up to the complex heterostructures.

Bibliography

1. kug.A, Heine.T and Kis.A Electronic properties of transition-metal dichalcogenides.MRS Bulletin.2015;40: 577-584.
2. Wallace PR. The Band Theory of Graphite. Physical Review. 1947;71(9):622-34.
3. Novoselov KS, Geim AK, Morozov SV, Jiang D, Zhang Y, Dubonos SV, et al. Electric Field Effect in Atomically Thin Carbon Films. Science. 2004;306(5696):666-9.
4. Geim AK and Novoselov KS. The rise of graphene. Nat Mater. 2007;6(3):183-91.
5. de Andres PL, Verges JA. First-principles calculation of the effect of stress on the chemical activity of graphene. Appl Phys Lett. 2008;93: 171915.
6. Castro Neto AH, Guinea F, Peres NMR, Novoselov KS, Geim AK. The electronic properties of graphene. Reviews of Modern Physics. 2009;81(1):109-62.
7. Malard LM, Pimenta MA, Dresselhaus G, Dresselhaus MS. Raman spectroscopy in graphene. Physics Reports. 2009;473(5):51-87.
8. Wang JG, Ma FC, Sun MT. Graphene, hexagonal boron nitride, and their heterostructures: properties and applications. Rsc Adv. 2017;7(27):16801-22.
9. Geim AK, MacDonald AH. Graphene: Exploring carbon flatland. Phys Today. 2007;60(8):35-41.
10. G G, Grosso G, Parravicini GP. Solid State Physics: Elsevier Science; 2000.
11. Katsnelson MI, Novoselov KS, Geim AK. Chiral tunnelling and the Klein paradox in graphene. Nat Phys. 2006;2(9):620-5.
12. Castro Neto AH, Guinea F, Peres NMR. Drawing conclusions from graphene. Phys World. 2006;19(11):33-7.
13. Michel KH, Costamagna S, Peeters FM. Theory of anharmonic phonons in two-dimensional crystals. Phys Rev B. 2015;91(13).
14. Neil W. Ashcroft, N. David Mermin.Solid state physics. 1976
15. Biro LP, Nemes-Incze P, Lambin P. Graphene: nanoscale processing and recent applications. Nanoscale. 2012;4(6):1824-39.
16. Wang QH, Kalantar-Zadeh K, Kis A, Coleman JN, Strano MS. Electronics and optoelectronics of two-dimensional transition metal dichalcogenides. Nat Nanotechnol. 2012;7(11):699-712.
17. Mak KF, Lee C, Hone J, Shan J, Heinz TF. Atomically Thin MoS_2: A New Direct-Gap Semiconductor. Phys Rev Lett. 2010;105(13):136805.
18. Xiao D, Liu GB, Feng WX, Xu XD, Yao W. Coupled Spin and Valley Physics in Monolayers of MoS_2 and Other Group-VI Dichalcogenides. Phys Rev Lett. 2012;108:196802.
19. Zeng HL, Dai JF, Yao W, Xiao D, Cui XD. Valley polarization in MoS_2 monolayers by optical pumping. Nat Nanotechnol. 2012;7(8):490-3.
20. Sanchez OL, Ovchinnikov D, Misra S, Allain A, Kis A. Valley Polarization by Spin Injection in a Light-Emitting van der Waals Heterojunction. Nano Letters. 2016;16(9):5792-7.
21. Withers F, Del Pozo-Zamudio O, Mishchenko A, Rooney AP, Gholinia A, Watanabe K, et al. Light-emitting diodes by band-structure engineering in van der Waals heterostructures. Nat Mater. 2015;14(3):301-6.
22. Withers F, Del Pozo-Zamudio O, Schwarz S, Dufferwiel S, Walker PM, Godde T, et al. WSe_2 Light-Emitting Tunneling Transistors with Enhanced Brightness at Room Temperature. Nano Letters. 2015;15(12):8223-8.
23. Guo H, Lan C, Zhou Z, Sun P, Wei D, Li C. Transparent, flexible, and stretchable WS_2 based humidity sensors for electronic skin. Nanoscale. 2017;9(19):6246-53.
24. Zhu ZY, Cheng YC, Schwingenschlögl U. Giant spin-orbit-induced spin splitting in two-dimensional transition-metal dichalcogenide semiconductors. Phys Rev B. 2011;84(15):153402.
25. Ribeiro-Soares J, Almeida RM, Barros EB, Araujo PT, Dresselhaus MS, Cancado LG, et al. Group theory analysis of phonons in two-dimensional transition metal dichalcogenides. Phys Rev B. 2014;90;115438.

26. Yazyev OV, Kis A. MoS_2 and semiconductors in the flatland. Mater Today. 2015;18:20-30.
27. Noah F.Q. Yuan BTZ, Wen-Yu He and K. T. Law. Ising Superconductivity in Transition Metal Dichalcogenides. 2016.Department of Physics, Hong Kong University of Science and Technology.
28. Pimenta MA, del Corro E, Carvalho BR, Fantini C, Malard LM. Comparative Study of Raman Spectroscopy in Graphene and MoS_2-type Transition Metal Dichalcogenides. Accounts of Chemical Research. 2015;48:41-7.
29. Li TS. Ideal strength and phonon instability in single-layer MoS_2. Phys Rev B. 2012;85;235407.
30. Silva-Guillén J.A, San-Jose P. and Roldan.R . Electronic Band Structure of Transition Metal Dichalcogenides from Ab Initio and Slater–Koster Tight-Binding Model. ApplSci. 2016;6:284.
31. Kośmider K, Fernández-Rossier J. Electronic properties of the MoS_2-WS_2 heterojunction. Phys Rev B. 2013;87(7):075451.
32. Kioseoglou G, Hanbicki AT, Currie M, Friedman AL, Gunlycke D, Jonker BT. Valley polarization and intervalley scattering in monolayer MoS_2. Appl Phys Lett. 2012;101:221907
33. Xu XD, Yao W, Xiao D, Heinz TF. Spin and pseudospins in layered transition metal dichalcogenides. Nat Phys. 2014;10(5):343-50.
34. Cao T, Wang G, Han WP, Ye HQ, Zhu CR, Shi JR, et al. Valley-selective circular dichroism of monolayer molybdenum disulphide. Nat Commun. 2012;3:887
35. Kormanyos A, Burkard G, Gmitra M, Fabian J, Zolyomi V, Drummond ND, et al. k.p theory for two-dimensional transition metal dichalcogenide semiconductors. 2D Mater. 2015;2(4): 022001
36. Molina-Sanchez A, Sangalli D, Hummer K, Marini A, Wirtz L. Effect of spin-orbit interaction on the optical spectra of single-layer, double-layer, and bulk MoS_2. Phys Rev B. 2013;88(4).
37. Latzke DW, Zhang WT, Suslu A, Chang TR, Lin H, Jeng HT, et al. Electronic structure, spin-orbit coupling, and interlayer interaction in bulk MoS_2 and WS_2. Phys Rev B. 2015;91(23).
38. Zhang X, Qiao XF, Shi W, Wu JB, Jiang DS, Tan PH. Phonon and Raman scattering of two-dimensional transition metal dichalcogenides from monolayer, multilayer to bulk material. Chem Soc Rev. 2015;44(9):2757-85.
39. Kamalakar MV, Dankert A, Kelly PJ, Dash SP. Inversion of Spin Signal and Spin Filtering in Ferromagnet vertical bar Hexagonal Boron Nitride-Graphene van der Waals Heterostructures. Sci Rep-Uk. 2016;6;21168.
40. Ni ZH, Wang HM, Kasim J, Fan HM, Yu T, Wu YH, et al. Graphene Thickness Determination Using Reflection and Contrast Spectroscopy. Nano Letters. 2007;7:2758-63.
41. Radisavljevic B, Radenovic A, Brivio J, Giacometti V, Kis A. Single-layer MoS_2 transistors. Nat Nanotechnol. 2011;6:147-50.
42. Novoselov KS, Geim AK, Morozov SV, Jiang D, Katsnelson MI, Grigorieva IV, et al. Two-dimensional gas of massless Dirac fermions in graphene. Nature. 2005;438:197-200.
43. Yu S, Chen H-Y, Gao B, Kang J, Wong HSP. HfOx-Based Vertical Resistive Switching Random Access Memory Suitable for Bit-Cost-Effective Three-Dimensional Cross-Point Architecture. Acs Nano. 2013;7:2320-5.
44. Fang Z, Wang XP, Sohn J, Weng BB, Zhang ZP, Chen ZX, et al. The Role of Ti Capping Layer in HfOx-Based RRAM Devices. IEEE Electron Device Letters. 2014;35:912-4.
45. Waser R, Aono M. Nanoionics-based resistive switching memories. Nat Mater. 2007;6:833.
46. Webster JG. Wiley encyclopedia of electrical and electronics engineering. John Wiley & Sons, Inc 1999(Ielmini D 2014 Resistive switching memories (John Wiley & Sons, Inc.)).
47. Kwon D-H, Kim KM, Jang JH, Jeon JM, Lee MH, Kim GH, et al. Atomic structure of conducting nanofilaments in TiO_2 resistive switching memory. Nat Nanotechnol. 2010;5:148.

48. Wong HP, Lee H, Yu S, Chen Y, Wu Y, Chen P, et al. Metal–Oxide RRAM. Proceedings of the IEEE. 2012;100:1951-70.
49. Wang S-Y, Lee D-Y, Huang T-Y, Wu J-W, Tseng T-Y. Controllable oxygen vacancies to enhance resistive switching performance in a ZrO_2-based RRAM with embedded Mo layer. Nanotechnology. 2010;21:495201.
50. Ielmini D. Resistive switching memories based on metal oxides: mechanisms, reliability and scaling. Semiconductor Science and Technology. 2016;31:063002.
51. Yu S, Guan X, Wong HP. On the Switching Parameter Variation of Metal Oxide RRAM—Part II: Model Corroboration and Device Design Strategy. IEEE Transactions on Electron Devices. 2012;59:1183-8.
52. Guan X, Yu S, Wong HP. On the Switching Parameter Variation of Metal-Oxide RRAM—Part I: Physical Modeling and Simulation Methodology. IEEE Transactions on Electron Devices. 2012;59:1172-82.
53. Lee MKF, Cui Y, Somu T, Luo T, Zhou J, Tang WT, et al. A System-Level Simulator for RRAM-Based Neuromorphic Computing Chips. ACM Trans Archit Code Optim. 2019;15:1-24.

54. Singh D, Gupta SK, Sonvane Y, Kumar A, Ahuja R. 2D-HfS_2 as an efficient photocatalyst for water splitting. Catalysis Science & Technology. 2016;6 :6605-14.

Chapter 3: Fabrication

3.1 Introduction

This chapter presents a detailed overview of the key fabrication techniques involved in the assembly of stacked sequences of different 2D materials, also known as van der Waals heterostructures. At first the exfoliation technique of atomically thin layers from bulk crystals is introduced, followed by the optical contrast and a description of the bespoke equipment used for assembling the heterostructures. Secondly, the two main techniques for flake transfer and assembling them into stacks are discussed highlighting the individual benefits and limitations. Thirdly, the contamination issues of the transfer techniques are addressed.

3.2 Mechanical exfoliation of 2D materials

Few-layers and monolayers are obtained by thinning down bulk crystals (e.g. graphene, TMDCs...) by micromechanical exfoliation/cleavage technique. This is usually done by sequential pealing of a layered bulk crystal with the use of adhesive tape, i.e. the Scotch tape method (1). Figure 3.1 (a) shows the bulk crystal (black circle) placed on the adhesive tape and thinned through repeated peeling action (grey circles) on the surface of the tape. The tape is subsequently placed on a pre-heated substrate at a temperature of 90 $^{\circ}$C on the hot plate and pressed down onto the substrate (e.g. Si/SiO_2, glass, quartz, plastic, textile fibres, etc.). In this process, flakes consisting of a varying number of layers to include single atomic layers are transferred onto the substrate, see Figure 3.1 (b). Hence, they are subsequently identified by inspection under an optical microscope, since the absorption of the light is directly proportional to the number of layers starting from monolayers (2). The difference in the reflected light by flakes of different thicknesses and the substrates is detectable by the “naked human eye”. Crucially this difference can be quantified and it can be used to automate the detection of flakes where the optical contrast is defined as the difference in the reflected light by flakes to the reflected light from the empty substrate can enable an accurate screening over the number of layers.

Figure 3.1: Micromechanical exfoliation of 2D materials. (a) Tape in blue with the already exfoliated thin material in grey and bulk crystal in black. (b) Transfer of the exfoliated material from the tape on top of the substrate in red.

Indeed, monolayer graphene has an absorbance of $\pi\alpha$=2.293% where $\alpha = e^2/\hbar c$ is the fine-structure constant for the infrared-to-visible spectral range as it does not have a bandgap (3). Therefore, graphene absorbs 2.3% per layer, each of them adding another extra 2.3% for few layers graphene (4).

The optical contrast technique is used to determine flake's thickness with an optical microscope ("naked eye") (5) which is defined by the contrast coefficient (C) (5):

$$C = \frac{R(\lambda)_0 - R(\lambda)}{R(\lambda)_0} ; \quad (3.1)$$

where $R(\lambda)_0$ is the reflected light from the Si/SiO_2 substrate and $R(\lambda)$ is the reflected light from the graphene sheet (5). The optical contrast is between the graphene flake that covers the substrate and bare substrate; for monolayer graphene this is around 5 % under white light illumination for the sequence of Si/SiO_2/graphene/air. This technique is reliable for up to 4 layers of graphene; thus, another technique is used to complement it; Raman spectroscopy that is explained in Chapter 4.

3.3 Fabrication of Van der Waals heterostructures

3.3.1 Introduction

Assembling different 2D materials (see figure 3.2) within the same van der Waals heterostructure creates new device structures that enable the study of novel fundamental physics as well as supporting the development of unprecedented applications (6).

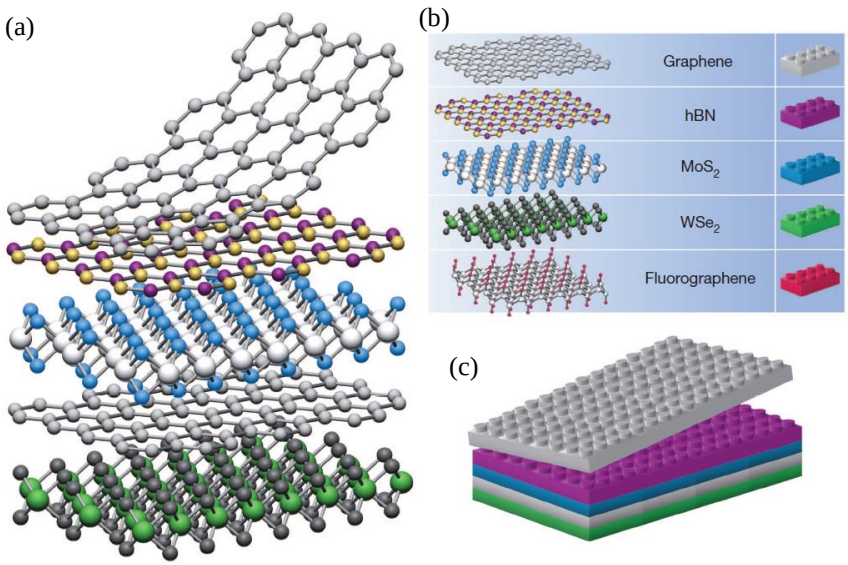

Figure 3.2*:* Van der Waals heterostructures of 2D materials. (a) Assembling of different 2D materials with their atomic lattice structure. (b) 2D materials with their respective lattice on the left and with a "Lego" piece on the right. (c) "Lego" assembling of the heterostructure of (a). Reproduced with permission (7).

Stacking atomically thin layers to form heterostructures with clean interfaces is a technically challenging task which requires the use of bespoke equipment such as the system shown in figure 3.3 (a). This system allows to control the relative

alignment between the crystallographic orientation of the top flake (see figure 3.3 (b) in orange colour) and target flake attached to the target substrate (see figure 3.3 (b) in purple colour) through the use of two translation stages. For the top flake resting on the transfer arm (see figure 3.3 (b) in red colour), the micromanipulator (X1, Y1, Z) is used for the directions and pitch and yaw for the rotations. The orientation and position of the target flake is controlled by the stage the micromanipulator (X2, Y2) used for the XY plane and rotation in the same plane, see figure 3.3 (b)). The stage (see green colour in figure 3.3 (b)) is connected to a vacuum pump that holds the target substrate, while a heating element enables the local control of the temperature which can be used to fine tune the transfer conditions and improve the adhesion between the top and bottom flakes.

This equipment has an optical microscope provided by long-working distance objectives with three different magnifications (x 5, x 10 and x 20) and a white light source. Colour filters are used to enhance the contrast of the flakes and facilitate their identification. A charge-coupled device (CCD) camera is fitted on top of the microscope for acquiring pictures while assembling. A Nikon elements Microscope Imaging software (NIS) enables the user to draw in real time the contour of the flakes on the computer screen, add colour filters for distinguishing the flakes and improving the optical contrast.

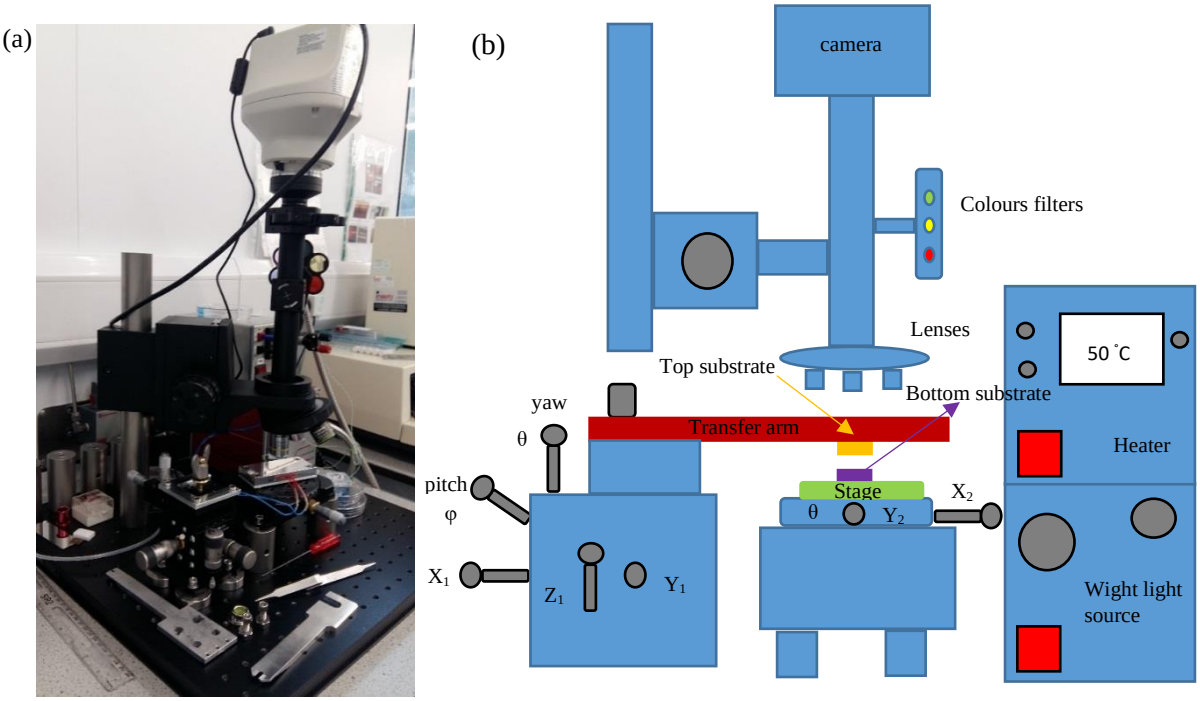

Figure 3.3: Transfer setup. (a) Image of the transfer setup. (b) Schematic of the transfer setup of the right: the micromanipulators, yaw and pitch are in grey, the transfer arm in red, the stage in green colour, top substrate in orange, bottom substrate in purple and the rest solid parts are in blue.

In this thesis mainly two *dry-transfer methods* have been used for the assembly of van der Waals heterostructures. These are the PDMS stamp transfer technique and the bilayer polymer transfer technique. In both cases the target substrate is

treated by an oxygen plasma prior to the exfoliation and a cleaning process with isopropanol (IPA) and acetone chemicals. The oxygen plasma treatment removes ambient adsorbates from the surface of the target substrate improving the adhesion between the exfoliated crystal from the tape and the target substrate (8). Therefore, the number and area of the individual flakes increases using this treatment. It is also possible to functionalise the substrate to increase the interaction between the substrate and the flakes, although this is known to introduce generally unwanted charge doping (9).

3.3.2 PDMS stamp transfer technique

This method is an all-dry transfer method that uses a viscoelastic material-PDMS (polydimethylsiloxane) bought from TELTEC (1, 10) that is sandwiched between two layers: Polyethylene coversheet and clear Polyester substrate. PDMS is made of a network of cross-linked dimethylsiloxane oligomers. However, up to 5% of the oligomers can remain uncrosslinked after the curing process depending of the curing time and temperature used. These oligomers can remain on the stamp used in the transfer process as well as contaminating the layer on the vdW heterostructures after the PDMS stamp (6).

The mechanical behaviour of PDMS is explained with the viscoelasticity (1). The adhesion between the donor substrate (normally the exfoliated tape) and PDMS and the adhesion between the acceptor substrate (silicon or quartz) and PDMS depends on the separation speed (11). Therefore, for the first process, the PDMS is pulled away from the tape at high peel velocity (typical values of ~10 cm s-1 have been reported by M.A.Meitl et al. (11)) in which the tape is lifted away from the tape and flakes show stronger adhesion towards PDMS so the flakes are transferred on it. Afterwards, PDMS is brought into contact with the acceptor/target substrate at low speed with the transfer setup. When the PDMS is peeling off from the receiving substrate, the peel velocity is slow (values of ~1 mm s-1 has been reported by M.A.Meitl et al. (11)) releasing the flake from the PDMS and adhering to the target substrate (1).

First of all, the first desired material is exfoliated on a pre-cleaned target substrate and the sample is inspected under the optical microscope until the desired flake with appropriate thickness and size is found, see figure 3.4 (a) for the case of tungsten diselenide and hafnium disulphide on quartz. The distance between the horizontal (vertical) crosshairs is 100 (50) μm. The target substrate is placed on the stage (see figure 3.3 (b) in green colour) whereas the second desired material is exfoliated on the tape and transferred on PDMS (10) and a suitable flake is identified by optical inspection of the PDMS with a visible wavelength microscope. Afterwards, the PDMS piece is cut in a smaller piece and secured to the transfer arm by a double-sided tape (see figure 3.3 (b) in red colour). Then, both flakes are identified using the x 10 magnification objective. Hence, the stage temperature is set at 50 ºC - 60 ºC. The NIS software settings are used for drawing the top and target flakes thus helping to choose the correct alignment between them according to the desired design of the heterostructure. The arm is brought down using the micromanipulators and keeping the top flake in focus using the drawing as a guideline for the relative alignment. Once the top flake is

brought into contact to the bottom flake, the contrast of the target substrate changes (as shown in figure 3.4 (b) with x 5 magnification objective) as the PDMS starts to cover the target substrate. After the target substrate is covered by the PDMS, the transfer arm is brought back up peeling off slowly from the bottom substrate leaving the top flake of the chosen position. Figure 3.4 (c) shows the optical image (with green filter) of the heterostructure after the procedure.

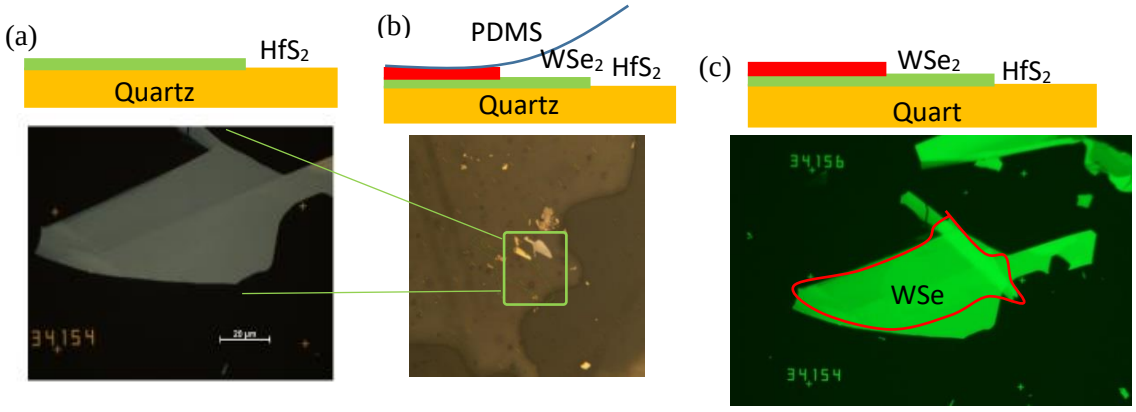

Figure 3.4: Schedule and optical images of 1L-WSe2/few-layer HfS2 stack on quartz substrate by PDMS stamp transfer technique. (a) Exfoliated HfS2 flake in green on quartz substrate in orange. The scale bar is 20 μm. (b) Transfer of monolayer WSe2 in red on HfS2 where the line indicates the contrast of the PMDS in blue covered area and the one not covered. (c) The stack completed with green light.

3.3.3 Bilayer polymer transfer technique

In this method, a substrate such as Si/SiO2 is coated with polymethyl methacrylate (PMMA) and Poly vinyl alcohol (PVA) water-soluble polymer (1), where the PMMA is a sacrificial layer. Flakes are obtained by mechanical exfoliation directly on the bilayer polymer assembly (PMMA/PVA ≈400/400 nm, figure 3.5 (a)) whilst the temperature of the substrate is maintained at 135 ºC as shown in figure 3.5 (b). After the identification of the desired flake a circle is scored around the flake as shown in figure 3.5 (c) with the use of tweezers, leaving the flake in the middle of it. This process is conducted under the microscope with x 5 magnification objective. As PVA is soluble in deionized water (DI), we used the tweezers for dropping DI water in the circle dissolving the PVA and detaching the PMMA membrane as silicon and PMMA are hydrophobic (10). The silicon substrate with the PMMA/PVA stack is immersed in a beaker filled by DI water (figure 3.5 (d)) releasing the PMMA membrane as PVA dissolves. Afterwards, the membrane is scooped from the water using a washer that is held by tweezers (figure 3.5 (d)). Previously PMMA was placed on the edges of the washer and baked at 90 ºC on a hot plate for 10 minutes so that the adhesion between the PMMA membrane and washer improves. Subsequently, the washer is placed on the transfer arm and facing the target substrate (figure 3.5 (e)). The membrane is brought into contact (figure 3.5 (f)) using the same technique that is described in section 3.3.2 at 70 ºC and using both micromanipulators for the alignment. This membrane is used for either drop-down/peeling (9) (figure 3.5 (g) the top flake is left on the target substrate) or picking/lifting up (figure 3.5(h)) the

flakes from the target substrate. In the peeling process, the PMMA membrane releases the top flake onto the target flake and the stack gets on the target substrate. On the other hand, in the lifting up process the strong adhesion between PMMA membrane and the layered materials enables the 2D materials to be mechanically detached from the target substrate and with the whole stack on the membrane, allowing for subsequent transfer to another target substrate. Sometimes, in the peeling process the membrane can get stuck down on the substrate which means that not only the flake is on the target substrate. For improving the adhesion between the membrane and the target substrate, the substrate is baked at 150 ºC for 10 minutes, subsequently, the PMMA membrane is dissolved in acetone.

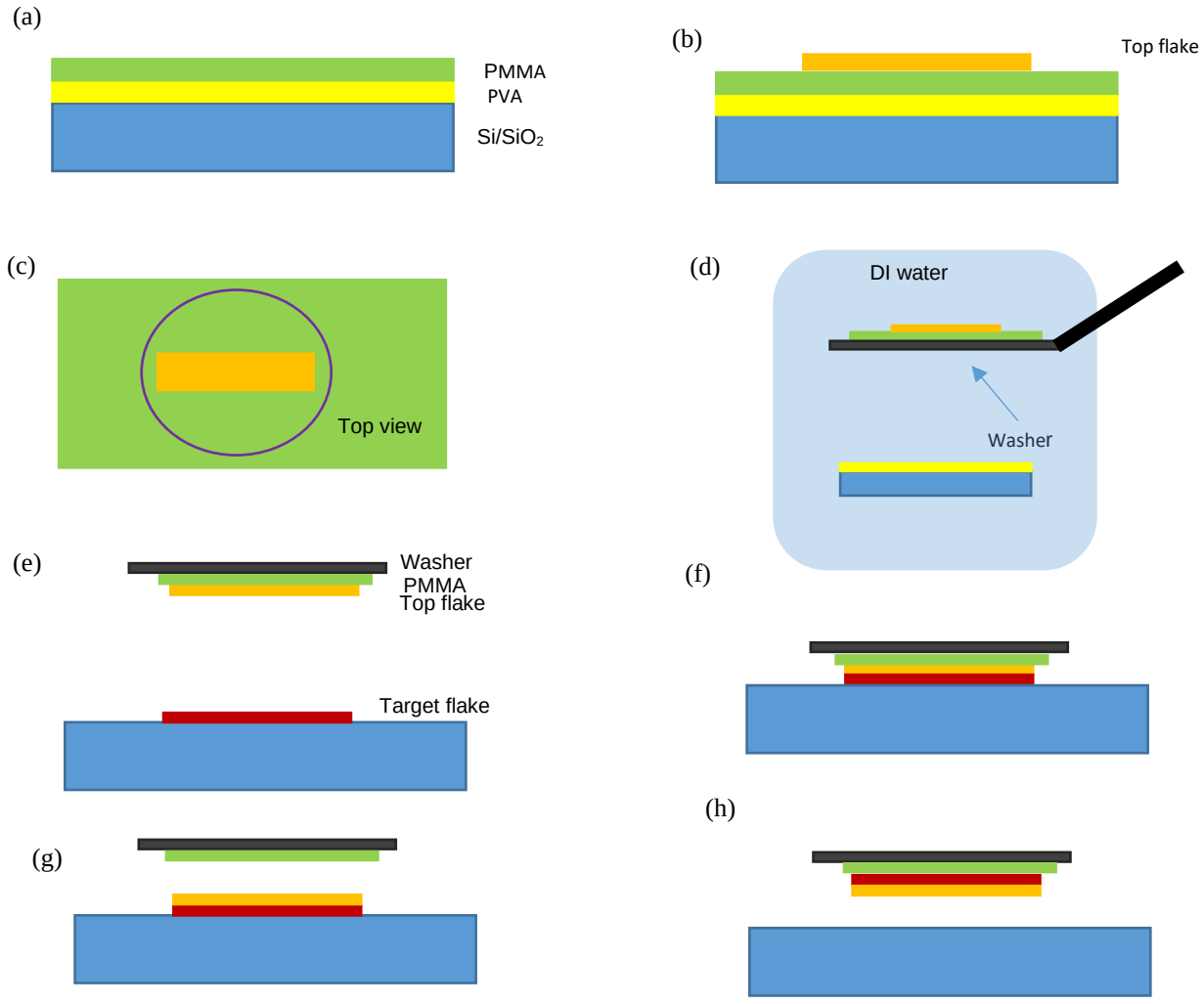

Figure 3.5: PMMA/PVA transfer technique schedule. (a) PMMA (green) /PVA (yellow) coated on silicon wafer (blue). (b) Exfoliation of the top flake (orange) on the coated silicon wafer. (c) Circe (purple) around the flake on the PMMA/PVA. (d) Immersion of the exfoliated substrate in a beaker filled up by DI water and scooped up the PMMA membrane with the washer (black). (e) Alignment of the top flake (orange) with the target flake (red). (f) Contact of the top and target flakes. (g) Peeling process of the membrane leaving the top flake on the substrate. (h) Picking up process of the membrane with the whole stack.

3.4 Contamination of the transfer techniques

The techniques explained in section 3.3.2 and 3.3.3 often result in vdW heterostructures with sizeable contamination between the layers that are stacked, this is manifested as “bubbles” peppering the surface of the sample. These bubbles are likely to be water adsorbates and/or trapped air, residues when the flakes are detached from the tape on the pre-heated substrate in the exfoliation or ambient airborne hydrocarbon contamination (12) as the assembling process is done in ambient atmosphere (9), not in the glove box. These bubbles collect the contamination and leave the sample free of it (1).

These bubbles have been reported in previous work by A.Castellanos-Gomez et al. (1) in which they clarified that the 30-40 % of their heterostructures have free bubbles areas and they claimed that if the PDMS undergoes a high pressure while being transferred on the target substrate, the elastomer may be deformed or break giving rise to bubbles (1). F.Pizzocchero et al. reported these “blisters” in graphene and h-BN vdW heterostructures using two polymers for the stamp: PDMS and polypropylene carbonate (PPC) (9).

These bubbles have been seen in vdW heterostructures from this work using PDMS stamp transfer technique as shown in the optical picture of figure 3.6. The bottom layer is few-layers graphene on quartz as a substrate, the top layer is h-BN and the bubbles are indicated by a red circle. The distance between the horizontal (vertical) crosshairs is 100 (50) µm.

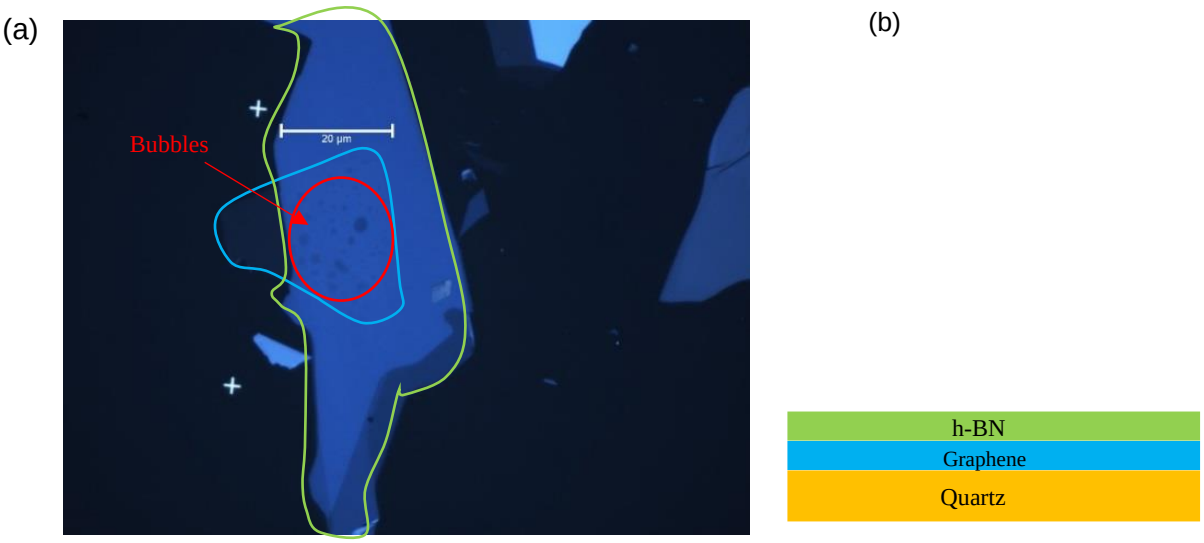

Figure 3.6: VdW heterostructure with PDMS technique. (a) Optical image of the stack: h-BN in green for the top layer, graphene in blue for the bottom layer, quartz as a substrate and bubbles in red. The scale bar is 20 µm. (b) The schematic of the stack of the right following the same colour sequence.

The bilayer polymer transfer technique can lead to some trapped adsorbates between the layers as well as it was reported by A.S.Mayorov et at. (13) in devices made by graphene sandwiched between two h-BN in the assemble

process and S.J.Haigh et al. (14) by devices made by monolayer and bilayer graphene sandwiched between thin h-BN layer individually.

These bubbles have been seen while using the bilayer polymer transfer technique as well as shown in figure 3.7. This picture shows h-BN as a bottom layer and monolayer graphene as top layer on Si/SiO_2 substrate with red filter. The bubbles can be seen on the monolayer graphene trapped between graphene and h-BN.

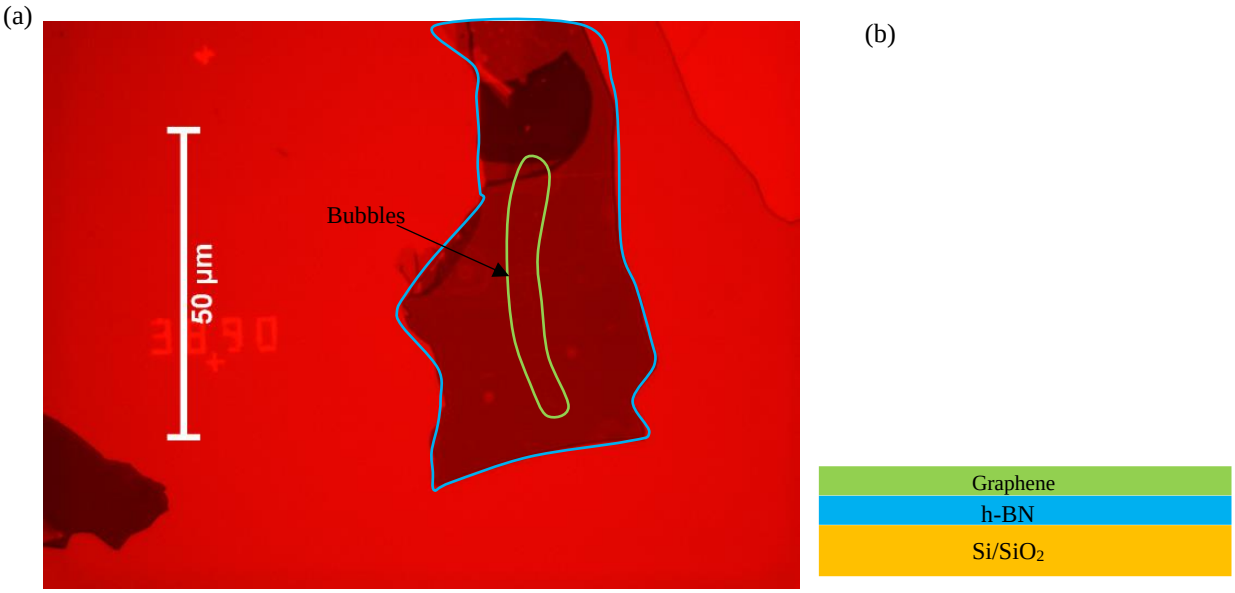

Figure 3.7: VdW heterostructure with bilayer polymer transfer technique. (a) Optical image of the stack: h-BN in blue for the bottom layer, graphene in green for the top layer, Si/SiO_2 as a substrate and bubbles between graphene and h-BN. The picture was taken with red filter. The scale bar is 50 µm. (b) The schematic of the stack of the right following the same colour sequence.

Bilayer polymer transfer technique is the only one that can have exfoliated monolayer graphene due to the compatibility of graphene with PMMA. Therefore, if monolayer graphene electrodes are needed this technique is used, however, this technique depends on the contrast of the polymers and the filters to identify a layer. Moreover, the membrane is easy to break. PDMS stamp transfer technique can be mastered quicker and it is less time consuming, nevertheless both techniques leave residues.

The contamination can be reduced if the stacks are done in the glove box rather than in air, however, the use of the glove box may difficult the degree of freedom while stacking.

This chapter shows two different techniques for fabricating the heterostructures and their advantages and disadvantages as well as the handmade set up used. The characterisation of the heterostructures is explained in Chapter 4 where the background is provided, and the Raman and photoluminescence set up is described.

Bibliography

1. Castellanos-Gomez A, Buscema M, Molenaar R, Singh V, Janssen L, van der Zant HSJ, et al. Deterministic transfer of two-dimensional materials by all-dry viscoelastic stamping. 2D Mater. 2014;1:011002.
2. Novoselov KS, Jiang D, Schedin F, Booth TJ, Khotkevich VV, Morozov SV, et al. Two-dimensional atomic crystals. P Natl Acad Sci USA. 2005;102:10451-3.
3. Mak KF, Sfeir MY, Wu Y, Lui CH, Misewich JA, Heinz TF. Measurement of the Optical Conductivity of Graphene. Phys Rev Lett. 2008;101:196405.
4. Nair RR, Blake P, Grigorenko AN, Novoselov KS, Booth TJ, Stauber T, et al. Fine Structure Constant Defines Visual Transparency of Graphene. Science. 2008;320:1308.
5. Ni ZH, Wang HM, Kasim J, Fan HM, Yu T, Wu YH, et al. Graphene Thickness Determination Using Reflection and Contrast Spectroscopy. Nano Letters. 2007;7:2758-63.
6. Jain A, Bharadwaj P, Heeg S, Parzefall M, Taniguchi T, Watanabe K, et al. Minimizing residues and strain in 2D materials transferred from PDMS. Nanotechnology. 2018;29:265203.
7. Grigorieva A.K. and Griegorieva.I.V. Van der Waals heterostructures.Nature. 2013;499:419
8. Huang Y, Sutter E, Shi NN, Zheng J, Yang T, Englund D, et al. Reliable Exfoliation of Large-Area High-Quality Flakes of Graphene and Other Two-Dimensional Materials. Acs Nano. 2015;9:10612-20.
9. Pizzocchero F, Gammelgaard L, Jessen BS, Caridad JM, Wang L, Hone J, et al. The hot pick-up technique for batch assembly of van der Waals heterostructures. Nat Commun. 2016;7:11894.
10. Frisenda R, Navarro-Moratalla E, Gant P, Pérez De Lara D, Jarillo-Herrero P, Gorbachev RV, et al. Recent progress in the assembly of nanodevices and van der Waals heterostructures by deterministic placement of 2D materials. Chem Soc Rev. 2018;47:53-68.
11. Meitl MA, Zhu Z-T, Kumar V, Lee KJ, Feng X, Huang YY, et al. Transfer printing by kinetic control of adhesion to an elastomeric stamp. Nat Mater. 2006;5:33-8.
12. Li Z, Wang Y, Kozbial A, Shenoy G, Zhou F, McGinley R, et al. Effect of airborne contaminants on the wettability of supported graphene and graphite. Nat Mater. 2013;12:925.
13. Mayorov AS, Gorbachev RV, Morozov SV, Britnell L, Jalil R, Ponomarenko LA, et al. Micrometer-Scale Ballistic Transport in Encapsulated Graphene at Room Temperature. Nano Letters. 2011;11:2396-9.
14. Haigh SJ, Gholinia A, Jalil R, Romani S, Britnell L, Elias DC, et al. Cross-sectional imaging of individual layers and buried interfaces of graphene-based heterostructures and superlattices. Nat Mater. 2012;11:764-7.

Chapter 4: Characterisation

4.1 Introduction

There are two main types of scattering of photons by matter, these are Rayleigh and Raman. The Rayleigh scattering is an elastic scattering process, whereby the scattered photons has the same frequency as the incoming photon. At a microscopic level, the absorbed photon by a material creates an excited electron and hole which will emit a photon of the same frequency as that of the absorbed photon upon recombining in a radiative process: $h\nu_{in} = h\nu_{out}$, where ν_{in} is the incoming photon frequency and ν_{out} is the outgoing photon frequency (1). An inelastic Raman scattering process can also take place (2) as it was first observed in 1928 by Sir Chandrasekhra Venkata Raman (3). In this case, the frequency of the scattered photon differs from that of the incoming photon due to a loss of energy in crystal vibrations, which are phonons. Hence, a spectral analysis of the scattered photons provides direct information on the phonons. In Raman, the electron is excited from the occupied state in the valence band due to the absorption of a photon to an unoccupied state which could be a virtual state within the bandgap or real state above the conduction band.

Raman is a non-destructive inelastic light scattering technique which probes the lattice vibrational modes (phonons) in a solid. This information can be used to identify substances from their characteristic spectral patterns (2, 4, 5). The scattered light provides, in the case of the graphene, information about the number of layers (2), charge doping (2), disorder (6), defects (6) and strain (6).

Conventionally in Raman spectra, the scattered light intensity is plotted versus the Raman shift for the wavenumbers (1/wavelength) (i.e $1/\lambda_{in}$ - λ_{out}), where λ_{in} is the incoming photon wavenumber and λ_{out} is the scattered photon wavenumber. This shift can be expressed in units of reciprocal centimetres (cm-1):

$$\Delta\omega\ [\text{cm-1}] = \left(\frac{1}{\lambda_{in[\text{nm}]}} - \frac{1}{\lambda_{out[\text{nm}]}}\right)\frac{10^7[\text{nm}]}{cm} \quad (4.1)$$

Phonon Raman scattering can occur in two different ways.

1-Stokes: The scattered photon has a smaller frequency than the incoming photon which loses some of its energy to create a phonon (1):

$$\hbar\omega_{in} - \hbar\omega_{out} = \hbar\Omega, \quad (4.2)$$

where ω_{in} is the incoming photon frequency, ω_{out} is the scattered photon frequency and Ω is the phonon frequency.

2-Anti-Stokes: The incoming photon has smaller energy than the scattered photon which means that a phonon in the sample is enlisted to enable the Raman process (1):

$$\hbar\omega_{out} = \hbar\omega_{in} + \hbar\Omega\ , \quad (4.3)$$

In first-order Raman process, there is only one phonon involved (7) whereas for the second-order Raman process two phonons are involved which they must have equal magnitude of the momenta but travelling in opposite directions to keep the momentum (8). For resonant Raman the transition is between real states having the possibility of single resonant (SR), double resonant (DR) and tripe resonant (TR) (1). In graphene all the transitions are resonant as it is energy gapless and it has a linear energy dispersion where the electrons are brought into real states (9). In graphene, for transitions within the same Dirac cone are named intra-valley whereas for transitions happening between K and K' are named inter-valley.

4.2 Raman of graphene and graphite

There are three main peaks in the Raman spectra of graphene and graphite: G, G' (also known as 2D) and D and they are all due to in-plane atomic vibrations (1). In graphite, the energy positions of these Raman peaks have the following Raman shifts:, G – 1580 cm^{-1} and G' (2D) – 2700 cm^{-1} and in case of samples with defects and disorder D –1350 cm^{-1} for the laser excitation at 2.41 eV (8). The G' peak was named historically like that as it is the second most prominent peak for graphitic samples, however, this band is the second order of the D peak-so-called 2D (9). The processes that give rise to these 3 main Raman spectral peaks with the transitions explained in figure 4.1.

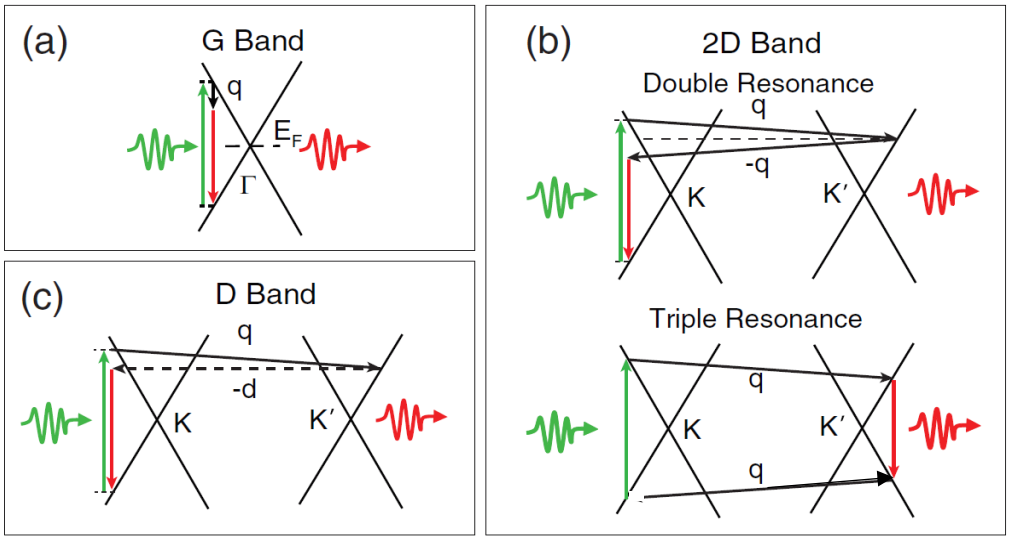

Figure 4.1: Electron-phonon scattering mechanism of monolayer graphene for the main three graphene Raman bands (G, D and G' (2D)) within Dirac cones. (a) Intra-valley, first-order single-resonant Raman scattering for the G peak at the Γ point of the first Brillouin zone of the phonon dispersion involving one phonon for K Dirac cone. (b) Inter-valley and second-order Raman scattering for the G' (2D) peak involving two phonons for the double and triple resonance Raman. (c) Inter-valley and second-order Raman scattering for the D peak involving one phonon and one defect. G' and D peaks happen in the vicinity of the K point of the first Brillouin zone and the transitions are between K and K' Dirac cones. Incoming (scattered) photon in green (red) lines, q for the momentum of the phonon with a black line, d for the momentum of the defect with a dotted line and the Fermi level is indicated by a dashed line in the charge neutrality point (7).

The Raman G peak is a first-order single-resonant Raman scattering process that happens within the same K Dirac cone (intra-valley) (8). This peak is related to the vibrations of the in-plane sp^2 hybridised carbon atoms C-C stretching mode (2, 10) and it is doubly-degenerate with the TO and LO phonons at the center of the first Brillouin zone Γ (6, 7, 11). An incoming photon promotes an electron from the valence band into the conduction band followed by the scattering of the electron by either TO or LO phonon. The electron and hole recombine radiatively emitting a scattered photon that is red shifted by the amount of energy given to the phonon as shown in figure 4.1 (a) (2, 7, 12).

The Raman G' (2D) is a second-order, double-resonant or tripe-resonant Raman scattering within the K and K' Dirac cones (inter-valley) (8). This peak is related to the breathing-like mode of the sp^2 carbon rings (7) and the scattering process happens at the vicinity of the K point in the first Brillouin zone for the TO phonon modes (7). For the double-resonant process an incoming photon promotes an electron from the valence band into the conduction band within Dirac cone at the K point followed by the scattering by a TO phonon to the Dirac cone at K' (7). This electron is back-scattered to the Dirac cone at K by a second TO phonon as the energy and momentum must be conserved (7, 13) so that there are two phonons with opposite momenta (8, 11, 14). Afterwards, the electron and hole recombine radiatively at the K Dirac cone emitting a scattered photon as shown in figure 4.1 (b) (7). For the case of triple resonance, the scattering is considered with holes; instead of having an electron being back scattered into K Dirac cone by a phonon with - q momentum for double resonance, the hole is scattered by a +q momentum from the K to K'(8) as shown in figure 4.2 (b). Therefore the recombination process happens near K' (8).

The Raman D peak is related to the disorder or defect of graphene and it is a second-order double resonant Raman scattering process (8) between K and K' Dirac cones (inter-valley). This peak is related to the breathing-like mode of the sp^2 carbon like G' (8, 9) being G' (2D) an overtone of D (1).This peak is generated by one TO photon near K point of the first Brillouin zone and one defect is needed for the activation (6, 8). The scattering process is the same one explained for G' where the electron is back-scattered by a defect instead for momentum conservation as shown in figure 4.1 (c) (7). The frequency of the G' (2D) is the double of the frequency of the D peak as G' has two phonons involved in the scattering process (8).

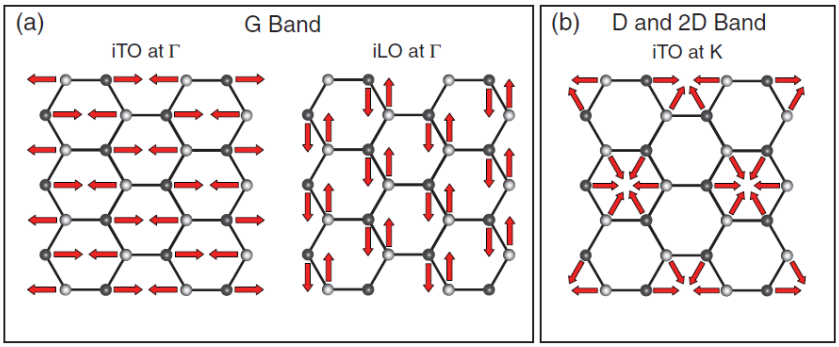

Figure 4.2: Phonon vibrations contributing to main G, G' (2D) and D bands for Raman of monolayer graphene. (a) Vibration of the two atomic sub-lattices for TO and LO phonons at Γ of the first Brillouin zone for the G band. (b) Breathing modes of the sp^2 carbon atom rings for TO phonon at K of the first Brillouin zone for D and G' (2D) bands. Black and grey for the two sub-lattices and the arrows for movement of the atoms (7).

For the G band the phonon involved are TO and LO at the Γ of the first Brillouin zone where the two sub-lattices vibrate opposite to each other as shown with the red arrows whereas for the D and G' (2D) bands the atoms are moving towards the center of the atom ring as shown in figure 4.2. These three bands appear in graphene spectrum, however, depending of the number of layers the spectrum looks differently. Monolayer graphene's G band intensity is much lower than few layers graphene as its intensity increases almost linearly as the number of layers increases as more carbon atoms are detected from multi-layer graphene (2, 14, 15) as shown in figure 4.3 (a) for graphite. In this figure there is no D peak for monolayer graphene and graphite which means that the samples were defect-free (13).

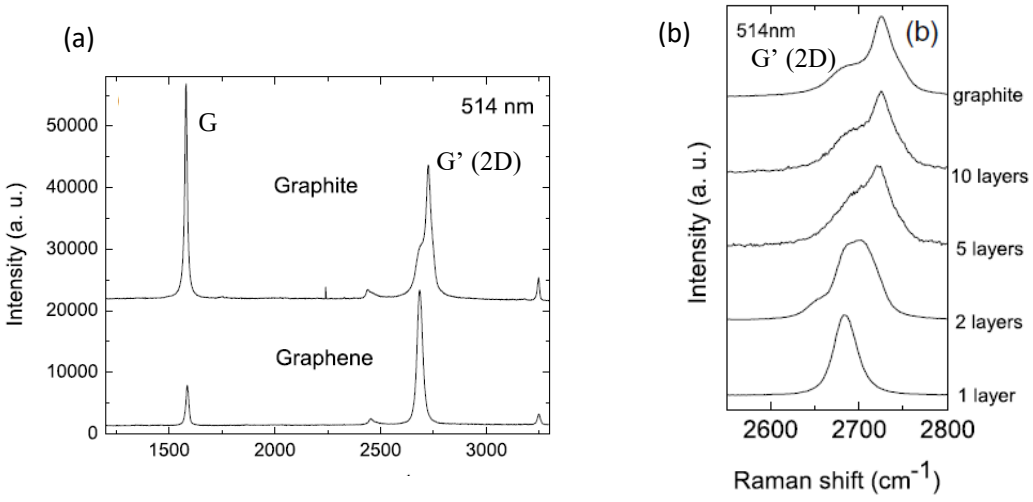

Figure 4.3: Raman spectra for graphene. (a) Monolayer graphene and graphite Raman spectra with G ~ 1580 cm^{-1} and G' (2D) ~ 2700 cm^{-1} peaks for the excitation laser of 514 nm (13). (b) Evolution of G' (2D) peak around 2700 cm^{-1} increasing the number of layers for the excitation laser of 514 nm. Reproduced with permission (13).

Figure 4.3 (a) and (b) show that the G' (2D) peak shape changes with the number of layers; for monolayer the G' (2D) peak is sharp and symmetric. A single

Lorentzian function provides an excellent fit to G' in the case of monolayer graphene. In the case of bilayer graphene, the G' peak is fitted to four Lorentzians as there are four possible transitions in the scattering process as shown in figure 4.4 (a) (8, 12). Bilayer graphene has two conduction and valence bands which underpin for Raman resonant processes originating the G' peak, see figure 4.4 (a) (9). Considering that the light couples only two sub-bands pairs of the four of them for the G' (2D) according to the DFT calculations that leaves to only four processes denoted by the momenta q_{1B}, q_{1A}, q_{2A} and q_{2B} for the phonon coupling to the bands (9, 13). These Lorentzians fittings for G' are shown in green for the figure 4.4 (b) labelled by $2D_{1B}$, $2D_{1A}$, $2D_{2A}$ and $2D_{2B}$ (9). The typical excitation wavelength lights for graphene are 532 nm and 514 nm.

Upon increasing the number of layers, the electronic band structure changes approaching the one of graphite (16), leading to a broadening and shifting of the G' peak compared to the case of monolayer graphene as shown in figure 4.4 (b). Thus the G' peak is a widely considered to be a fingerprint for identifying the number of layers up to less than five layers as from five layers is almost impossible to distinguish from graphite (9) as shown in figure 4.3 (b). This identification is noticeable especially between monolayer and bilayer, as Y.Y. Wang et al. reported (2) whereas the G' peak fitting for monolayer graphene was reported by R. Beams et al. (7) by a single Lorentzian lineshape with a full width at a half maximum (FWHM) of ~ 30 cm^{-1} reported by D.Yoom et al. (16).

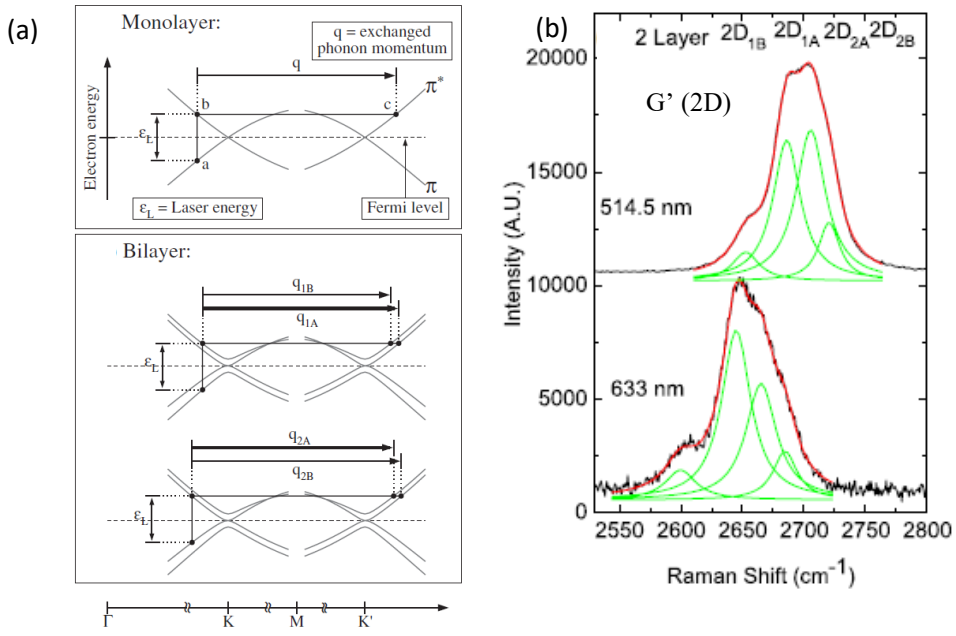

Figure 4.4: Band structure and G' (2D) peak. (a) Monolayer and bilayer graphene band structure and the G' (2D) peak scattering process reproduced with permission (13). (b) G' (2D) peak fitting to four components shown in green for 514.5 nm and 633 nm excitation laser. Reproduced with permission (13).

4.3 Raman of TMDCs

Raman spectra of TMDCs mainly show two peaks for two vibrations modes that are first order (11, 17): the in-plane (E') being degenerate at Γ of the Brillouin zone by the optical branches LO2 and TO2 and the out-of-plane (A_1') with the ZO2 optical branch at Γ (18) explained in Chapter 2. The peaks notation depends on the number of layers: for odd number of layers -E' and A_1'- labels are used whereas for even number of layers-A_{1g} and E_{2g}^1 (19, 20). These phonons are shown in figure 4.5 for the unit cell of monolayer TMDCs: in the A_1' mode: both chalcogen (X) atoms vibrate out-of-plane direction opposite to each other whereas the metal (M) atom is static (11). However, for the E' mode the two chalcogen atoms move in-plane both in phase but opposite to the metal (M) atom (11).

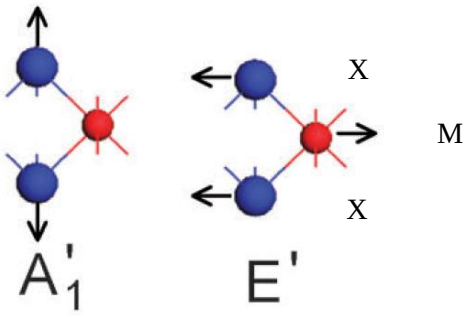

Figure 4.5: Phonon vibrations for monolayer TMDCs. out-of-plane A_1' and in-plane E' phonon modes. Chalcogen (X) in blue and metal (M) in red and black arrows for the movement pf the atoms. [Chem Soc Rev. 2015; 44(9):2757-85] – Reproduced by permission of The Royal Society of Chemistry (18).

Taking MoS_2 as a prototype material for the TMDCs, the Raman spectra is shown in figure 4.6. When the thickness is increased both peaks are widen apart from each other ; A_{1g} softens and E_{2g}^1 stiffens as the number of layers increases from monolayer up to bulk as they dielectric screening increases and due to the stacking changes in intralayer and interlayer coupling as it was reported by H.Zeng et al. (21).This observation was reported by C.Lee et al. in their Raman spectra where it was claimed that the shift of E_{2g}^1 to low frequencies may be attributed to long-rage Coulomb interlayer interactions (22) as well as A. Molina-Sanchez et al. (23) reported. Monolayer MoS_2 has a fixed value between the modes of 19 cm^{-1} that is used for identifying as bulk MoS_2 shows a difference of 26 cm^{-1} (21, 22).

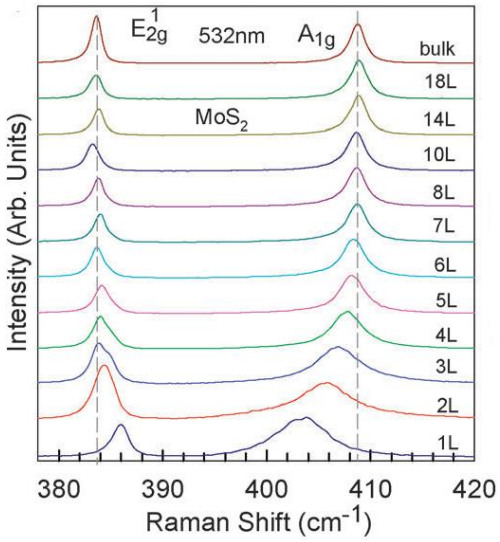

Figure 4.6: Raman spectra of MoS_2 from monolayer up to bulk. A_{1g} and E^1_{2g} are denoted and the number of layers are depicted in different colours for the excitation laser of 532 nm. [Chem Soc Rev. 2015; 44(9):2757-85] – Reproduced by permission of The Royal Society of Chemistry (18).

4.4 Luminescence

Luminescence is used for describing a collective term for different mechanisms where a material emits light radiatively (releasing energy either wholly or partially) (24). These phenomena are distinguished by the method of excitation: photoluminescence (PL, photons absorption), cathodoluminescence (bombardment with a beam of electrons), electroluminescence (EL, applied electric field) (24). In this thesis, the main method of excitation used to investigate light emitted from 2D materials is photon absorption, hence we will focus largely on photoluminescence.

In all the luminescence processes, the electronic transition between the final (E_2, $E_2 > E_1$) and initial (E_1) states results in an emitted wavelength λ (24):

$$\frac{hc}{\lambda} = E_2 - E_1, \qquad (4.4)$$

where h is the Planck constant and c the speed of light.

When the luminescence lasts for a period of time equal to the lifetime of the transition between the two states is named fluorescence whereas for luminescence lasting longer the process is named phosphorescence (24).

4.5 Photoluminescence of TMDCs

Semiconductors have an energy bandgap between valence and conduction bands that must be overcome or equal with by the excitation laser for promoting an electron from the valence band into the conduction band. In this process the material absorbs a photon (24) and a hole (positively charged quasi-particle) is

created in the valence band when the electrons is excited. Due to Coulomb interaction this electron and hole are bound, forming a quasiparticle known as exciton characterized by energy states located just below the conduction band edge.

The single particle energy bandgap fundamental bandgap (E_g in figure 4.7) is the gap between the highest valence band state and the lowest conduction band state. Reflectance, absorption and transmittance spectra often show structures appearing at energies smaller than single particle energy gap which means that the excitons are bound by the binding (E_b in figure 4.7) energy below the conduction band. Figure 4.7 shows a schematic for the possible optical transitions occurring at the K-point of a direct gap 2D semiconductor with spin-orbit split bands. The energy split in the valence band gives rise to two excitons. These are known as A and B, with A (B) being the transition from the highest (lowest) valence band to the conduction band for the K and K' points of the Brillouin zone (25) as shown in figure 4.7. The transitions which conserve the spin orientation are permitted, these are called bright transitions (A and B in figure 4.7 as it was shown in figure 2.10 (b) of chapter 2). The forbidden transitions such as that from the lowest valence band (spin up) up to the highest conduction band (spin down) are called dark transitions (figure 2.10 of chapter 2).

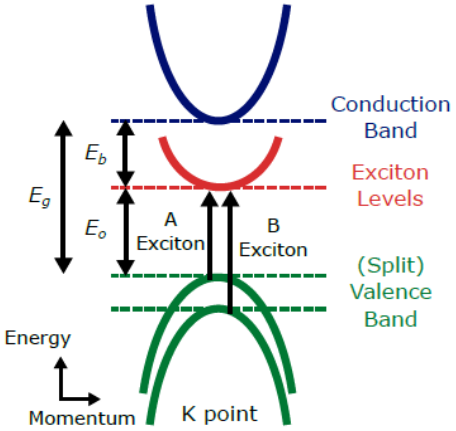

Figure 4.7: Exciton transitions within the energy band for monolayer TMDCs. (a) The K valley with the A and B exciton levels, single particle bandgap (E_g), optical bandgap (E_o) , exciton binding energy (E_b), conduction (valence) band in green (blue) and the exciton levels in red. Reproduced with permission (26).

Figure 4.8 shows the photoluminescence of MoS_2 for different number of layers as a prototype. Both exciton peaks (A and B) appear for all the number of layers, however, the intensity decreases (27) and the peaks are redshifted as the number of layer increases (28) and the system undergoes a transition from direct-to-indirect energy bandgap. There is another extra peak labelled as I which is related to the indirect transition from the highest valence band in Γ point to the half way between the Γ and K of the lowest conduction band (chapter 2) (28, 29). This peak shifts to low energies and its intensity decreases when the number of layers

increases approaching the bulk crystal (28). Raman peaks of MoS_2 and silicon Raman peak appear at low wavelengths of figure 4.8.

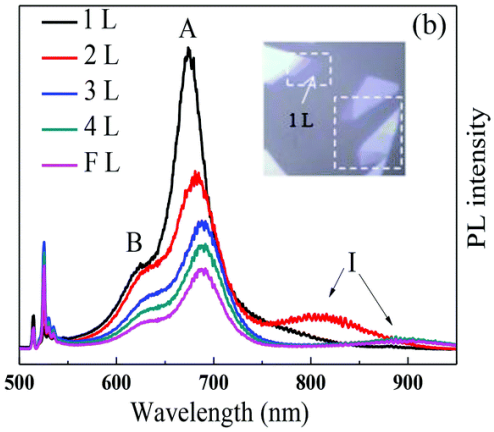

Figure 4.8: Photoluminescence from monolayer to few-layer of MoS_2. The A and B exciton peaks, the indirect transition (I) are denoted and the layer number is depicted by different colours. Spectra was taken at room temperature and with the excitation laser of 514 nm.(30) [Nanoscale. 2014; 6(21):13028-35] - Reproduced by permission of The Royal Society of Chemistry.

4.6 Optoelectronic setup

In this section the systems used for the measurements and acquisition of data are presented. First of all, the microscope setup is explained specifically for the Raman/photoluminescence measurements and then the set-up for the optical transmittance spectroscopy is discussed.

4.6.1 Microscope setup

The following setup was develop in our group and it can be used for a wide range of measurements such as: transmittance (T), reflectance (R), Raman, photoluminescence, Scanning Photocurrent Microscopy (SPCM), electroluminescence with the possibility to perform simultaneously electrical and optical measurements (31).

The system is built on a vibrational isolated optical table and for the reflection measurements a white light-emitting-diode (LED) is used whereas for transmittance measurements the built-in lamp and condenser (Cond) lens that are underneath the stage of an upright microscope are used. For the electrical measurements a grounded BNC box is connected to different equipment such as Lock-in amplifiers and/or Keithley and the sample is bonded on the custom-built-printed circuit board (PCB) chip carrier. The chip carrier is connected to the BCN box either in air or using a vacuum chamber connected to a vacuum pump.

The system is equipped with five continuous wave lasers in the wavelength range from ultraviolet (UV, 375 nm) to visible. The wavelengths of the lasers are 473 nm for hafnium oxide oxidation, 514 nm for photoluminescence and Raman, 561 nm and 685 nm. The laser light path is enclosed, using tube lens and magnetic

interlocks for safety purposes. Moreover, each laser is selected and modulated and its power (from 30 to 50 mW) is controlled digitally.

The microscope is equipped with a motorized XYZ stage, camera and x 5, x 10, x 20, x 50 (short and long working distances) magnifications lenses. The system can fit different types of filters in different custom-built drop-in-filters (DiF) such as: neutral density filters (ND), polarisers, notch filter, bandpass (BP) and beam splitters (BS).

The spectrometer contains three different dispersion gratings: 1200 g/mm with 500 nm and 700 nm blaze, and 1800 g/mm with 500 nm blaze that are chosen depending on the kind of measurements and it is equipped by a (CCD) that is cooled down by a Peltier cooler as shown in figure 4.9. The typical wavelength for Raman of graphene is 532 nm.

The chosen laser light is guided by a series of kinematic (M_{xy}) and fixed mirrors (M) to the illumination path of the optical microscope splitting the beam by a 50/50 beam splitter and then targeting the sample as shown in figure 4.10. The Raman signal from the sample is collected by a flip mirror (FM) directed into the spectrometer through the slit as shown in figure 4.11. The beam is then re-collimated by the collimating mirror onto a diffraction grating that disperses the incident light (depending of the number of lines per milimeter and the angle of the grating with respect to the incoming beam) onto a focusing mirror for exiting the spectrometer and directing onto the CCD with a computer read out interface.

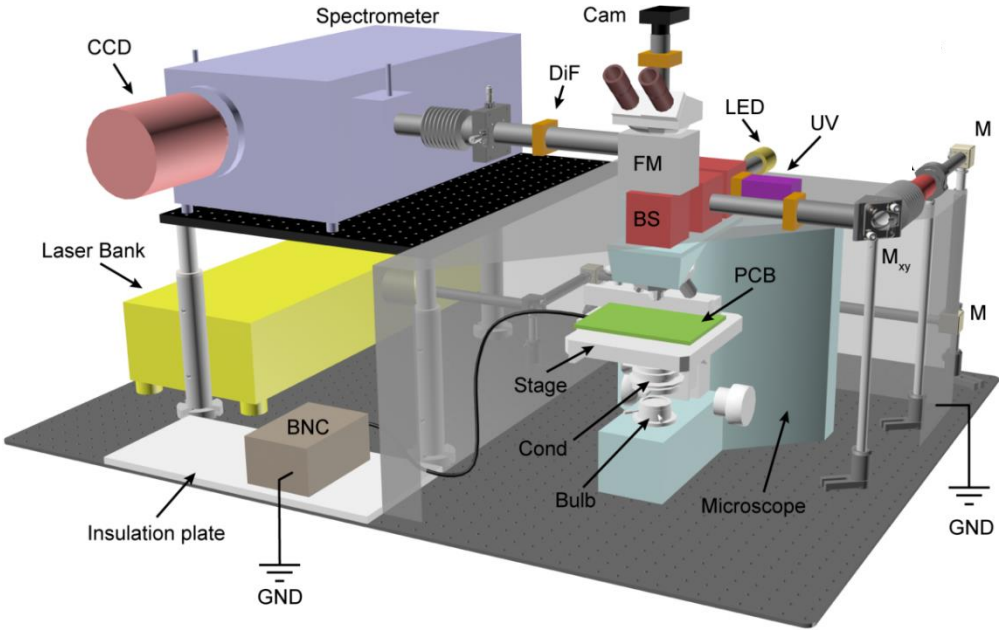

Figure 4.9: 3D schematic of the microscope set up on a vibration-isolated optical table. The system contains the spectrometer (pale purple) with the charge-coupled device CCD (pink), the laser bank (yellow) with the laser lines of 375 nm, 473 nm, 514 nm and 561 nm, the grounded (GND) BNC on an insulation plate, the camera (Cam, in black), the custom-built drop in-filter (DiF, in brown), the flip mirror (FM, in grey), the beam splitter (BS, in red), the custom-built-printed circuit board (PCB, in green), the microscope and its stage, the condenser (Cond), bulb, the light-emitting diode (LED, in yellow), ultraviolet laser (UV, in purple), the kinematic (M_{xy}) and fixed mirrors (M). Tub lens are used for cover the laser and light path Reproduced with permission (31).

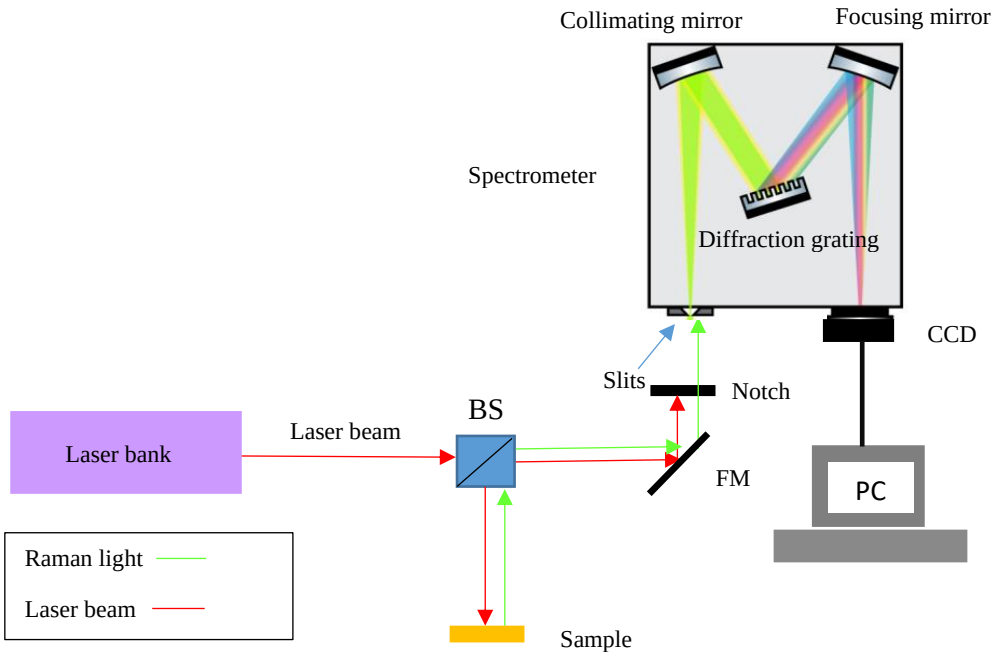

Figure 4.10: Raman setup. The laser beam (red arrow) exits the laser bank (in purple) onto a beam splitter (BS, in blue) and 50 % of the laser beam is directed onto a sample (in orange) whereas the other 50 % is reflected onto the flip mirror (FM in black). The Raman light (green arrow) from the sample is directed through the beam splitter onto the flip mirror for entering the spectrometer through the slits. The beam is collimated on the collimating mirror and dispended by the diffraction grating. The dispersed beam is directed on the focusing mirror and exits the spectrometer leading onto the CCD.

4.6.2 Transmittance

The optical transmittance (T) is the fraction of light that passes through a sample relative to the light transmitted through the transparent substrate as shown in figure 4.11.

$$T = \frac{T_{sample}}{T_{substrate}} \tag{4.5}$$

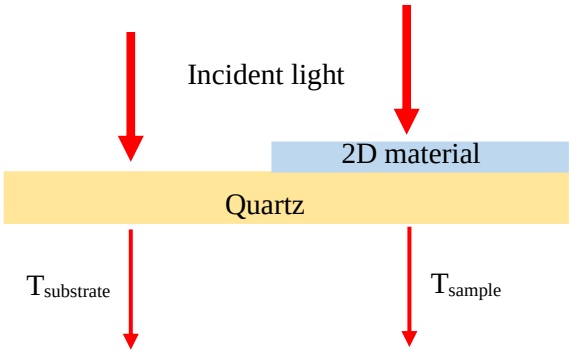

Figure 4.11: Optical transmittance. The incident light is shone on the substrate and on the 2D material, then the transmitted light is collected through the sample and through the substrate. 2D material in blue, quartz as transparent substrate and red arrows for the incident and transmitted light.

The setup used for these measurements is shown in figure 4.12 where the broadband light source shines the light on the first objective lens set to be collimated and projected on the sample held by the sample holder. The transmitted light through the sample is collimated by the second objective lens set and directed onto an entrance slit of the spectrometer that has three mirrors and a diffraction grating. The incoming light through the slit gets focused onto the mirror. Afterwards, the light is collimated onto the diffraction grating and dispersed by the grating and redirected by two mirrors exiting the spectrometer through the slits and directing onto the CCD with a computer read out interface.

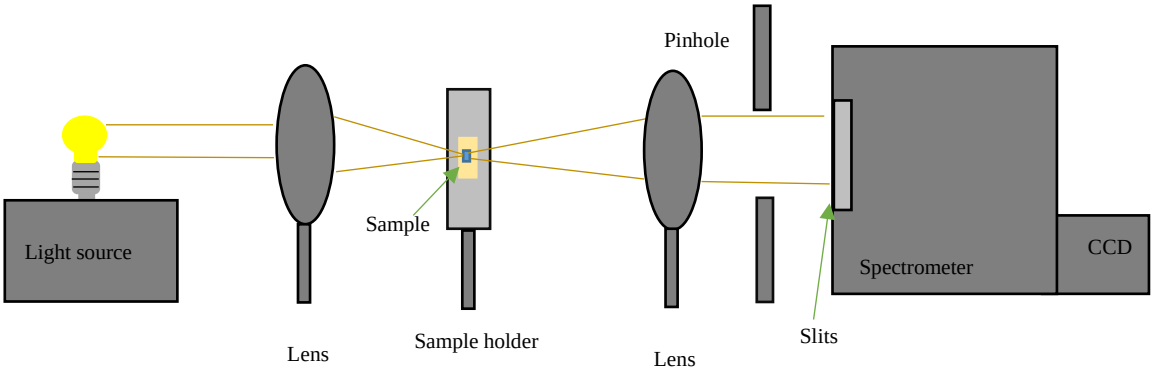

Figure 4.12: Optical transmittance setup. The light source emits light that is collimated on the first objective lens set and shone onto the sample that is held by the sample holder. The transmitted light through the sample is collected by the second objective lens set and focused onto an entrance slit of the spectrometer equipped with a CCD. Solid parts are in grey including the lens, sample holder, spectrometer and CCD. The sample is in blue and the light path is denoted by brown.

Optical transmittance, like reflectance (differential reflectance), provides a wide variety of the optical transitions peaks such as the excitons of TMDCS as was reported by R.Frisenda et al. (32) for WS_2, MoS_2, WSe_2 and $MoSe_2$. With the correct differential treatment of the recorded spectra the excited states of the excitons are accessible as it will be explained in Chapter 6.

This chapter starts with the theory of Raman covering Graphene and TMDCs and moving into photoluminescence and it finishes with the handmade set up used for the measurements. In the last two chapters the results are showed focusing in vdW heterostructures samples.

Bibliography

1. Ferrari AC, Basko DM. Raman spectroscopy as a versatile tool for studying the properties of graphene. Nat Nanotechnol. 2013;8:235-46.
2. Wang YY, Ni ZH, Yu T, Shen ZX, Wang HM, Wu YH, et al. Raman studies of monolayer graphene: The substrate effect. J Phys Chem C. 2008;112:10637-40.
3. Raman CV, Krishnan KS. A New Type of Secondary Radiation. Nature. 1928;121:501-2.
4. Lewis IR, Edwards H. Handbook of Raman Spectroscopy: From the Research Laboratory to the Process Line: CRC Press; 2001.
5. Jorio A, Dresselhaus MS, Saito R, Dresselhaus G. Raman Spectroscopy in Graphene Related Systems: Wiley; 2011.
6. Basko DM, Piscanec S, Ferrari AC. Electron-electron interactions and doping dependence of the two-phonon Raman intensity in graphene. Phys Rev B. 2009;80:165413.
7. Beams R, Cancado LG, Novotny L. Raman characterization of defects and dopants in graphene. J Phys-Condens Mat. 2015;27:8.
8. Malard LM, Pimenta MA, Dresselhaus G, Dresselhaus MS. Raman spectroscopy in graphene. Physics Reports. 2009;473:51-87.
9. Ferrari AC. Raman spectroscopy of graphene and graphite: Disorder, electron–phonon coupling, doping and nonadiabatic effects. Solid State Commun. 2007;143:47-57.
10. Wang YY, Ni ZH, Shen ZX, Wang HM, Wu YH. Interference enhancement of Raman signal of graphene. Appl Phys Lett. 2008;92:043121.
11. Pimenta MA, del Corro E, Carvalho BR, Fantini C, Malard LM. Comparative Study of Raman Spectroscopy in Graphene and MoS_2-type Transition Metal Dichalcogenides. Accounts of Chemical Research. 2015;48:41-7.
12. Das A, Chakraborty B, Sood AK. Raman spectroscopy of graphene on different substrates and influence of defects. B Mater Sci. 2008;31:579-84.
13. Ferrari AC, Meyer JC, Scardaci V, Casiraghi C, Lazzeri M, Mauri F, et al. Raman spectrum of graphene and graphene layers. Phys Rev Lett. 2006;97:187401.
14. Ni ZH, Wang YY, Yu T, Shen ZX. Raman Spectroscopy and Imaging of Graphene. Nano Res. 2008;1:273-91.
15. Ni ZH, Wang HM, Kasim J, Fan HM, Yu T, Wu YH, et al. Graphene thickness determination using reflection and contrast spectroscopy. Nano Letters. 2007;7:2758-63.
16. Yoon D, Moon H, Cheong H, Choi JS, Choi JA, Park BH. Variations in the Raman Spectrum as a Function of the Number of Graphene Layers. J Korean Phys Soc. 2009;55:1299-303.
17. Ye M, Winslow D, Zhang D, Pandey R, Yap YK. Recent Advancement on the Optical Properties of Two-Dimensional Molybdenum Disulfide (MoS_2) Thin Films. Photonics. 2015;2:288-307.
18. Zhang X, Qiao XF, Shi W, Wu JB, Jiang DS, Tan PH. Phonon and Raman scattering of two-dimensional transition metal dichalcogenides from monolayer, multilayer to bulk material. Chem Soc Rev. 2015;44:2757-85.
19. Amber McCreary RG, ‖ Matin Amani, Jin Wang, Karel-Alexander N. Duerloo,Ankit Sharma,Karalee Jarvis, Evan J. Reed, Avinash M. Dongare, Sanjay K. Banerjee,, Mauricio Terrones RRN, ‡ and Madan Dubey. Effects of Uniaxial and Biaxial Strain on Few-Layered Terrace Structures of MoS2 Grown by Vapor Transport. Acs Nano. 2016;10:3186-97.
20. Terrones H, Del Corro E, Feng S, Poumirol JM, Rhodes D, Smirnov D, et al. New First Order Raman-active Modes in Few Layered Transition Metal Dichalcogenides. Sci Rep-Uk. 2014;4.
21. Zeng HL, Zhu BR, Liu K, Fan JH, Cui XD, Zhang QM. Low-frequency Raman modes and electronic excitations in atomically thin MoS_2 films. Phys Rev B. 2012;86:241301.
22. Lee C, Yan H, Brus LE, Heinz TF, Hone J, Ryu S. Anomalous Lattice Vibrations of Single- and Few-Layer MoS_2. Acs Nano. 2010;4:2695-700.

23. Molina-Sánchez A, Wirtz L. Phonons in single-layer and few-layer MoS_2 and WS_2. Phys Rev B. 2011;84:155413.
24. Wilson J, Hawkes JFB. Optoelectronics - An introduction (2nd edition)1989 January 01, 1989.
25. Jia GY, Liu Y, Gong JY, Lei DY, Wang DL, Huang ZX. Excitonic quantum confinement modified optical conductivity of monolayer and few-layered MoS_2. Journal of Materials Chemistry C. 2016;4:8822-8.
26. Woodward RI, Kelleher EJR. 2D Saturable Absorbers for Fibre Lasers. Appl Sci-Basel. 2015;5:1440-56.
27. Mouri S, Miyauchi Y, Matsuda K. Tunable Photoluminescence of Monolayer MoS_2 via Chemical Doping. Nano Letters. 2013;13:5944-8.
28. Mak KF, Lee C, Hone J, Shan J, Heinz TF. Atomically Thin MoS_2: A New Direct-Gap Semiconductor. Phys Rev Lett. 2010;105:136805.
29. Tonndorf P, Schmidt R, Bottger P, Zhang X, Borner J, Liebig A, et al. Photoluminescence emission and Raman response of monolayer MoS_2, $MoSe_2$, and WSe_2. Opt Express. 2013;21:4908-16.
30. Dhakal KP, Duong DL, Lee J, Nam H, Kim M, Kan M, et al. Confocal absorption spectral imaging of MoS_2: optical transitions depending on the atomic thickness of intrinsic and chemically doped MoS_2. Nanoscale. 2014;6:13028-35.
31. Sanctis AD, Jones GF, Townsend NJ, Craciun MF, Russo S. An integrated and multi-purpose microscope for the characterization of atomically thin optoelectronic devices. Review of Scientific Instruments. 2017;88:055102.
32. Frisenda R, Niu Y, Gant P, Molina-Mendoza AJ, Schmidt R, Bratschitsch R, et al. Micro-reflectance and transmittance spectroscopy: a versatile and powerful tool to characterize 2D materials. Journal of Physics D: Applied Physics. 2017;50:074002.

Chapter 5: Laser writable high-K dielectric for van der Waals nanoelectronics

5.1 Introduction and previous work

Electronics has relied on the semiconductor silicon (Si, energy bandgap of 1.1 eV) as a fundamental material. Silicon reacts with oxygen and forms-its "native" insulator- silicon dioxide which is useful for devices such as random-access-memories, field-effect transistor where SiO_2 is used as a gate dielectric to list a few (1). However, the widely used dielectric material - silicon dioxide - has a limited use as the leakage current through the dielectric increases as the thickness of the oxide is decreased which is a well-known problem (1). Downscaling of the dimensions of FETs including the width and length of the channel and the reduction of the gate oxide thickness reaches a physical limit (2) (~ 1.0 - 1.8 nm for SiO_2) which increases the leakage current leading to reliability issues (1, 3). S.H.Lo et al. reported a calculated value of 1.5 nm thickness of SiO_2 with density leakage current of 10^2 A/cm^2 (4). The state-of-the-art vdW devices has relied on high purity hexagonal boron nitride for different purposes as tunnel barriers (5), gate and substrate (6). Nevertheless, its dielectric constant (κ ~ 4) (7) is similar to SiO_2 (κ ~ 3.9) (1, 8) which prevents further downscaling of the devices addressing the need of high- κ materials.

As a solution SiO_2 (κ = 3.9 (1)) substitution for high-κ materials (κ =16 to 20 (9)) is proposed as the capacitance between the gate dielectric (2) and the channel would increase which means that there is a wider range to choose the thickness of the capacitor while keeping a high capacitance ($C = \varepsilon_0 \varepsilon_r A/d$ from chapter 2). These materials has the advantage of allowing efficient charge injection into transistor channel with low leakage currents due to the high capacitance (2).

Previous work in high-κ materials' native oxides has been done such as :M.J. Mleczko et al. reported a FET with exfoliated few-layers $HfSe_2$ ($ZrSe_2$) with mobilities ranging from 1 to 4 cm^{2}V^{-1}s^{-1} (1 to 1.5 cm^{2}V^{-1}s^{-1}) at room temperature (9). Moreover, they reported a top-gated-few-layers $HfSe_2$ transistor with native HfO_2 dielectric reaching the mobility of 0.3 cm^{2}V^{-1}s^{-1}. B.Chamlagain et al. shown a few-layers MoS_2 FET with Ta_2O_5 working as a bottom and top gate with the mobility of 61.5 cm^{2}V^{-1}s^{-1} (10).

However, the high-κ dielectric implementation in van der Waals (vdW) heterostructures (11) has not been probed yet despite the fast growing family of layered 2D materials (12). Multiple vdW heterostructures combinations within devices have been reported for instance graphene tunnelling FET with a vertical structure (13), light-emitting quantum well (LEQWs) with WSe_2 ($MoSe_2$) monolayers encapsulated by h-BN tunnel barriers with top and bottom graphene electrodes, single quantum well (SQW) and multiple quantum well (MQW) light emitting diode (LED) of monolayer MoS_2 and WS_2 with h-BN tunnelling barriers and graphene electrodes (14). 2D materials have been implemented in memory

devices (15) and in photovoltaics (16-19) such as ionic-polymer gated WS_2-graphene photodetectors (20).

In microfabrication; sputtering, evaporation and chemical vapour deposition (CVD) are the most used deposition techniques (21). These techniques are not suitable for 2D materials fabrication: sputtering is based on plasma and molecular-level bombardments which damages the underneath thin materials (21). Evaporation and CVD create thin films from tens to hundreds nanometres thick (21).Therefore, novel routes or technology of the implementation of high-κ materials, compatible with 2D materials, need to be researched.

5.2 Photo-oxidation of HfS_2 into HfO_x

The novelty of this project is to embed ultrathin HfO_x in vdW heterostructures devices using selectively in-situ photo-oxidation of HfS_2 to avoid other deposition methods for instance atomic layer-deposition (ALD). X.Tang et al. reported the damage of the deposition of HfO_2 and Al_2O_3 on few-layer and monolayer graphene by ALD where the damage on monolayer graphene is more noticeable than for few-layers (22).

HfS_2 is a semiconducting transition metal dichalcogenide that has an indirect energy bandgap of 2.85 eV in its bulk form (23, 24) whereas for monolayer the indirect energy bandgap is around ~ 1.2 eV with 0.7 nm thickness (25). Monolayer HfS_2 (S-Hf-S) is bonded in-plane by covalent forces whereas few-layers are held together by van der Waals forces. In the monolayer limit, the crystal structure shows tetragonal symmetry (1T) phase (25) as shown in figure 2.6 (c) (26). The heterostructures were fabricated following the mechanical exfoliation and stacking transfer procedures explained in Chapter 3.
The 2D materials were purchased from HQ Graphene and h-BN and MoS_2 were acquired from Manchester Nanomaterials. Flakes were mechanically exfoliated and vdW heterostructures were fabricated by the techniques explained in Chapter 3. More specifically, HfS_2 was exfoliated and placed on the stack where the dielectric (HfO_x) was required and the contacts were defined by electron beam lithography. The desired region of HfS_2 was photo-oxidised into HfO_x (energy bandgap of ~ 5.5 eV (27)) with 473 nm laser irradiation wavelength with the energy density of 53 mJ/μm^2 and 1 to 2 seconds exposure per point of the HfS_2 layer with the equipment described in the section 4.6.1.

HfS_2 photo-oxidation was shown by A.D.Sanctis et al. that ultra-thin HfS_2 upon laser irradiation oxidises into HfO_x due to the charge transfer between the semiconductor and the water redox presented on its surface (28). Therefore, the atmospheric water is needed on the semiconductor surface for the reaction to happen (28). An oxygen-water redox reaction leads to aqueous oxygen diluted within the water (28):

$$2H_2O \leftrightarrow O_2\,(aq) + 4e^- + 4H^+ \qquad (5.1)$$

When HfS_2 is optically excited ($HfS_2 + h\nu \rightarrow Hf{S_2^*}$), free carriers are created and transferred to oxygen creating a radical anion (O_2^-) that reacts with HfS_2 giving

HfO_2 and SO_2 as shown in the following chemical reaction (28) as O_2 binds to the metal:

$$HfS_2\,(s) + 3O_2\,(aq) + h\nu \rightarrow HfO_2\,(s) + 2SO_2\,(g) \qquad (5.2)$$

Where s denotes solidus, aq aqueous and g gaseous.

The charge carriers are transferred towards aqueous oxygen at the surface and the reaction depends on the band alignment between the material (HfS_2) and the redox potentials of the redox reaction of water and oxygen (equation 5.1) presented in air which means that not all 2D materials can be photo-oxidised (29).

Figure 5.1 (a) shows a graphene/HfS_2 heterostructure on Si/SiO_2 substrate as-fabricated on the left, in the middle the laser exposure for the photo-oxidation process turning into HfO_x (right) making the photo-oxidation possible when HfS_2 is embedded in heterostructures and under metallic contacts. This process is probed for the encapsulated HfS_2 between graphene and h-BN shown in the top of figure 5.1 (e).This sample was photo-oxidised within the vacuum chamber (blue hatched area) and in air (red hatched area) of the bottom of the figure 5.1 (e). HfS_2 oxidation relies on the atmospheric water and/or oxygen in air as can be compared for the micrograph. After the HfS_2 exfoliation, its surface oxidised naturally before the encapsulation allowing the diffusion of atmospheric water between graphene and more hydrophilic already oxidised HfO_x surface. This water intercalation/diffusion at ambient conditions has been reported previously for graphene and silicon samples by D.Lee et al. (30).

Cross-sectional high-resolution scanning transmission electron microscope (HR STEM) has been proved to be a useful tool capable of providing atomic resolution for heterogeneous samples as shown by A. P. Rooney et al. for encapsulated monolayer $MoSe_2$, $NbSe_2$ and MoS_2 in h-BN (31) and S. J. Haigh et al. in graphene-h-BN stack (32). HR STEM measurements were taken in an FEI Dual Beam Nova instrument incorporating a focused ion beam and a scanning electron microscope in the same chamber. In figure of 5.1 (b) a HR STEM image of a cross section of HfO_x encapsulated by graphene device is shown in which graphene can be distinguish from the amorphous phase of HfO_x. On the right of the figure 5.1 (b), energy-dispersive X ray (EDX) analysis of the same heterostructure presents hafnium and oxygen species with a low level of sulphur after the laser irradiation indicating the formation of HfO_x. To characterise the doping level of graphene a FET made by h-BN substrate capped with graphene before and after HfS_2 transfer and oxidation is shown in figure 5.1 (f). After the oxidation there a small n-type doping and a negligible D peak in the Raman spectra of graphene appears in the inset of figure 5.1 (f) indicating that graphene does not undergo a significantly damage after the laser irradiation.

The current-voltage (I_{sd}-V_{sd}) curves were done using a Keithley 2400 voltage/current source meter and the electrical characterization of dual-gated graphene FET was performed using a standard low-noise AC lock-in techniques using a Signal Recovery 7225 lock-in amplifier and a Keithley 2400 source meter providing gate voltage and a vacuum of 10^{-3} mbar.To characterise the insulating properties of the laser-written HfO_x a FET with MoS_2 channel, graphene gate

electrode, gold/chromium contacts and 8-nm thick HfS_2 in between graphene and the channel is fabricated as shown in the top of figure 5.1 (c). After the photo-oxidation, HfO_x is transparent indicating that the bandgap has increased from 2.85 eV for HfS_2 to 5.5 eV HfO_x. This device was electrically characterised by vertical electron transport measurements giving the I_{sd}-V_{sd} curves as shown in figure 5.1 (d). Previously to the oxidation, the current-voltage curve for MoS_2 semiconductor with a resistivity of $\rho \sim 20 \times 10^6\ \Omega\ \mu m^2$ shows a similar behaviour that was reported by T. Georgiou et al. (33) in graphene-WS_2 field-effect tunnelling transistor (FETT). After the oxidation, however, the resistivity is $\rho \sim 10^{11}\ \Omega\ \mu m^2$ indicating that an oxide formation for small bias.

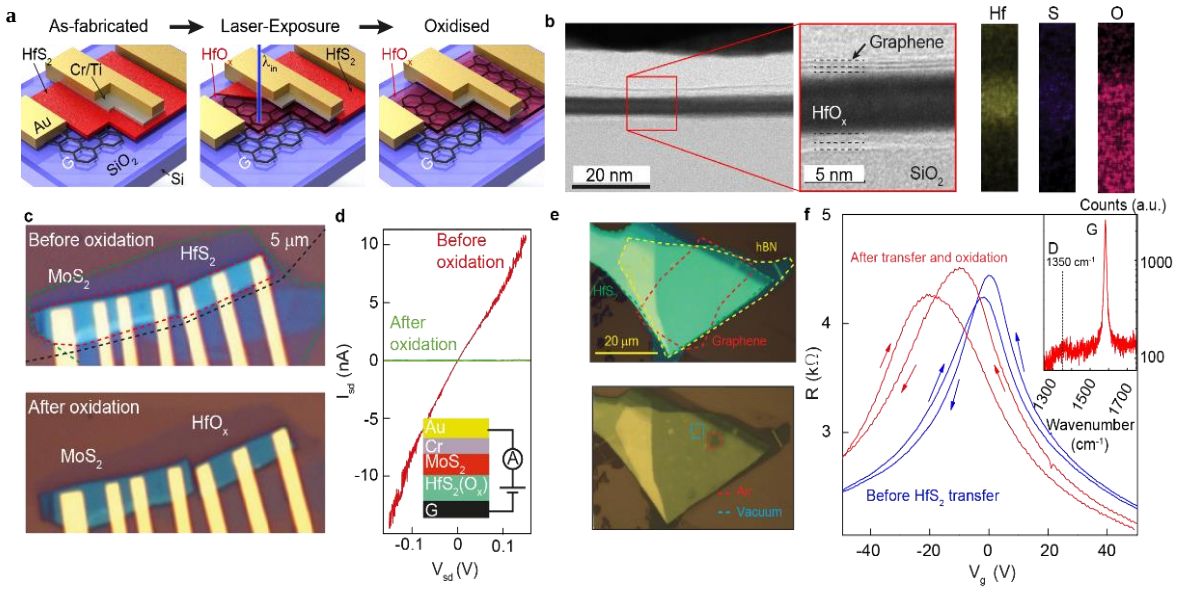

Figure 5.1: Photo-oxidation of HfF_2 into HfO_x and its characterisation. (a) Schedule of the heterostructure from the fabrication (left), laser irradiation (middle) and after the oxidation of the HfS_2 into HfO_x (right). (b) STEM image of the cross section of graphene/HfO_x/graphene heterostructure on Si/SiO_2 substrate after laser irradiation (left) and EDX elemental analysis (right). (c) Optical image of graphene/HfO_x/MoS_2 heterostructure as a FET (top) before and (bottom) after the photo-oxidation. Green outlines for HfOx, red outlines for MoS_2 and black outlines for graphene. (d) Current (I_{sd})-voltage (Vs_d) curves for the device in (c) before (red) and after (green) the photo-oxidation. Bottom right inset: The stacking sequence. (e) Top: Optical micrograph of graphene-HfO_x-hBN heterostructure. Bottom: Same optical micrograph after the photo-oxidation within the vacuum chamber in vacuum (blue hatched area) and in air (red hatched area). The pressure was around ~ 10^{-5} mbar and no oxidation was obserbed that that pressure. (f) Two-terminal resistance versus gate voltage for a FET of graphene on h-BN (~ 40 nm) on Si/SiO_2 substrate measured at 266 K in helium atomsphere (blue curve) and after placing HfS_2 and been oxidised (red curve, sweep rate = 10V/min). Raman of graphene after the oxidation showing the G peak and a negligible D peak in the inset.

5.3 Breakdown and dielectric constant of HfO_x

The breakdown voltage of HfO_x was measured with a vertical electron tunnelling device graphite/HfO_x/Cr (5nm)/Au (60nm) as shown in the inset of schematic of figure 5.2 (a) where the tunnel current is measured applying a source-drain bias across the vertical junction as shown in figure 5.2 (a) with a voltage range from

-2 to 2 V. In the top left inset the Fowler-Nordheim tunnelling model is shown for the fitted data where height value of the barrier of Φ_B ~ 1.15 eV (34).

The voltage range for the figure 5.2 (b) was increased to determine the breakdown electric field of ~ 0.5-0.6 V/nm where the current discontinuously increases reaching the compliance level of the voltage source meter around ~ 3 V. This breakdown value is comparable to that SiO_2 from 0.6 to 2.5 V/mm (35) and h-BN 1 V/mm (36).

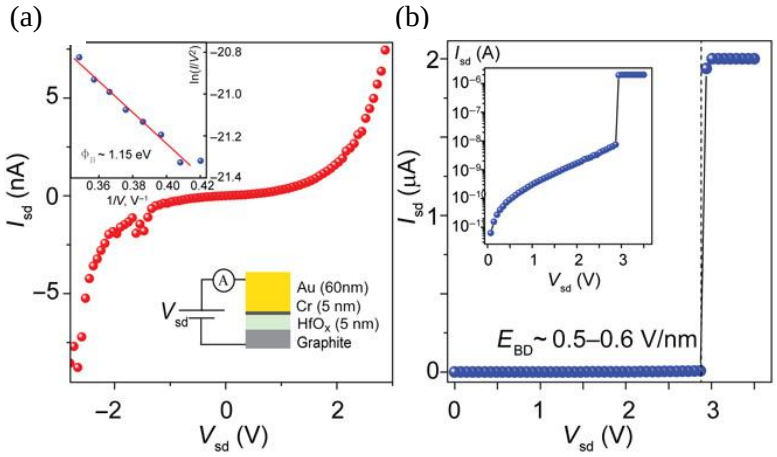

Figure 5.2: HfO_x dielectric breakdown. (a) Graphite/HfO_x/Cr/Au junction I_{sd}-V_{sd} curve. Bottom right inset: Device schematic. Top left inset: Fowler-Nordheim tunnelling theory fit. (b) I_{sd}-V_{sd} curve for extended voltage range showing the breakdown field. Inset: Log scale of the same data showing the exponential dependence of the tunnelling current.

A dual-grated graphene FET is fabricated for better understanding of the dielectric properties of the photo-oxidised HfO_x where the structure sequence is shown in the bottom inset of figure 5.3 (a) where bilayer graphene is the channel, SiO_2 (285 nm) is the back gate, HfO_x (7nm) is the top gate and Cr/Au is used for the contacts. In this current-voltage (I_{sd}-V_{sd}) measurements contact lead 5 is used as a source and 1 and 2 for drains. Figure 5.3 (b) contains the optical micrograph of the sample with the lead contacts number so that contact 1, 2 and 11 are placed directly on the bilayer graphene and on top of HfO_x contact 3 to 11.The current-voltage measurements show the initial/partial breakdown as the voltage is increased reaching the compliance level for the red curve and in the sweep down to around -3 V the conductive filament is completely broken as shown in the blue curve reaching the breakdown electric field. For further cycling of the source-drain bias with increasing the current compliance leads to the non-reversible conductive filament formation that allows direct contact between the Cr/Au and bilayer graphene as shown of the black curve. The selectively breakdown of the conductive filament allows to form the contact between the top Cr/Au metal contact and graphene underneath HfO_x therefore there is a freedom of choosing the contacts such as contacts 7 and 8 for source and voltage probes and contact 9, 10 and 11 as drain and voltage probes while contacts 3, 6 and 8 are used as top gates for figure 5.3 (b). For this configuration the resistance is measured for different values of top gate from -60 V to 60 V where graphene charge neutrality point is shifted as the bias is increased. Figure 5.3 (c) shows a

four-terminal top-back gate contour plot of the four-point channel resistance between the contacts 7 and 9 as a source and drain contacted trough conductive filaments and 8 as a top gate electrode.

Using the equations 2.6 and 2.7 from Chapter 2 for SiO_2 and HfO_x and taking into account the hafnium thickness measured by AFM and the slope of the black curve at that point the carrier density of hafnium oxide top gate and silicon dioxide back gate are equal, the dielectric constant of hafnium oxide is calculated. The extracted dielectric constant for HfO_x has the value of ~ 15 ± 1 which is similar to the previously reported values by A.Callegari et al. (37) and M.Osada et at. (2).

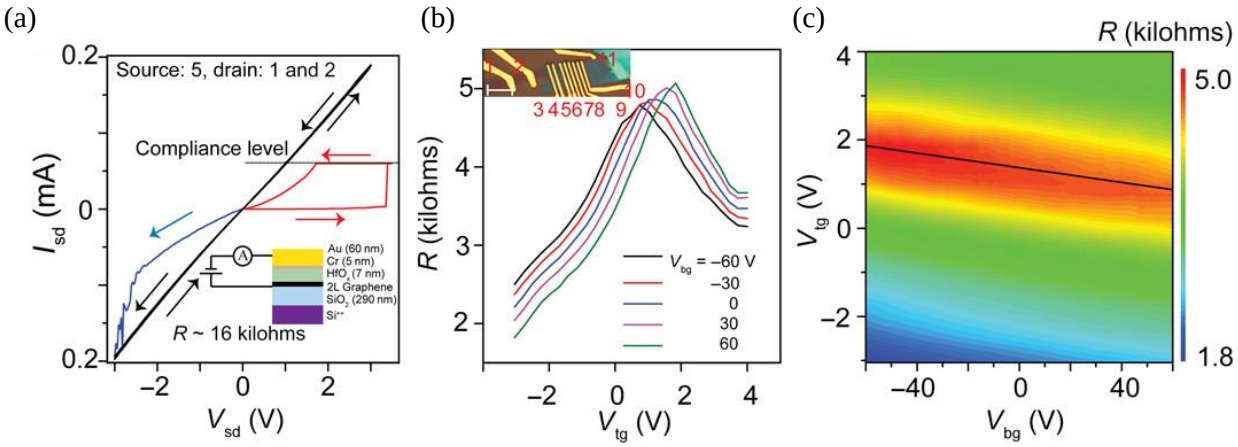

Figure 5.3: Dual-gated graphene FET with HfO_x as top gate and SiO_2 as back gate. (a) Current-voltage (I_{sd}-V_{sd}) curves indicating the initial breakdown of HfO_x (red curve), further breakdown (blue curve) and completely broken and conductive filament formation (black curve). Metal lead 5 for the source and 1 and 2 for the drains. Top right inset: the schematic of the device. The cycling orientations is indicated by the arrows. (b) R (V_{tg}) curves for values from -60 V to 60 V for the back gate. Top left inset: Optical micrograph for the schematic of the figure 5.4 (a) with the metal contact numbers: 1, 2 and 11 on bilayer graphene and from 3 to 10 on HfO_x. (c) Four-terminal top back-gate contour plot for the channel resistance with contact 8 as top gate and contacts 7 and 9 as source and drain.

5.4 Resistive switching memory devices

Resistive switching memory devices are promissing candidates for future non-volatile memory generation especially oxide-based RRAM as they are compatible with the complementary metal-oxide-semiconductor (CMOS) technology (38, 39). RRAM have attracted attention due to low power consumption (40), retention and high speed (41). Previously L.Zhang et al. reported the degradation with the cyles of bipolar switching HfO_x-based RRAM with the structure of $TiN/TiO_x/HfO_x/TiN$ (39). S.Yu et al., however, probed the stability over the cycles of HfO_x-based vertical RRAM (38).

The RRAMs devices of this project are bipolar switching type devices and are based on the conductive filament mechanism where the filament is forming and ruptured in the Set and Reset processes.The inset of figure 5.4 (a) shows a RRAM consisting on top gold (Au) contacts and chromium (Cr) as a “capping”/adhesion layer between gold and photo-oxidised HfO_x and bottom graphite electrode. After the fabrication, the voltage is applied to the top electrode

respect to the bottom electrode. After the first soft breakdown of HfO_X, the loop is shown in figure 5.4 (a): the Set process is at +1 V from HRS to LRS when the current increases abruptly which means that the conductive filaments are connected. As the polarity is reversed, the device keeps at LRS until -1 V where the current decreases reaching HRS state for the Reset process which means that the conductive filamenst are partially broken. These RRAM devices have a memory window (R_{HRS}/R_{LRS}) of ~5 up to 10^4.

Figure 5.4 (b) shows the current-voltage curves for the 1st and 100th cycles with the same behaviour with almost no change between them keeping the initial condition. In figure 5.4 (c), the V_{sd} was kept at 100 mV where HRS and LRS showing little variation over the 100 cycles. Moreover, the stability of HRS and LRS resistances values were checked at V_{sd} = 250 mV up to 10^4 seconds showing consistency.

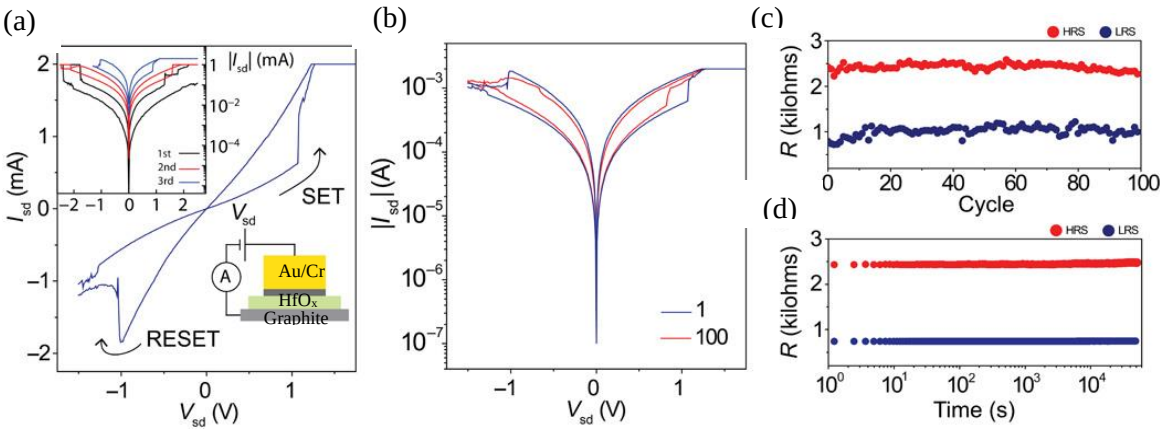

Figure 5.4: RRAM and its performance. (a) I_{sd}-V_{sd} switching cycle with Set and Reset states.Top left inset: $|I_{sd}|$-V_{sd} curves for the first three cycles. Top right inset: The device schematic. (b) $|I_{sd}|$-V_{sd} loops for the 1st and 100th cyles for the same device of (a) for the absolute value of the current. (c) Stability of HRS and LRS resistance values for different number of cycles. (d) HRS and LRS resistance values versus time. Yellow for top gold electrode, dark grey for chromium adhesion layer, green for HfO_x, grey for bottom graphite electrode and HRS (LRS) state in red (blue).

5.5 Conclusions

It has been shown thay ultrathin few-layer HfS_2 can be incorporated in vdW heterostructures and photo-oxidised into amorphous high-κ HfO_x upon laser irradiation without damaging the underneath 2D material. It has been probed that the laser written HfO_x has a dielectric contast of ~ 15 and a breakdown field of ~ 0.5 to 0.6 V/nm. This material has been used for FETs and RRAM showing its compatibility and due to its high dielectric constant provides significant scaling improvement for future applications.

Bibliography

1. Kingon AI, Maria JP, Streiffer SK. Alternative dielectrics to silicon dioxide for memory and logic devices. Nature. 2000;406:1032-8.
2. Osada M, Sasaki T. Two-Dimensional Dielectric Nanosheets: Novel Nanoelectronics From Nanocrystal Building Blocks. Adv Mater. 2012;24:210-28.
3. Suehle JS. Ultrathin gate oxide reliability: physical models, statistics, and characterization. IEEE Transactions on Electron Devices. 2002;49:958-71.
4. Lo S, Buchanan DA, Taur Y, Wang W. Quantum-mechanical modeling of electron tunneling current from the inversion layer of ultra-thin-oxide nMOSFET's. IEEE Electron Device Letters. 1997;18:209-11.
5. Withers F, Del Pozo-Zamudio O, Mishchenko A, Rooney AP, Gholinia A, Watanabe K, et al. Light-emitting diodes by band-structure engineering in van der Waals heterostructures. Nat Mater. 2015;14:301.
6. Dean CR, Young AF, Meric I, Lee C, Wang L, Sorgenfrei S, et al. Boron nitride substrates for high-quality graphene electronics. Nat Nanotechnol. 2010;5:722.
7. Li LH, Santos EJG, Xing T, Cappelluti E, Roldan R, Chen Y, et al. Dielectric Screening in Atomically Thin Boron Nitride Nanosheets. Nano Letters. 2015;15:218-23.
8. Wilk GD, Wallace RM, Anthony JM. High-κ gate dielectrics: Current status and materials properties considerations. J Appl Phys. 2001;89:5243-75.
9. Mleczko MJ, Zhang C, Lee HR, Kuo H-H, Magyari-Köpe B, Moore RG, et al. $HfSe_2$ and $ZrSe_2$: Two-dimensional semiconductors with native high-κ oxides. Science Advances. 2017;3:e1700481.
10. Chamlagain B, Cui Q, Paudel S, Cheng MM-C, Chen P-Y, Zhou Z. Thermally oxidized 2D TaS2 as a high-κ gate dielectric for MoS_2 field-effect transistors. 2d Mater. 2017;4:031002.
11. I.V. Grigorieva and A.K.Geim. Van der Waals heterostructures. Nat. 2013;499:419-425
12. Miró P, Audiffred M, Heine T. An atlas of two-dimensional materials. Chem Soc Rev. 2014;43:6537-54.
13. Britnell L, Gorbachev RV, Jalil R, Belle BD, Schedin F, Mishchenko A, et al. Field-Effect Tunneling Transistor Based on Vertical Graphene Heterostructures. Science. 2012;335:947-50.
14. Withers F, Del Pozo-Zamudio O, Mishchenko A, Rooney AP, Gholinia A, Watanabe K, et al. Light-emitting diodes by band-structure engineering in van der Waals heterostructures. Nat Mater. 2015;14:301-6.
15. Bertolazzi S, Krasnozhon D, Kis A. Nonvolatile Memory Cells Based on MoS_2/Graphene Heterostructures. Acs Nano. 2013;7:3246-52.
16. Furchi MM, Pospischil A, Libisch F, Burgdörfer J, Mueller T. Photovoltaic Effect in an Electrically Tunable van der Waals Heterojunction. Nano Letters. 2014;14:4785-91.
17. Lee C-H, Lee G-H, van der Zande AM, Chen W, Li Y, Han M, et al. Atomically thin p–n junctions with van der Waals heterointerfaces. Nat Nanotechnol. 2014;9:676-81.
18. Withers F, Yang H, Britnell L, Rooney AP, Lewis E, Felten A, et al. Heterostructures Produced from Nanosheet-Based Inks. Nano Letters. 2014;14:3987-92.
19. McManus D, Vranic S, Withers F, Sanchez-Romaguera V, Macucci M, Yang H, et al. Water-based and biocompatible 2D crystal inks for all-inkjet-printed heterostructures. Nat Nanotechnol. 2017;12:343-50.
20. Mehew JD, Unal S, Torres Alonso E, Jones GF, Fadhil Ramadhan S, Craciun MF, et al. Fast and Highly Sensitive Ionic-Polymer-Gated WS2–Graphene Photodetectors. Adv Mater. 2017;29:1700222.
21. Kim HG, Lee H-B-R. Atomic Layer Deposition on 2D Materials. Chemistry of Materials. 2017;29:3809-26.
22. Tang X, Reckinger N, Poncelet O, Louette P, Ureña F, Idrissi H, et al. Damage evaluation in graphene underlying atomic layer deposition dielectrics. Sci Rep-Uk. 2015;5:13523.

23. Traving M, Seydel T, Kipp L, Skibowski M, Starrost F, Krasovskii EE, et al. Combined photoemission and inverse photoemission study of ${\mathrm{HfS}}_{2}$. Phys Rev B. 2001;63:035107.
24. Kreis C, Werth S, Adelung R, Kipp L, Skibowski M, Krasovskii EE, et al. Valence and conduction band states of ${\mathrm{HfS}}_{2}:$ From bulk to a single layer. Phys Rev B. 2003;68:235331.
25. Kanazawa T, Amemiya T, Ishikawa A, Upadhyaya V, Tsuruta K, Tanaka T, et al. Few-layer HfS2 transistors. Sci Rep-Uk. 2016;6:22277.
26. Singh D, Gupta SK, Sonvane Y, Kumar A, Ahuja R. 2D-HfS_2 as an efficient photocatalyst for water splitting. Catalysis Science & Technology. 2016;6:6605-14.
27. Cheynet MC, Pokrant S, Tichelaar FD, Rouvière J-L. Crystal structure and band gap determination of HfO2 thin films. J Appl Phys. 2007;101:054101.
28. De Sanctis A, Amit I, Hepplestone SP, Craciun MF, Russo S. Strain-engineered inverse charge-funnelling in layered semiconductors. Nat Commun. 2018;9.
29. Favron A, Gaufrès E, Fossard F, Phaneuf-L'Heureux A-L, Tang NYW, Lévesque PL, et al. Photooxidation and quantum confinement effects in exfoliated black phosphorus. Nat Mater. 2015;14:826-32.
30. Peimyoo N. et al.Laser writable high-K dielectric for van der Waals nano-electronics.Science Advances. 2019; 5:1-8.
31. Rooney AP, Kozikov A, Rudenko AN, Prestat E, Hamer MJ, Withers F, et al. Observing Imperfection in Atomic Interfaces for van der Waals Heterostructures. Nano Letters. 2017;17:5222-8.
32. Haigh SJ, Gholinia A, Jalil R, Romani S, Britnell L, Elias DC, et al. Cross-sectional imaging of individual layers and buried interfaces of graphene-based heterostructures and superlattices. Nat Mater. 2012;11:764-7.
33. Georgiou T, Jalil R, Belle BD, Britnell L, Gorbachev RV, Morozov SV, et al. Vertical field-effect transistor based on graphene–WS_2 heterostructures for flexible and transparent electronics. Nat Nanotechnol. 2013;8:100-3.
34. Zhu WJ, Tso-Ping M, Tamagawa T, Kim J, Di Y. Current transport in metal/hafnium oxide/silicon structure. IEEE Electron Device Letters. 2002;23:97-9.
35. Harari E. Conduction and trapping of electrons in highly stressed ultrathin films of thermal SiO_2. Appl Phys Lett. 1977;30:601-3.
36. Hattori Y, Taniguchi T, Watanabe K, Nagashio K. Layer-by-Layer Dielectric Breakdown of Hexagonal Boron Nitride. Acs Nano. 2015;9:916-21.
37. Callegari A, Cartier E, Gribelyuk M, Okorn-Schmidt HF, Zabel T. Physical and electrical characterization of Hafnium oxide and Hafnium silicate sputtered films. J Appl Phys. 2001;90:6466-75.
38. Yu S, Chen H-Y, Gao B, Kang J, Wong HSP. HfOx-Based Vertical Resistive Switching Random Access Memory Suitable for Bit-Cost-Effective Three-Dimensional Cross-Point Architecture. Acs Nano. 2013;7:2320-5.
39. Zhang L, Hsu Y-Y, Chen FT, Lee H-Y, Chen Y-S, Chen W-S, et al. Experimental investigation of the reliability issue of RRAM based on high resistance state conduction. Nanotechnology. 2011;22:254016.
40. Wang S-Y, Lee D-Y, Huang T-Y, Wu J-W, Tseng T-Y. Controllable oxygen vacancies to enhance resistive switching performance in a ZrO_2-based RRAM with embedded Mo layer. Nanotechnology. 2010;21:495201.
41. Lee S, Sohn J, Jiang Z, Chen H-Y, Philip Wong HS. Metal oxide-resistive memory using graphene-edge electrodes. Nat Commun. 2015;6:8407.

Chapter 6: Functional screening for potential well arrays of excitons in 2D materials

6.1 Introduction

Atomically thin TMDCs show strongly reduced screening effect of Coulomb interactions especially in their monolayer limit (1-3). Upon light absorption by a semiconductor, an exciton can form when an electron is promoted from the valence band into the conduction band and the electron-hole pair is tightly bound and confined due to the Coulomb interaction (4, 5). Excitons typically have a hydrogen-like energy spectrum, with states appearing at energies smaller than the conduction band. The difference between the bandgap and the exciton resonance energies is known as the exciton binging energy (5), which corresponds to the energy necessary to split the bound electron-hole pair and effectively render the electrons free carriers in the conduction band.

The neutral (A) exciton shows binding energies of 1 eV for monolayer TMDCs (6-9), a value which is one order of magnitude greater than the inorganic semiconductors (*5*). Such a large value of binding energy greatly exceeds the energy corresponding to room temperature which is ~ 25 meV. For this reason, the physics of excitons in TMDCs has a prominent role in the opto-electronic properties of these systems in ambient conditions. Since TMDCs can be used as LED (10-12), FET (10) and photovoltaics cells (13), it is extremely important to unveil the physics of excitons in these materials. For example, in bulk crystals the exciton binding energy is a function of the dielectric constant of the TMDCs. Upon thinning the crystal down to a few atomic layers, the excitons will be influenced by the surrounding dielectric environment (14-16). Understanding the true role played by the dielectric environment on the interaction between the bound electron-hole pair is of paramount importance for developing efficient opto-electronic devices. The exciton physics opens the possibility of incorporating TMDC in different kind of devices with a wide range of applications; Bernardi et al. (13) show that the calculated absorption coefficients of monolayer MoS_2 are higher than the bulk counterpart which is promising for future solar cells including TMDCs and Meng-Lin Tsai et al. (17) reported a efficiency of 5.23 % for the solar cell made by monolayer MoS_2 and p-Si substrate. In addition to solar cells, TMDCs photodetectors have been successful such as the few layer WS_2-graphene heterostructure with a photodetectitive range from 400 to 700 nm reported by Mehew et al. (18).

The exciton binding energy can be determined by different experimental techniques such as: two-phonon photoluminescence excitation spectroscopy (21), one-photon photoluminescence (22), optical reflectance (5, 16, 22, 23) , optical linear absorption (4, 24) and second-harmonic generation spectroscopy (25). Using these techniques, it has been reported that excited states of the excitons in monolayer TMDCs the Rydberg stated of the Hydrogen atom, and

therefore they are labelled according to the hydrogen-like energy spectrum with 1s for the ground state and 2s,3s,4s,… for the optically accessible excited excitonic states (5, 22) as shown in figure 6.1 (a). Such energy level sequence for the excitons excited states in TMDCs has been reported in many experiments. For example, E Liu et al. (2) have observed the Rydberg sequence of the A exciton (see Section 4.2.1 from Chapter 4) up to 4s in ultraclean monolayer WS_2 encapsulated by h-BN and characterized their binding energies using photoluminescence spectroscopy with and without magnetic field (2). Previously, the Rydberg series of A exciton have been observed in monolayer WS_2 without any capping material (1, 22, 26), monolayer MoS_2 encapsulated by h-BN (27) and in monolayer MoS_2 without any capping material (22).

These exciton Rydberg states show appealing properties including superior valley polarization and coherence (*28*), Zeeman effect (*29*) and non-hydrogenic series (*24, 30*) due to the non-local character of the screening of the Coulomb interactions especially for the 1s and 2s states.

6.2 Previous work

Prior experimental work on the exciton binding energies and the associated quasiparticle bandgap has primarily focussed on dielectric environments with a dielectric constant smaller to or comparable to that of the TMDCs (*31*). To date, no studies on the role of high-κ dielectric environment have been published, leaving a significant gap in the understanding of excitons in TMDCs. For example, in a representative recent experiment A. Raja et al. (*32*) present a study of the bandgap and exciton binding energy of monolayer tungsten disulphide (1L-WS_2) for three different configurations: 1L-WS_2 on Si/SiO_2, 1L-WS_2 capped with monolayer graphene (1L-graphene) and 1L-WS_2 encapsulated by 1L-graphene (*32*). In these papers, the reflectance contrast technique was used and a change as large as 300 meV was reported for encapsulated WS_2 compared to WS_2 on Si/SiO_2.

In another previous work, S. Borghardt et al. (14) reported reflectance contrast measurements of three different samples: monolayers of WSe_2 with three different dielectric environments: encapsulated in h-BN (ϵ_{av}= 6.9), h-BN (ϵ_{av}= 3.6) and CYTOP (ϵ_{av}= 1.5) as substrates. The values of the energy splitting between the ground state (1s) and the first excited state (2s) of these sample were 180 meV for WSe_2 on CYTOP, around 130 meV for encapsulated WSe_2 by h-BN and around 150 meV for WSe_2 on h-BN. Therefore, upon increasing the value of the dielectric screening constant of the surrounding medium, the exciton binding energy and the quasiparticle bandgap decreases (16).

6.3 Dielectric screening

The dielectric screening effect is the coupling of the Coulomb interactions with the dielectric properties of the surrounding material (33). Since excitons are formed by charges held together by Coulomb interaction, they can be expected to be influenced by the surrounding dielectric environment especially in atomically

thin materials where most of the electric field lines can expand in the surrounding media depending on the dielectric constant of the environment and that of the TMDC (*26*). This is pictorially represented in figure 6.1 (b) for three different dielectric configurations. The first scenario concerns the case of a monolayer TMDC in a dielectric, this would be the scenario for a suspended monolayer in vacuum. The 1s ground state and the first excited excitonic state 2s deviate from the 2D hydrogenic model due to the strong screening in the monolayer plane (*23*) as the exciton radius (the distance between the hole and electron) is small so most of the electric field lines lie within the monolayer plane. For higher excited states (e.g. 3s, 4s and so on) the exciton radii is greater so the Coulomb potential is unscreened (as most of the electric lines lie out of the monolayer plane) which leads to 2D hydrogenic model- Rydberg like series behaviour (*24*). Therefore, as the radius of the exciton increases (higher quantum number n), the dielectric screening decreases (23). The second scenario shown in figure 6.1 (b) the monolayer TMDC is capping a dielectric substrate. In this case, the Coulomb interaction between the electron and hole will feel the heterogeneous dielectric environment, and the electric field lines will permeate the dielectric medium decreasing the exciton binding energy as shown in figure 6 (c). The dielectric screening is more pronounced for the higher excited excitonic states as their radii is larger than that of the 1s state (*26, 32*). Finally, the third scenario of figure 6.1 (c) concerns a monolayer TMDCs sandwiched between two dielectrics. In this case the dielectric screening due to the dielectric environment is more pronounced than for the second scenario as top and bottom electric field lines are now able to enter the space of the dielectric. In conclusion, this intuitive analysis of the electric field line for the bound electron-hole pair reveals that the dielectric screening and the exciton binding energy should depend on the exciton radii size and the dielectric constant of the environment (*22*).

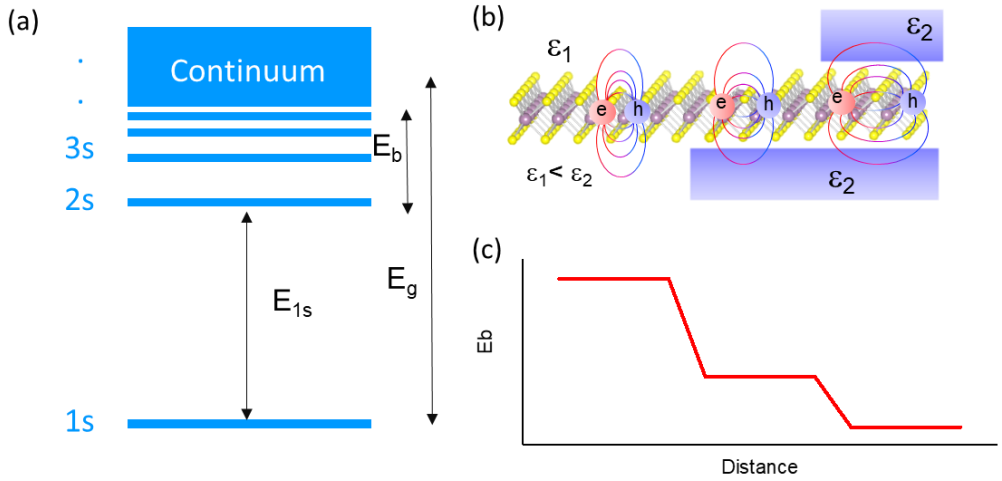

Figure 6.1: Tuning exciton binding energy through surrounding dielectric environment. (a) Schematic illustration of the exciton ground state (1s) and the excited states (2s, 3s…), the fundamental bandgap (E_g), exciton binding energy (E_b) and the lowest optical excitonic transition (E_{1s}). (b) Schematic diagram of monolayer TMDC surrounding by different dielectric environment. Starting from the left-bare TMDC in vacuum-, middle-TMDC supported on dielectric substrate- and right-encapsulated TMDC by a dielectric material. (c) Spatial dependence of the exciton binding energy of monolayer TMD from (b).

Excitons binding energies within different dielectric environments can be calculated when the 2D effective-mass Hamiltonian is (16):

$$H = - \hbar^2 \nabla_r^2/2\mu + V_{eh}(r), \quad (6.1)$$

where μ is the exciton reduced mass $\mu = (m_e^{-1} + m_h^{-1})^{-1}$ (16).

According to the original formulation by Keldysh, in the limit that the dielectric constant of the environment is smaller or equal to the dielectric constant of the TMDC, the electron-hole potential can be expressed as (16):

$$V_{eh}(r) = - \frac{e^2}{8\varepsilon_0 k r_0}[H_0(\frac{r}{r_0}) - Y_0(\frac{r}{r_0})], \quad (6.2)$$

where e is the electron charge, ε_0 is the vacuum permittivity, H_0 is the Struve function and Y_0 is the Bessel function of second kind, r_0 is the effective screening length related to the monolayer TMDCs ($r_0(k) = 2\pi\chi_{2D}\ \kappa^{-1}$ where χ_{2D} is the polarizability (16)), r is the electron-hole distance (2, 27) and κ is the average dielectric constant of the environment with $\kappa = (\varepsilon_{top} + \varepsilon_{bottom})/2$ where ε_{top} (ε_{bottom}) is the dielectric constant of the top (bottom) dielectric material (16).

This potential considers both cases: long-range distance (long electron-hole separations, $r \gg r_0$) where the screening vanishes and V(r) scales as $1/\kappa r$ and for the short-range distance ($r \ll r_0$) the monolayer TMDCs screening increases so V(r) diverges as log(r) (30). According to calculations r_0 lies between 3 to 5 nm for monolayers TMDCs (30).

The 2D hydrogen model for excitons in TMDCs widely used to describe the case of a homogeneous dielectric surrounding material with the binding energy (BE_{1s}^{A}) of the 1s ground state for the A exciton is given by (4):

$$BE_{1s}^{A} = 9/8\ (E_{1s}^{A} - E_{2s}^{A}) = 9/8\ \Delta E_{12} \quad (6.3)$$

where E_{1s}^{A} and E_{2s}^{A} are the experimental values of the exciton energies of the ground and first excited state respectively and ΔE_{12} is the peaks energy difference which scales with the ground state exciton binding energy (*5*). The quasiparticle bandgap is related to the E_{1s}^{A} and the binding energy of the exciton by the expression $E_g = E_{1s}^{A} + BE_{1s}^{A}$ (6.4) (4).

On the other hand, the 2D non-hydrogen model is used when the exciton series deviates from the hydrogen sequence, and it has a different set of expressions for the exciton binding energy and quasiparticle bandgap (*23*)

$$BE_{1s}^{A} = 2\ (E_{1s}^{A} - E_{2s}^{A}) = 2\ \Delta E_{12} \quad (6.5)$$

$$E_g = E_{1s}^{A} + BE_{1s}^{A} \quad (6.6)$$

6.4 Sample configuration and photoluminescence spectra

The aim of this project is to determine the quasiparticle bandgap and exciton binding energy for the monolayer TMDC in the case when the dielectric

environment has a dielectric constant larger than that of the TMDC. To date, this limit has not been explored mainly due to the lack of knowledge of how to attain atomically thin high-κ dielectrics. The discovery that the semiconducting HfS_2, a layered TMDC, can be photo-oxidised to attain a high quality high-κ dielectric enabled us to explore a much wider range of dielectric environments than previously studied.

Samples with a range of dielectric media where obtained from mechanically exfoliated flakes from bulk crystals of WSe_2, h-BN (provided by Manchester Nanomaterials), HfS_2 and In_2Se_3.The 2D materials (purchased from 2D semiconductors) were subsequently stacked on optically transparent quartz substrates using the PMDS transfer stamp technique described in Chapter 3. HfS_2 was first exfoliated and included in the vdW heterostructure, afterwards it was oxidised into HfO_2 with 473 nm laser irradiation wavelength with the energy density of 53 $mJ/\mu m^2$ with the equipment described in the section 4.6.1. The laser exposure time was 10 seconds, the step size was 0.5 μm and the oxidation was done in air. The thickness of monolayer WSe_2 was confirmed by photoluminescence spectroscopy exhibiting an intense spectra different to that bilayer and bulk as there is only one peak for monolayer WSe_2 (A) as it has a direct bandgap (34, 35).

The average dielectric constant is defined as $\kappa = (\varepsilon_{\text{top}} + \varepsilon_{\text{bottom}})/2$ where “top” and “bottom” refer to the two adjacent dielectric media to the monolayer TMDC. The different heterostructures studied are schematically represented in the diagrams of figure 6.2 (a)-quartz ($\kappa \sim 3.8$) and air ($\kappa \sim 1$), h-BN ($\kappa \sim 4$), photo-oxidised (10, 36) HfO_x ($\kappa \sim 15$) and ferroelectric (37) indium diselenide α- In_2Se_3 ($\kappa \sim 17$) where the average dielectric constant is in blue colour in the top left corner. Figure 6.2 (b) shows the photoluminescence spectra for the heterostructures of figure 6 (a). Hence, there are two different κ ranges: $\kappa > \kappa_{WSe2}$ and $\kappa < \kappa_{WSe2}$. For the case of bare monolayer WSe_2 (1L-WSe_2) on a quartz substrate the peak position of the A exciton is at 1.67 eV, consistently with previously reported values (*38*). The A peak is observed to shift as a function of the dielectric environment, with 30 meV redshift for $\kappa = 15$ as compared to $\kappa = 2.4$. Whilst photoluminescence sheds light on the emission of the excitons, this is also heavily dependent on the doping and strain of the TMDs. This can depend on the sample and the specific material (39, 40). Most importantly, it is known that the states of the Rydberg series are usually not distinguishable in the photoluminescence spectra, making it impossible to characterize the exciton binding energy. To this end, optical transmission spectroscopy is a well-established method in which the exciton excited states are prominent even at room temperature.

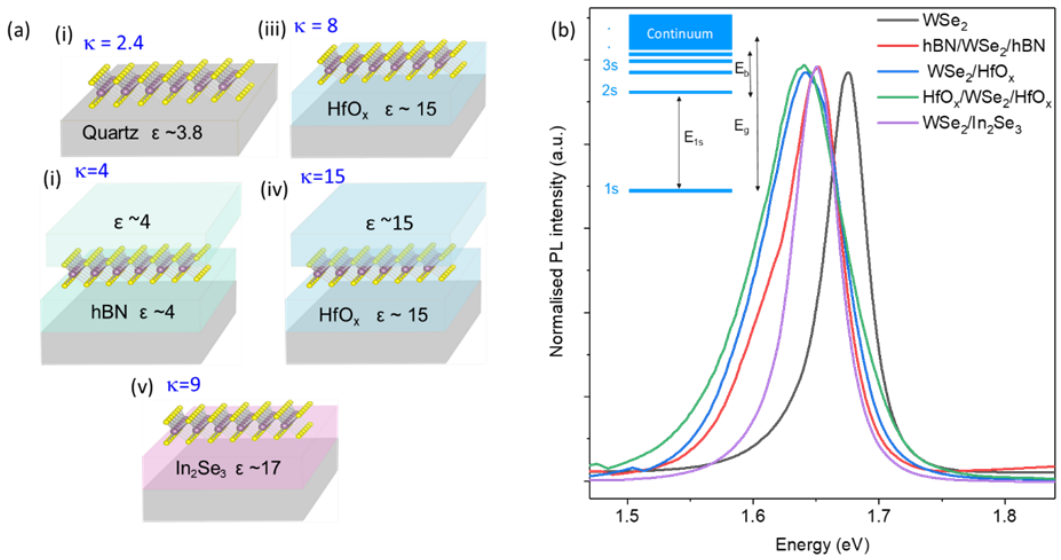

Figure 6.2: Sample structure and photoluminescence spectra. (a) Schematic of the different heterostructures combination with different dielectric environments including quartz (κ ~ 3.8) and air, h-BN (κ ~ 4), photo-oxidised HfO_x (κ ~ 15), ferroelectric In_2Se_3 (κ ~ 17), encapsulated HfO_x (κ ~ 15) and encapsulated h-BN (κ ~ 4) where the average dielectric constant (κ) is show in blue in the top left corner. (b) Photoluminescence spectra of the heterostructures of (a) at room temperature. In the top inset the schematic from the figure 6.1 (a).

6.5 Transmission spectroscopy results

Optical transmission spectroscopy is defined as follows as the ratio of the transmitted light intensity through the sample normalized to that of the substrate:

$$T=\frac{T_{sample}}{T_{substrate}} \tag{6.7}$$

Figure 6.3 shows a summary of the transmission spectroscopy measurements conducted on five different dielectric configurations. In the top row, the dashed line highlights the WSe_2 flake for each dielectric environment. The panels (a)-(e) are plots of the first derivative of the measured transmission spectra normalised to the substrate of the samples, whereas (f)-(j) are plots of the second derivative. In the first derivative, the 1s and 2s exciton states are indicated by a segment in the inflection points whereas for the second derivative, the exciton states are more clearly visualized as peaks.

Transmission measurements were performed at room temperature using a broadband light source and in air. After traveling through an objective lens, the light passed through the structures, and transmitted light was collected on the other side by a second objective lens. A pinhole was mounted to a 2D translational stage and positioned at the intermediate image plane in order to remove unwanted stray light and increase signal-to-noise ratio as shown in Chapter 4 in figure 4.12. The transmitted light was focused onto an entrance slit and the spectra were acquired with a spectrometer (IsoPlane-320) equipped with a CCD (PIXIS 400).

The energy difference between the exciton ground state (1s) and the first excited exciton state (2s) denoted by (ΔE_{12}) is calculated for all the configurations: 1L-WSe_2 on quartz substrate (figure 6.3 (a)) ΔE_{12} = 200 meV, h-BN/1L-WSe_2/h-BN (figure 6.3 (b)) ΔE_{12} = 155 meV, 1L-WSe_2/HfO_x (figure 6.3 (c)) ΔE_{12} = 110 meV, 1L-WSe_2/In_2Se_3 (figure 6.3 (d)) ΔE_{12} = 80 meV and HfO_x/1L-WSe_2/HfO_x (figure 6.3 (d)) ΔE_{12} = 49 meV.

The energy difference Δ_{12} decreases when 1L-WSe_2 has different dielectric environments with different average dielectric constant in comparison with bare 1L-WSe_2 on quartz substrate. From figure 6.3 it seems that as the dielectric constant increases, the energy difference Δ_{12} decreases which means that the exciton binging energy decreases too (see formulas 6.3 and 6.5).

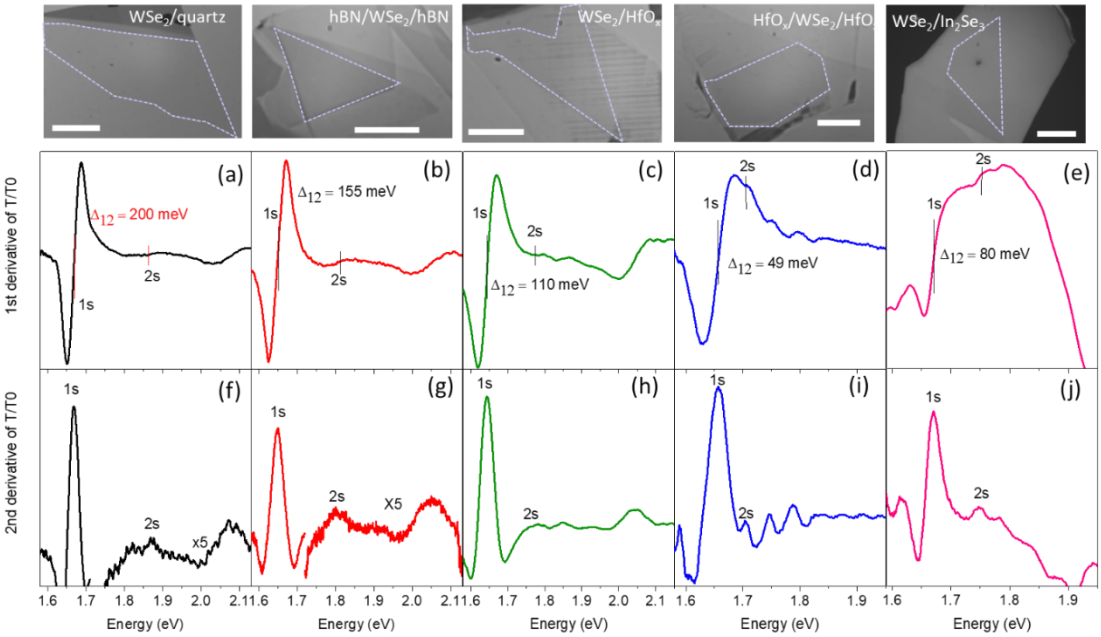

Figure 6.3: Transmission spectroscopy results. Optical micrographs of the heterostructures from left to right: 1L-WSe_2/quartz, h-BN/1L-WSe_2/h-BN, 1L-WSe_2/HfO_x, HfO_x/1L-WSe_2/ HfO_x and 1L-WSe_2/In_2Se_3 where the scale bar is 15 μm and the 1L-WSe_2 active area is indicated by the outlines. (a-e) The first derivative of the transmission spectra T of WSe_2 following the sequence of the optical pictures of the first row with the energy difference (Δ_{12}). (f-j) The second derivative of the transmission spectra T.

6.6 Modulation of excitons and the bandgap via dielectric engineering

Figure 6.4 (a) shows a plot of the 1s and 2s exciton states peak energies extracted from the second derivative of the optical transmittance plotted as a function of the average dielectric constant (κ) of the environment. Whilst both states redshift increasing the average dielectric constant, the redshift of the 1s peak is considerably smaller than the shift observed for the 2s peak. This observation is consistent with previous studies for monolayer WS_2 for $2<\kappa<15$ (41). The negligible shift of the 1s state has been observed previously for monolayers WS_2 and WSe_2 for $1.5<\kappa<3.8$ (16) which mean that the 1s state is

weakly dependent on the dielectric environment. This is due to the small radii of 1s exciton which means that less electric lines permeate the surrounding environment been undergoing less dielectric screening.

Figure 6.4 (b) shows the monotonous behaviour of Δ_{12} as a function of κ. According to both models: 2D-hydrogen model (BE_{1s}^{A} = 9/8 ΔE_{12}) and 2D non-hydrogen model (BE_{1s}^{A} = 2 ΔE_{12}) and using this expression $E_g = E_{1s}^{A} + BE_{1s}^{A}$ the quasiparticle bandgaps can be calculated using the experimental 1s exciton energy position and the extracted exciton binding.

Both models were used for estimating the exciton binding energy using the experimental data as shown in figure 6.4 (c) for the different dielectric environments. Taking the non-hydrogen model as an example, we find that the exciton binding energy reduces from 400 meV to 98 meV as κ increases from 2.4 to 15. In figure 6.4 (d), the quasiparticle bandgap (E_g) was determined from the expression $E_g = E_{1s}^{A} + BE_{1s}^{A}$ as a function of κ for different environments giving the value of 2.07 eV for bare 1L-WSe_2 on quartz. This value is reduced ~330 meV for the encapsulated 1L-WSe_2 by HfO_x which is the largest reduction reported so far for a monolayer TMDC induced by an oxide dielectric environment.

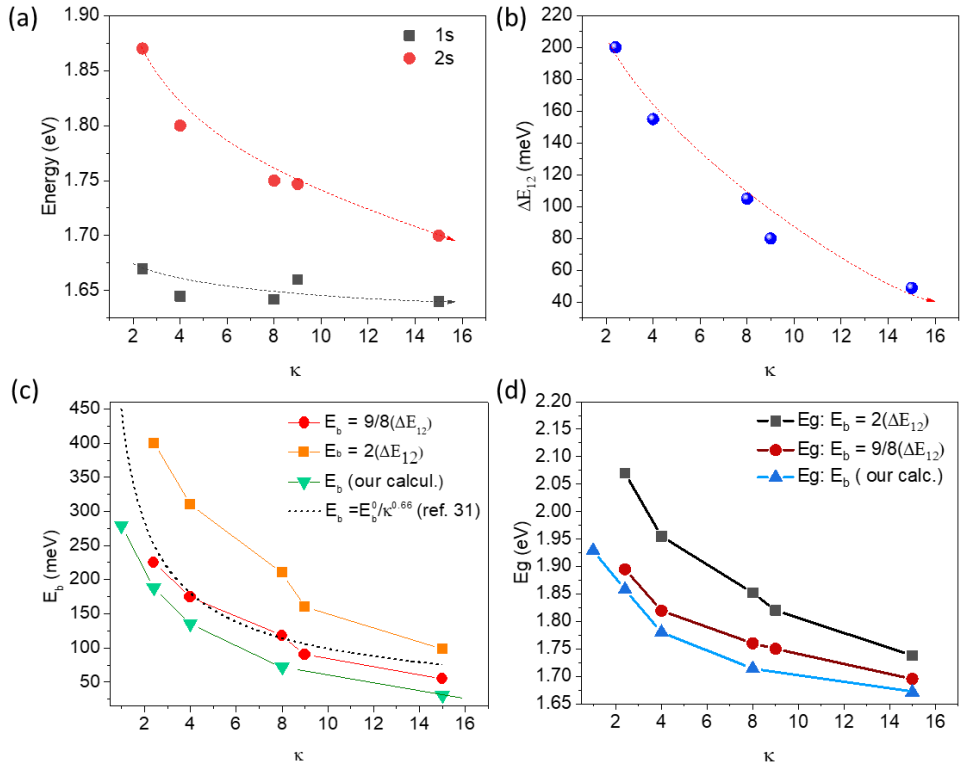

Figure 6.4: Modulation of excitons and the band gap via dielectric engineering. (a) 1s and 2s exciton states energy peaks as a function of average dielectric constants κ ranging from 2.4 up to 15 extracted from the second derivative of the transmission spectra. (b) The energy separation ΔE_{12} of monolayer WS_2 as a function of κ. (c) The κ dependence of the exciton binding energies experimentally determined from the measured ΔE_{12} using the 2D hydrogen model (E_b = 9/8 ΔE_{12}) and non-hydrogen model (E_b = 2ΔE_{12}). The exciton binding energies obtained from theoretical calculation are added for a comparison. (d) The variation of the band gap on κ, estimated from $E_g = E_{1s} + E_b$.

Figure 6.4 (c) and (d) show the calculated exciton binding energies and the quasiparticle bandgap solving theoretically the 2D Mott-Wannier model using the Keldysh potential (equation 6.2) where the dielectric environment is taken into account with the average dielectric constant κ. For these calculations, the exciton binding energy of freestanding 1L-WSe_2 is ~279 meV and reduces to 188 meV when placed on quartz substrate, and to 155 meV upon encapsulation of WSe_2 in h-BN. For 1L-WSe_2 on HfO_x on one side (encapsulated), the exciton binding energy is significantly reduced to 72 (31) meV. These calculated values show similar dependence on κ to the experimental results and they are in good quantitative agreement to the experimental values determined using the 2D hydrogen model rather than the non-hydrogen model.

Previous theoretical studies based on the screened Keldysh models have shown that the binding energy of the A exciton has a power law dependence on κ for TMDCs (30, 33, 42) which means that the exciton binding energy has a strong dependence on the average dielectric constant of the environment. $E_b = E_b^0 / \kappa\alpha$ (with α =0.7) (42) where E_b^0 is the exciton binding energy of the TMDCs in vacuum (κ =1). The experimental results are in good agreement with this model with α = 0.66 (dashed black line in figure 6.4 (c)) using the calculated exciton binding energy of 1L-WSe_2 in vacuum of ~450 meV (30, 42).

6.7 Spatial modulation of exciton binding energy of monolayer WSe_2 lateral heterostructure

The spatial change of the exciton binding energy is studied with the sample of the figure 6.5 (a). In this sample 1L-WSe_2 is placed so that some of the area is covering quartz (κ = 2.4) and the rest HfO_x (κ = 8). The scan is done across the green line acquiring the transmission spectra at each location. Figures 6.5 (b) and (c) show the second derivative of the transmission spectra for the 1s and 2s excitonic states for the green scanned line shown in figure 6.5 (a). The values for the ΔE_{12} on quartz are 193-199 meV (P1-P5) and they reduce to 105-110 meV (P6-P10) when it is scanned into the region of WSe_2 on HfO_x. The observed shift of ΔE_{12} is consistent with the previous observations shown in Figure 6.3. The spatial dependence of the exciton binding energy is presented in figure 6.5 (d) determined from $E_b = 2\Delta E_{12}$ which leads to different quasiparticle bandgap values between the two interfaces.

The spatial modulation of the binding energy leads to different values of the quasiparticle bandgap and binding energy of the exciton, making it possible to define potential wells with specific exciton potential profile by texturing the dielectric environment.

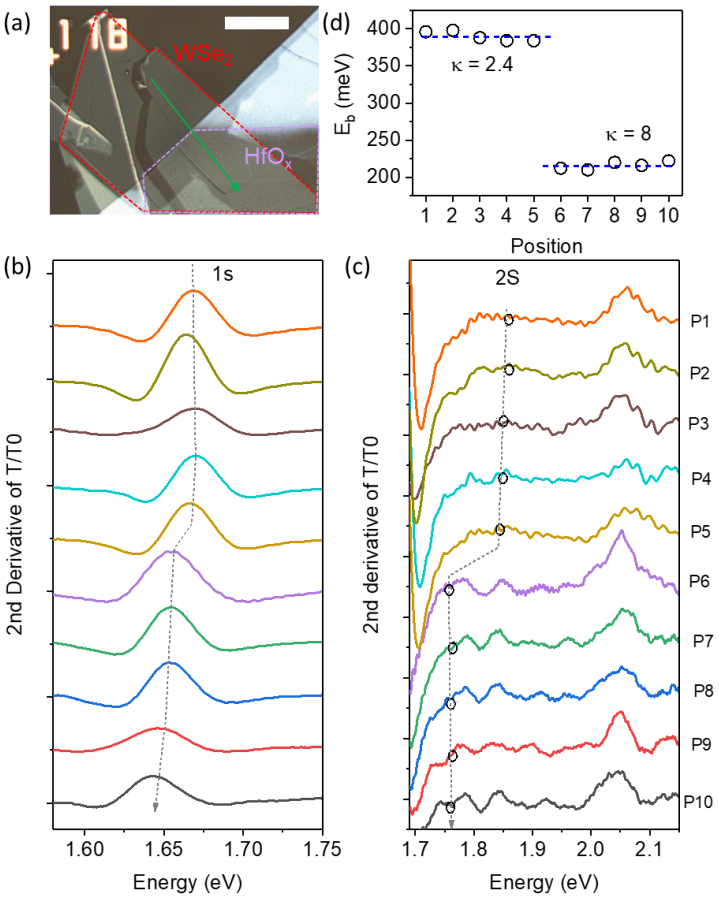

Figure 6.5: Spatial modulation of exciton binding energy of monolayer WSe_2 lateral heterostructure. (a) An optical image of monolayer WSe_2 spreading across different dielectric environments on quartz and photo-oxidised HfO_x (red: monolayer WSe_2; purple: HfO_x). Scale bar: 15 µm. The second derivative of T/T_0 of monolayer WSe_2 was taken from different locations along the green line from position 1-5 (on quartz) to position 6-10 (on HfO_x) showing the variation of the exciton ground stage 1s state (b) and the first excited excitonic state 2s (c). (d) Lateral modulation of the exciton binding energy of WSe_2 along the green dashed line determined from $E_b = 2\Delta E_{12}$.

6.8 Conclusions

The giant tuning of the exciton binging energy in monolayer WSe_2 as a function of the dielectric environment has been shown. For the first time, atomically thin high-κ dielectric HfO_x was employed attaining an average dielectric constant much larger than that of the TMDC, i.e $\kappa = 15$, leading to a suppression $330\ \mathrm{meV}$ of the exciton binging energy in ambient conditions.

The spatial modulation of the exciton binding energy across boundaries of different dielectrics was studied. This leads to a textured dielectric environment that can be used for creating the potential wells for exciton in 2D materials without hampering the structural integrity of these atomically thin semiconductors.

Bibliography

1. J. Jadczak *et al.*, Exciton binding energy and hydrogenic Rydberg series in layered ReS_2. Sci Rep.2019;9:1578.
2. E. Liu *et al.*, Magnetophotoluminescence of exciton Rydberg states in monolayer WS_2. Phys Rev.2019;99: 205420.
3. D. Van Tuan, M. Yang, H. Dery, Coulomb interaction in monolayer transition-metal dichalcogenides. Phys Rev.2018; 98: 125308.
4. A. T. Hanbicki, M. Currie, G. Kioseoglou, A. L. Friedman, B. T. Jonker, Measurement of high exciton binding energy in the monolayer transition-metal dichalcogenides WS_2 and WSe_2. Solid State Commun. 2015;203:16-20.
5. A. Raja *et al.*, Coulomb engineering of the bandgap and excitons in two-dimensional materials. Nat Commun.2017; 8:15251.
6. T. Cheiwchanchamnangij, W. R. L. Lambrecht, Quasiparticle band structure calculation of monolayer, bilayer, and bulk MoS_2. Phys Rev.2012;85:205302.
7. A. Ramasubramaniam, Large excitonic effects in monolayers of molybdenum and tungsten dichalcogenides. Phys Rev.2012;86:115409.
8. D. Y. Qiu, F. H. da Jornada, S. G. Louie, Optical Spectrum ofMos_2: Many-Body Effects and Diversity of Exciton States. Phys Rev Lett.2013;111:216805.
9. H.-P. Komsa, A. V. Krasheninnikov, Effects of confinement and environment on the electronic structure and exciton binding energy of MoS_2 from first principles. Phys Rev.2012;86:241201.
10. Peimyoo N. et al. Laser writable high-K dielectric for van der Waals nano-electronics. Science Advances. 2019; 5:1-8.
11. F. Withers *et al.*, WSe_2 Light-Emitting Tunneling Transistors with Enhanced Brightness at Room Temperature. Nano Letters.2015;15:8223-8228.
12. F. Withers *et al.*, Light-emitting diodes by band-structure engineering in van der Waals heterostructures. Nat Mater.2015;14:301-306.
13. M. Bernardi, M. Palummo, J. C. Grossman, Extraordinary Sunlight Absorption and One Nanometer Thick Photovoltaics Using Two-Dimensional Monolayer Materials. Nano Letters.2013;13:3664-3670.
14. S. Borghardt *et al.*, Engineering of optical and electronic band gaps in transition metal dichalcogenide monolayers through external dielectric screening. Physical Review Materials.2017;1:054001.
15. S. Park *et al.*, Direct determination of monolayer MoS_2 and WSe_2 exciton binding energies on insulating and metallic substrates. 2D Mater.2018;5:025003.
16. W.-T. Hsu *et al.*, Dielectric impact on exciton binding energy and quasiparticle bandgap in monolayer WS_2 and WSe_2. 2D Mater.2019; 6: 025028 (2019).
17. M.-L. Tsai *et al.*, Monolayer MoS2 Heterojunction Solar Cells. Acs Nano.2014; 8, 8317-8322.
18. J. D. Mehew *et al.*, Fast and Highly Sensitive Ionic-Polymer-Gated WS_2–Graphene Photodetectors. Adv Mater.2017;29:1700222.
19. H. Wang, C. Zhang, W. Chan, S. Tiwari, F. Rana, Ultrafast response of monolayer molybdenum disulfide photodetectors. Nat Commun.2015; 6:8831.
20. H. Jeong *et al.*, Metal–Insulator–Semiconductor Diode Consisting of Two-Dimensional Nanomaterials. Nano Letters.2016; 16:1858-1862.
21. B. Zhu, X. Chen, X. Cui, Exciton Binding Energy of Monolayer WS_2. Sci Rep.2015;5:9218.
22. H. M. Hill *et al.*, Observation of Excitonic Rydberg States in Monolayer MoS_2 and WS_2 by Photoluminescence Excitation Spectroscopy. Nano Letters.2015;15:2992-2997.
23. A. Chernikov *et al.*, Exciton Binding Energy and Nonhydrogenic Rydberg Series in Monolayer WS_2. Phys Rev Lett.2014; 113: 076802.
24. K. He *et al.*, Tightly Bound Excitons in Monolayer WSe_2. Phys Rev Lett.2014; 113: 026803

25. G. Wang *et al.*, Giant Enhancement of the Optical Second-Harmonic Emission of WSe_2 Monolayers by Laser Excitation at Exciton Resonances. Phys Rev Lett.2015;114: 097403.
26. Y. Kajino, M. Arai, K. Oto, Y. Yamada, Dielectric screening effect on exciton resonance energy in monolayer WS_2 on SiO_2/Si substrate. Journal of Physics: Conference Series.2019;1220: 012035.
27. C. Robert *et al.*, Optical spectroscopy of excited exciton states in ${\mathrm{MoS}}_{2}$ monolayers in van der Waals heterostructures. Physical Review Materials.2018;2, 011001.
28. S.-Y. Chen *et al.*, Superior Valley Polarization and Coherence of 2s Excitons in Monolayer WSe_2. Phys Rev Lett.2018; 120: 046402.
29. A. V. Stier *et al.*, Magnetooptics of Exciton Rydberg States in a Monolayer Semiconductor. Phys Rev Lett.2018; 120:057405.
30. A. V. Stier, N. P. Wilson, G. Clark, X. Xu, S. A. Crooker, Probing the Influence of Dielectric Environment on Excitons in Monolayer WSe_2: Insight from High Magnetic Fields. Nano Letters.2016; 16:7054-7060.
31. G. Gupta, S. Kallatt, K. Majumdar, Direct observation of giant binding energy modulation of exciton complexes in monolayer $MoSe_2$. Phys Rev.2017; 96, 081403.
32. A. Raja *et al.*, Coulomb engineering of the bandgap and excitons in two-dimensional materials. Nat Commun.2017; 8: 15251.
33. Y. Lin *et al.*, Dielectric Screening of Excitons and Trions in Single-Layer MoS_2. Nano Letters.2014; 14:5569-5576.
34. K. F. Mak, C. Lee, J. Hone, J. Shan, T. F. Heinz, Atomically Thin MoS_2: A New Direct-Gap Semiconductor. Phys Rev Lett.2010; 105: 136805.
35. P. Tonndorf *et al.*, Photoluminescence emission and Raman response of monolayer MoS_2, $MoSe_2$, and WSe_2. Opt Express.2013; 21:4908-4916.
36. A. De Sanctis, I. Amit, S. P. Hepplestone, M. F. Craciun, S. Russo, Strain-engineered inverse charge-funnelling in layered semiconductors. Nat Commun.2018;9,1652.
37. Y. Li, M. Gong, H. Zeng, Atomically thin α-In_2Se_3: an emergent two-dimensional room temperature ferroelectric semiconductor. Journal of Semiconductors.2019; 40:061002.
38. W. Zhao *et al.*, Evolution of Electronic Structure in Atomically Thin Sheets of WS_2 and WSe_2. Acs Nano.2013;7:791-797.
39. O. B. Aslan, M. Deng, T. F. Heinz, Strain tuning of excitons in monolayer WSe_2. Phys Rev.2018; 98:115308.
40. N. Peimyoo *et al.*, Chemically Driven Tunable Light Emission of Charged and Neutral Excitons in Monolayer WS_2. Acs Nano.2014;8:11320-11329.
41. M. R. o. A. R. Lutz Waldecker, Christina Steinke,,, R. J. K. Aaron Bostwick, Chris Jozwiak, Takashi Taniguchi, Kenji, E. R. Watanabe, Tim O. Wehling, and Tony F. Heinz, Rigid band shifts in two-dimensional semiconductors through environmental screening. . *Arxiv*, (2019).
42. I. Kylänpää, H.-P. Komsa, Binding energies of exciton complexes in transition metal dichalcogenide monolayers and effect of dielectric environment. Phys Rev.2015;92: 205418.

7 Conclusions and future work

The main objective of this thesis is to investigate high-κ dielectric materials embedded inside vdW heterostructures for optoelectronic applications, which is addressed in Chapter 5. In this chapter, the novelty of a selective laser writing process for a spatially resolved oxidation of HfS_2 into HfO_x is reported. This method is also applied to create an embedded oxide in vdW heterostructures and under metallic contacts, whilst avoiding damaging the underlying material. The resulting dielectric constant is approximately 15 for HfO_x and the dielectric breakdown is around an electric field of ~ 0.5 to 0.6 V/nm. As a result of this process, resistive switching memories were fabricated using few-layer HfO_x in a vertical structure. The graphite and gold electrodes then rely on the dielectric breakdown of HfO_x, which forms a conductive filament resulting in a hysteresis loop in the I-V measurements. The implementation of HfS_2 into the heterostructures and the subsequent photo-oxidation into HfO_x enriches the possibility of developing a wide variety of devices, allowing further investigations with other high-κ materials as well as the potential for use in a large range of novel applications.

The second objective was to investigate the dielectric screening impact on monolayer WSe_2 binding energy and quasiparticle bandgap changing the surrounding material which is explained in Chapter 6. The study of 2D exciton physics is crucial for implementing these challenging heterostructures in photonic devices especially at room temperature. In this project explained in Chapter 6, quartz (κ ~ 3.8), h-BN (κ ~ 4), photo-oxidised HfO_x (κ ~ 15) and ferroelectric indium diselenide α- In_2Se_3 (κ ~ 17) have been used as surrounding dielectric materials. This study has been done experimentally with transmission measurements which is supported by theoretical calculations. The exciton binding energy and the band gap were found to decrease with an increase of the surrounding average dielectric constant for all the devices measured. In addition, the spatial modulation of 1L-WSe_2 when surrounded by two different dielectric environments has been studied, leading to different values of the quasiparticle bandgap and binding energy of the exciton. This gives the opportunity to define potential wells with specific exciton potential profile by texturing the dielectric environment using two or more dielectric materials within the same TMDC structure. Further investigations should be done around the lateral modulation of the quasiparticle bandgap of TMDCs especially for novel devices and applications in which the specific quasiparticle profile is needed.

Appendices: Device fabrication

The devices and materials studied in this thesis were fabricated on two different type of substrates: (1) highly doped silicon wafers coated by a thermally grown oxide of 290 nm thick SiO_2 and (2) quartz. 2D materials are mechanically exfoliated on the substrate and assembled into vdW heterostructures by the procedures explained in Chapter 3. Afterwards, the positive resist PMMA KA6 (K for the number of monomers in the polymer chain) is spun onto the substrate and backed at 150 $^{\circ}$C for 2 minutes. The samples are patterned by electron beam lithography (EBL) in Nanobeam NB4 system for defining electrical contacts. Upon exposure to the electron beam, the chain of the positive tone polymer is broken into monomers. The exposed PMMA region is removed by an immersion in a developer solution of methyl isobutyl ketone (MIBK) and isopropanol (IPA) with the ratio of 1:3 respectively for about 30 seconds. IPA is used for rinsing the developer and N_2 for drying. Metallisation process is performed by a thermal evaporator with a double layer of ~ 5nm thick either Chromium or Titanium to improve the adhesion between SiO_2 and the second metal layer-50 nm thick gold. Then, the redundant metal is removed through a lift off process consisting of a sample soaking in an acetone bath for about two hours.

The whole procedure with the electron beam lithography and thermal evaporator can be explained in the following sequence steps of figure A1:

1-PMMA spin coating and baking

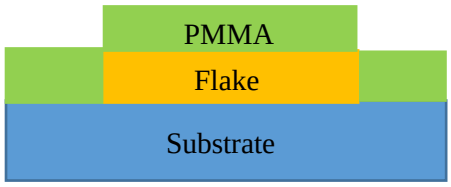

2-Electron beam lithography

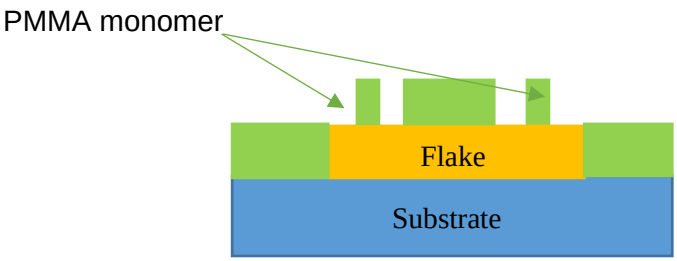

3-Develop

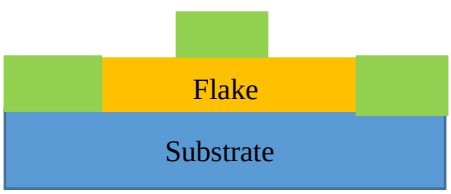

4-Thermal evaporator metallisation

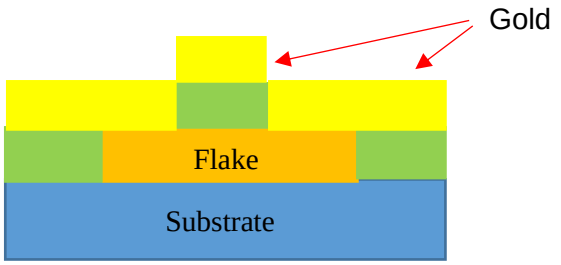

5-Lift off

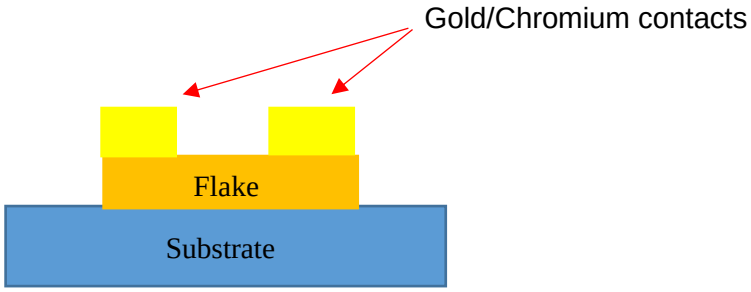

Figure A1: Schematic of electron beam lithography and metallisation in 5 steps.